



Università degli Studi di Napoli Federico II

Dottorato di Ricerca in
Fisica Fondamentale e Applicata
Ciclo XXVII
Coordinatore: Prof. Raffaele Velotta

The time synchronization system of
JEM-EUSO and JEM-EUSO
pathfinders

Settore Scientifico Disciplinare FIS/01

Dottorando

Tutor

Valentina Scotti

Dott. Giuseppe Osteria

Anni 2012-2015

Contents

Introduction	1
1 Introduction to Extreme Energy Cosmic Rays	3
1.1 The cosmic rays spectrum	4
1.2 Composition	7
1.3 EECR sources and acceleration mechanisms	11
1.4 The propagation of EECR	14
1.4.1 Interactions with cosmic backgrounds	14
1.4.2 Interactions with magnetic fields	16
1.5 Phenomenology of EECR	17
1.6 Extensive Air Showers	20
1.6.1 Electromagnetic showers	22
1.6.2 Hadronic showers	25
1.7 Nuclei and the Superposition Model	26
1.8 Detection technique	27
1.8.1 Ground arrays	28
1.8.2 Cherenkov Detector	29
1.8.3 Fluorescence detector	30
1.8.4 Hybrid Detection technique	32
1.8.5 Telescope Array	32
1.8.6 Pierre Auger Observatory	34
1.9 Overview of experimental results	36
2 The JEM-EUSO project	41
2.1 Science Objectives	44
2.1.1 Main Objective: Astrophysics through the Particle Channel	45
2.1.2 Exploratory Objectives	46
2.2 Observation Principle and Requirements	48
2.3 The JEM-EUSO system	50
2.4 The telescope	52
2.4.1 Optics System	53
2.4.2 Focal Surface	54

2.4.2.1	FS detector	56
2.4.2.2	FS electronics	57
2.4.2.3	The data acquisition and handling system . .	60
2.4.2.4	Timing and Synchronization System	61
2.4.2.5	Housekeeping System	62
2.5	Atmospheric Monitoring System	62
2.6	Calibration System	63
3	The EUSO-Balloon pathfinder	65
3.1	Objectives of the balloon flights	66
3.2	Description of the instrument	67
3.3	The working principle	70
3.3.1	Optical system	75
3.3.2	Photo Detector Module	75
3.3.3	Data Processor	79
4	The timing and synchronization system of the JEM-EUSO pathfinders	83
4.1	The GPS receivers	85
4.2	Introduction to Field Programmable Gate Arrays	89
4.3	FPGA design flow	92
4.4	The device and the design tool used	95
4.5	The CLK-Board	98
4.5.1	The clock generator	102
4.5.2	The CPU interface	104
4.5.3	The HK interface	107
4.5.3.1	Alarms	110
4.5.4	The GPS interface	111
4.5.5	The CCB interface	112
5	EUSO-Balloon Integration	115
5.1	DP Integration in Naples	115
5.2	DP-PDM Integration test at APC, Paris	120
5.3	Thermal Vacuum test at CNES, Toulouse	123
5.4	Other integration tests	125
5.5	Full integration test at IRAP, Toulouse	126
5.5.1	Trigger tests	127
5.5.2	Calibration source tests	128
5.5.3	Test triggering using GPS signal	129
5.6	Campaign simulation tests	131

6	EUSO-Balloon launch campaign	133
6.1	Ground Support Equipment and software	133
6.1.1	EUSO-Balloon instrument in AIT configuration	134
6.1.2	EUSO-Balloon instrument in flight configuration	135
6.2	The preparation of the flight	135
6.3	The condition for the flight	135
6.4	The flight	136
7	Data analysis and measurements	139
7.0.1	Jitter measurements	139
7.1	Data analysis in progress	142
7.1.1	Data Processor performance	142
7.2	Live and dead time measurement	143
	Conclusions and perspectives	147
	Bibliografia	149

Introduction

In this thesis I present the Time and Synchronization System for the JEM-EUSO pathfinder, which I designed and developed as main part of my PhD work.

JEM-EUSO is a wide-angle refractive telescope in near-UV region being proposed for attachment to the ISS. The main goal is the study of Extreme Energy Cosmic Rays. JEM-EUSO has been designed to address basic problems of fundamental physics and high-energy astrophysics investigating the nature of the Extreme Energy Cosmic Rays, EECRs ($E > 5 \times 10^{19}$ eV), which constitute the most energetic component of the cosmic radiation.

Cosmic rays are highly penetrating ionizing radiation arriving at the Earth isotropically from outer space. The phenomenon of cosmic rays has been discussed since the beginning of last century, although the study of EECR has progressed considerably over the last decade, any astrophysical accelerators able to produce such extreme events has been identified so far. These high energy particles can also shed light about the regions in which they were accelerated and the vast spaces through which they passed on their way to Earth. However, there are still a lot of unanswered question about their energy spectrum, their composition and their origin. Current data indicates that only a significant increase in the exposure at the highest energies will allow to answer all the questions concerning the particles which strike the Earth with such enormous energies.

JEM-EUSO will pioneer the investigation from Space of EECR-induced Extensive Air Showers, making accurate measurements of the primary energy, arrival direction and composition of EECRs, using a target volume far greater than is possible from the ground. The instrument consists of Fresnel lenses, a Focal Surface covered by MAPMT, Front-End readout, trigger and system electronics.

While the research and development work for JEM-EUSO is ongoing, the JEM-EUSO collaboration is completing several pathfinder experiments: EUSO-TA, EUSO-Balloon, and Mini-EUSO. In 2015 a telescope prototype will be installed in the Telescope Array site. The main aim is to perform a full scale end-to-end test of all the key technologies and instrumentation of JEM-EUSO and to prove the global detection chain. For the second mission, EUSO-BALLOON, the prototype is mounted onboard a stratospheric

balloon. EUSO-BALLOON aims to measure the atmospheric and terrestrial UV background components, in different observational modes. Mini-EUSO foresees the placement of a very small version of the JEM-EUSO detector inside the ISS to observe the atmosphere through an UV transparent window.

In my PhD work I designed and developed the component which is responsible of the timing and synchronization of the whole acquisition chain for both the TA-EUSO and the EUSO-Balloon mission.

Outline of the thesis

The first chapter gives a general introduction to cosmic ray physics and detectors. It also summarizes experimental results above the ankle of the spectrum with particular emphasis on those obtained above 10^{19} eV.

The first chapter will give a brief summary of the field of cosmic ray physics, focusing on EECR. As at very high energies cosmic rays can be studied only by measuring the secondary radiation they generate in the Earth's atmosphere, also the mechanisms which originate these particle shower and the most common techniques employed their detection are exploited. In the chapter there is also a short summary of the experimental results obtained by the two main experiments which observe EECR, the Pierre Auger Observatory (PAO) and Telescope Array (TA) project, on spectrum, mass and arrival directions of cosmic rays in the energy region in the top end of the spectrum (above $10^{19.5}$ eV).

The second chapter is devoted to an analysis of the scientific goals of JEM-EUSO and its innovations compared to the other observatory of EECR. Then a detailed description of the operating principles of the telescope and its main components will be presented, paying particular attention to the timing and synchronization system and to its links with the electronics of the focal surface. The EUSO-Balloon mission and instrument will be described in the following chapter.

The fourth chapter describes the first part of my thesis work, which consisted in the design of the Timing and Synchronization System for the JEM-EUSO pathfinders. The system will be described together with the design strategy and the implementation.

In the following chapter every phase of the integration and assembly of the EUSO-Balloon pathfinder which involved the Time and Synchronization System will be shortly reviewed. Then, in the sixth chapter I will describe the EUSO-Balloon launch campaign, which was held in Timmins (Canada) in August 2014.

The last chapter is devoted to show preliminary results of the analysis of data taken during the first EUSO-Balloon flight.

Chapter 1

Introduction to Extreme Energy Cosmic Rays

Cosmic rays are highly penetrating ionizing radiation arriving at the Earth isotropically from outer space. The phenomenon of cosmic rays has been discussed since the beginning of last century: in 1911, Victor Hess started a series of balloon flights to measure the atmospheric ionization at different altitudes and could show that, above 1 km, it increased with higher altitudes [1]. Hess hypothesised that the particles responsible for the ionization at high altitudes had an extraterrestrial origin.

More than 20 years later, Pierre Auger, using a coincidence of Geiger counters separated by up spatially distributed on the ground, demonstrated that high energy cosmic rays creates cascades of charged secondary particles in the atmosphere, called Extensive Air Showers (EAS) [2]. The discovery of EAS lead to the indirect detection of cosmic rays using ground arrays consisting of spaced detector elements which sample the shower. Studying cosmic rays, many particles (i.e. positrons [?] and muons [?] among others) were discovered before the accelerator era.

Nowadays it is known that the vast majority of cosmic ray particles are protons and atomic nuclei. Electrons and gamma rays make up less than 1% of the total flux. The energy of cosmic rays spans over 11 orders of magnitude. The traditional start of the cosmic ray spectrum is 10^9 eV, the highest energy cosmic ray ever detected was $10^{20.5}$ eV and was observed at Volcano Ranch by John Linsley in 1962 [3]. High energy cosmic rays are quite rare compared to low energy cosmic rays: the flux above 10^{19} eV is approximately 10^{10} times smaller than the flux above 10^9 eV. The Large Hadronic Collider accelerates protons to $10^{12.8}$ eV, nearly 8 orders of magnitude less than the maximum energy cosmic ray particle.

Over the past twenty years the interest in the nature and origin of the Extreme Energy Cosmic Rays (EECRs), those with energy above $10^{19.5}$ eV, has grown enormously. At these energies the cosmic ray particles, be they pro-

tons, nuclei or photons, interact strongly with the cosmic microwave background (CMB) and should be severely attenuated except for those whose sources are in our cosmological neighbourhood (<100 Mpc). Also protons of these energies may not be significantly deflected so that some of the cosmic rays may point back to their source. Although the study of EECR has progressed considerably over the last decade, any astrophysical accelerators able to produce such extreme events has been identified so far. These high energy particles can also shed light about the regions in which they were accelerated and the vast spaces through which they passed on their way to Earth. However, there are still a lot of unanswered question about their energy spectrum, their composition and their origin. Current data indicates that only a significant increase in the exposure at the highest energies will allow to answer all the questions concerning the particles which strike the Earth with such enormous energies.

This chapter will give a very brief summary of the field of cosmic ray physics, focusing on EECR. Section 1.1 briefly describes the spectrum of cosmic rays and its features, while in section 1.2 their composition is reviewed. The dominant views on acceleration and propagation mechanisms of cosmic rays are outlined in section 1.3. As at very high energies cosmic rays can be studied only by measuring the secondary radiation they generate in the Earth's atmosphere, EAS are discussed in section 1.6, while in the following section the most common techniques employed for EAS detection are exploited. Sections 1.9 summarizes the experimental results obtained by the two main experiments which observe EECR, the Pierre Auger Observatory (PAO) and Telescope Array (TA) project, on spectrum, mass and arrival directions of cosmic rays in the energy region in the top end of the spectrum (above $10^{19.5}$ eV). This is followed by a discussion of some of the experimental challenges encountered in the field, mostly related to understanding the results of the main experiments.

1.1 The cosmic rays spectrum

The all particle cosmic ray differential spectrum, that is the number of particles which reach Earth per unit of energy per square meter per steradian per second, is shown in Figure 1.1. A noteworthy feature of the cosmic ray spectrum is that it extends from several MeV up to at least 10^{20} eV and spans through several orders of magnitude in flux. The energy spectrum is well described by an inverse power law $dN/dE \sim E^{-\gamma}$, with $\gamma \sim 3$ over its wide range, but small structures appear as changes in its steepness at different energies.

Some fraction of cosmic rays with energies of up to several GeV originate from the Sun, accelerated by solar flares and coronal mass ejections. The flux of lower energy galactic cosmic rays is influenced by solar winds [?] and the

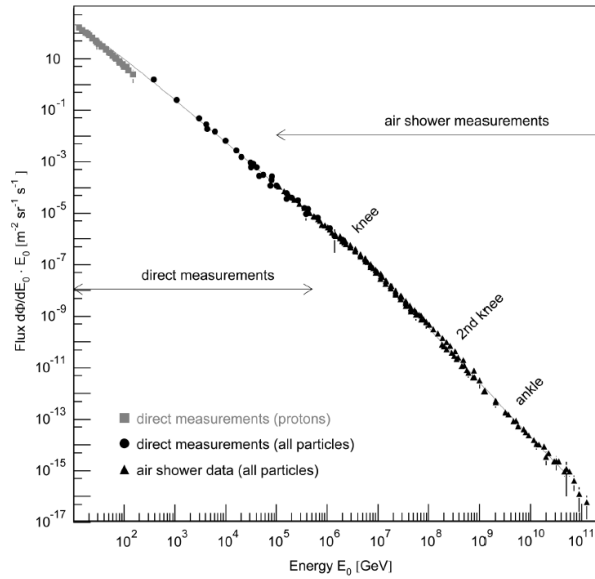


Figure 1.1: The total cosmic ray spectrum from the lowest energies up to the highest energy particles observed taken from [4]. The overall spectrum extends more than 12 decades in energy and 18 decades in flux. Above 100 GeV the total cosmic ray flux is shown, below this energy only the proton flux is plotted. Below 10^5 GeV the flux is high enough that cosmic rays can be studied by direct observation. Above this energy, cosmic rays are observed primarily by indirect observation of extensive air showers.

Earth's magnetic field deflects cosmic rays away from its surface. For these reasons, the flux measured at Earth at low energy is dependent on latitude, longitude, and azimuth angle. The magnetic field lines of the Earth sweep low energy cosmic rays towards the poles, giving rise to aurorae.

As can be seen in Figure 1.1, the flux decreases with increasing energy, by about a factor of 500 per decade in energy. This results in the flux going from more than 1000 particles per second and m at GeV energies to about one particle per m per year at a 10^{15} eV and further, to less than one particle per km per century at 10^{20} eV. Because of this rapid decrease in flux, the possibility of detecting cosmic rays also decreases with energy. At energies in the range from GeV to TeV cosmic rays can be detected directly using balloon borne detectors, or detectors in space (i.e. detectors with an area on the order of several m). Above 100 TeV, huge detector exposures are needed and usually the detectors are built on ground, typically with a large coverage area, the largest of which can reach an effective area of several thousand km. Ground observatories detect the cosmic rays indirectly, by sampling the secondary particles in the Extensive Air Shower created by the interaction of the cosmic ray with the atmosphere.

At high energy the spectrum shows several features which can give us

information about the underlying physics of cosmic rays. The plot in Figure 1.2 is a compilation of published results from several past and ongoing experiments [4], it shows the cosmic rays spectrum multiplied by a factor of E^2 . The first feature which can be seen in Figure 1.2 is the steepening of the

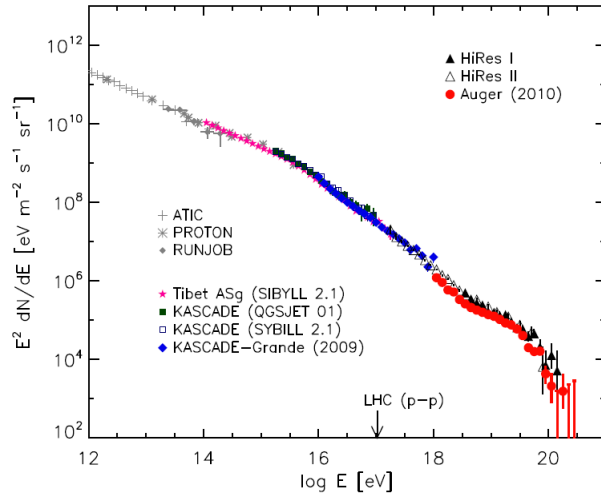


Figure 1.2: All particle cosmic ray flux above 1012 eV taken from [5]. In this plot the flux is multiplied by E^2 in order to make structures in the spectrum more visible. The measured data are from ATIC (Ahn et al. 2008), Proton (Grigorov et al. 1971), RUNJOB (Apanasenko et al. 2001), Tibet AS- γ (Chen 2008), KASCADE (Kampert et al. 2004), KASCADE-Grande (Apel et al. 2009), HiRes-I (Abbasi et al. 2009), HiRes-II (Abbasi et al. 2008b), and Auger (Abraham et al. 2010b). LHC energy reach of p-p collisions (in the frame of a proton) is indicated for comparison.

spectrum at $\sim 4 \times 10^{15}$ eV, known as the “knee”. After the knee is the still-debated so-called “second-knee”, a further steepening around 3×10^{17} eV, followed by a hardening of the spectrum known as the “ankle”, which appears around 3×10^{18} eV. These features can be related to the transitions between different sources and propagation processes of cosmic rays and will be discussed in some details in next sections. In Figure 1.2 is shown also the equivalent LHC energy (proton-proton fixed target), which is $\sim 10^{17}$ eV: this shows that particle physics above the knee is no longer directly constrained by data from accelerator experiments.

As shown in Figure 1.2, the crucial spectral feature recently established at the highest energies is a steep decline in flux above about 3×10^{19} eV, named the Greisen-Zatsepin-Kuzmin (GZK) cutoff [28] [?]. This feature is a result of the effect of interactions between extragalactic extremely high energy cosmic rays and the Cosmic microwave Background (CMB) radiation, which lead to a decrease in the average propagation length of EECR. Details on the propagation and interaction of high energy cosmic rays are discussed in section 1.3. Since the overall flux above 10^{18} eV is very low, in the past

years, the observation of the GZK suppression was one of the most challenging issues in the physics of cosmic rays, excited also by the discrepancy between the AGASA and HiRes results [?, ?]. The jump in statistics given by High Resolution Fly's Eye (HiRes), PAO and TA have made the observation of the cutoff statistically significant [4, 5, 3, 7, 6, 12]. The existence of the GZK cut-off would favour the models which attribute the origin of Extreme Energy Cosmic Rays to powerful astrophysical objects distributed on cosmological scales, such as powerful radio-galaxies or gamma-ray bursts. However, the observed feature does not differentiate between an effect to the maximum energy of acceleration at the source, E_{\max} , or the losses due to propagation through cosmological distances. A confirmation that the observed softening is the GZK feature, awaits supporting evidence from the spectral shape, anisotropies, and composition at trans-GZK energies and the observation of produced secondaries such as neutrinos and photons [5].

1.2 Composition

After the cosmic ray spectrum, the next measurement which gives us information on cosmic ray phenomena is their composition as a function of energy observed on Earth. The composition of cosmic rays can be directly measured up to energies of ~ 100 TeV with space-based experiments. For higher energies, composition is derived from the observed development and particle content of the Extensive Air Shower created by the primary cosmic ray when it interacts with the atmosphere.

The measured composition of cosmic rays up to 100 TeV compared to the abundance of nuclei in the solar system is shown in Figure 1.3. The abundance of many elements in the measured cosmic ray flux matches well with their abundance in the solar system. For some elements, however, such as lithium, beryllium, and boron, the abundance in cosmic rays is several orders of magnitude higher than in the solar system. This can be explained considering the phenomena of spallation of primary cosmic rays. Primary cosmic rays are particles accelerated by some astrophysical source, whereas secondary cosmic rays are created by the spallation of primary cosmic rays. Spallation is the emission of a small number of nucleons as the result of a heavier nucleus being hit by a high energy particle. This process is a natural result of both low energy interactions with the Galactic medium, and GZK-type energy loss mechanisms like photo-disintegration of nuclei. The lithium, beryllium, and boron over-abundance can be easily explained by the spallation of carbon and oxygen if cosmic rays transverse at least $5 \text{ g}^2 \text{ cm}^{-1}$ of matter. The same mechanism can also account for the over-abundance of elements below iron in Figure 1.3.

Further information about cosmic rays can be gleamed from the composition by looking at the ratio of unstable to stable isotopes in the cosmic

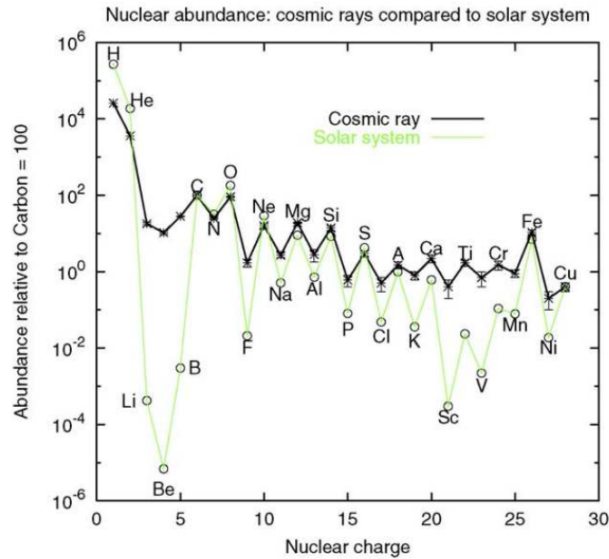


Figure 1.3: A plot of the cosmic ray composition by nuclear species, outside the heliosphere, for $E < 10^{14}$ eV cosmic rays, taken from [6].

ray flux. These measurements can constrain the escape time of cosmic rays in the Galaxy, giving a value of $\tau_{escape} \sim 2 \times 10^7$ yr. This result can be used to estimate the density of matter through which the cosmic rays propagate, and a comparison to the matter density in the Galactic disk and halo shows that Galactic cosmic rays must spend a significant fraction of this time in the halo. These estimated values of τ imply that cosmic ray nuclei must spend a significant length of time diffusing in low-density regions of the galaxy. The ratio of primary to secondary cosmic rays is also known to be energy dependent, which in turn implies that τ decreases with increasing energy, implying energy dependent diffusion of cosmic rays in the galaxy. This is expected theoretically, as the Larmor radius, as well as the diffusion coefficient, of the cosmic rays will increase with energy.

Above 100 TeV a direct measurement of the cosmic ray composition is more difficult, and in this energy range the composition is derived from the observation of characteristics of Extensive Air Showers sensitive to the mass composition, as we will see in section 1.6. Unfortunately, the interpretation of data is strictly related to the hadronic interaction models used to simulate the EAS. One interesting point regarding the composition at the highest energies can be understood by considering the previously mentioned energy loss mechanisms. The horizon structure at UHECR energies is shown in Figure 1.4 as the percentage of cosmic rays of a given nuclear species which survive propagation over a distance greater than D . This horizon is due to the energy and atomic number dependence of the interaction cross sections for processes such as the giant-dipole resonance, photo-pion production on

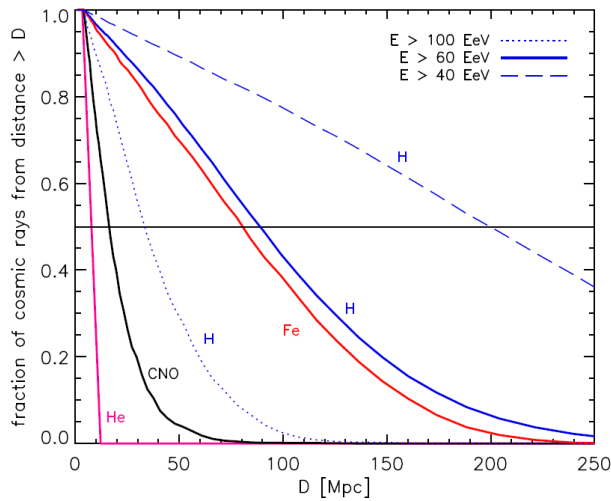


Figure 1.4: A plot of the fraction of cosmic rays which survive propagation over a distance greater than D , for protons above 40, 60, and 100 EeV, and for He, CNO, and Fe above 60 EeV. The black line shows the distance from which 50% of a given species can originate for a given atomic mass and energy. Above 6×10^{19} eV only protons and iron survive propagation over distances greater than 50 Mpc. Plot taken from [5].

CMB photons, and interactions with the Infrared (IR), Ultraviolet (UV) or optical photon background, as shown for protons in Figure 1.5. Due to these energy losses, at energies above 6×10^{19} eV only protons and nuclei with an atomic number near iron survive a propagation distance of greater than 50 Mpc. This means that the EECR flux at the highest energies is dominated by some combination of protons or nuclei near iron.

Nowadays, the most useful indicator of the composition of the primary particle is the depth in the atmosphere of the shower maximum, X_{\max} , given in g cm^{-2} . The average shower maximum, $\langle X_{\max} \rangle$, called elongation rate, scales approximately as $\ln(E/A)$, where E is the energy and A is the atomic mass of the primary cosmic ray which generated the shower (see [?]). Typically the shower maximum for protons occurs deeper in the atmosphere than that for the same energy iron nucleus, $\langle X_{\max}^p \rangle > \langle X_{\max}^{\text{Fe}} \rangle$. In addition, proton showers fluctuate more about $\langle X_{\max} \rangle$ providing another measure of composition, for example, the root mean square fluctuations about $\langle X_{\max} \rangle$.

Another useful measure of composition is the particle content of the shower such as the number of muons: proton showers have fewer muons than showers caused by heavier nuclei with the same energy. In practice, observed shower maxima and particle numbers are compared with Monte Carlo airshower simulations which involve an extrapolation to higher energies of hadronic interactions known at energies of laboratory accelerators ($\lesssim \text{TeV}$).

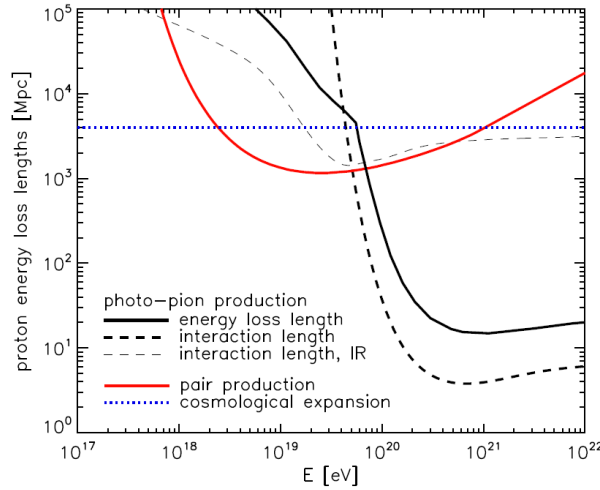


Figure 1.5: Proton energy loss lengths taken from [5]: black solid line for photo-pion production on CMB and IR-UV photons; red solid line for pair production on CMB photons. Dashed lines represent the interaction length (or mean free path to interaction) for photo-pion production on CMB photons (thick) and IR-UV photons (thin), assuming the background of [?]. The dotted blue line indicates the losses due to cosmological expansion. As can be seen, the interaction length for photo-pion production on the CMB becomes $\lesssim 100$ Mpc for protons with energies above 10^{20} eV .

Observations of cosmic rays with energies from just above the knee up to the ankle indicate a trend from a light primaries (protons) at the knee to a heavier composition up to 10^{17} eV [4]. These observations follow the general expectation that the knee is created by the end of the major Galactic cosmic ray sources and that the maximum acceleration energy is proportional to the cosmic ray charge. Near the ankle, the composition, as observed by both Auger [8] and HiRes [43], appears to reverse back towards a lighter composition. Above 10^{19} eV, however, it appears that the EECR composition again changes back towards a heavy composition, as measured by both the Auger average depth of shower maximum $\langle X_{max} \rangle$ and the root-mean-square of X_{max} [10]. This shift in the depth of shower maximum could, however, also be due to a change in particle interactions at center-of-mass energies above 100 TeV. At the same time, the measurement of $\langle X_{max} \rangle$ and X_{max} root-mean-square by HiRes and Telescope array are consistent with a proton composition at the highest energies [11]. This potential inconsistency is unclear, as the HiRes and TA results are compatible with both heavy nuclei and protons, difficult to resolve, due the use of different analysis techniques and experimental methods by the two collaborations, and a point of ongoing investigation [12].

1.3 EECR sources and acceleration mechanisms

The question about the sources of Extreme Energy Cosmic Rays has yet to be answered. The conventional bottom-up scenario assumes that all high-energy charged particles are accelerated in astrophysical environments. Any electric field can easily accelerate charged particles, but large-scale electric fields are limited in the universe due to the presence of highly conductive astrophysical plasmas. Magnetic fields, on the other hand are ever present in the universe. The dominant view in the scientific community is that up to 10^{18} eV, cosmic rays can originate inside our galaxy as products of acceleration mechanisms that take place at astrophysical sites in which there is a spatially or temporally varying magnetic field, such as supernova remnants or pulsars. In the higher energy region, cosmic rays are likely to originate outside our galaxy and the possible acceleration mechanisms are more constrained, due to the energy scale involved.

The basic ability of an accelerator to accelerate particles to a given energy is limited by the ability of the accelerating object to contain the particles inside the acceleration region. A particle of charge Z and energy E in movement through the Galactic magnetic field ($B \sim 3 \mu\text{G}$), has a curvature radius, called Larmor radius, of:

$$r_L = \frac{E}{ZeB} \sim 110 \text{ kpc} Z^{-1} (\mu\text{G}/B) (E/10^{20} \text{ eV}), \quad (1.1)$$

which is much larger than the thickness of the Galactic disk. Thus, confinement in the Galaxy is not maintained at the highest energies, motivating the search for extragalactic sources. Requiring that candidate sources be capable of confining particles up to E_{max} , translates into a simple selection criterion for candidate sources with magnetic field strength B and extension R [25]: $r_L \leq R$, i.e. $E < E_{\text{max}}$, where

$$E_{\text{max}} \simeq 10^{18} \text{ eV} Z \left(\frac{B}{\mu\text{G}} \right) \left(\frac{R}{1 \text{ kpc}} \right) \quad (1.2)$$

Figure 1.6 presents the so-called Hillas diagram where possible sources of cosmic rays are depicted as function of the size of the source and its magnetic field, taking into account the uncertainties on these parameters. Because the Larmor radius is proportional to the charge of the accelerated particle, the ability of a given accelerator to reach a certain energy depends on the nuclei being accelerated. The (lower) red line in Figure 1.6 indicates the combinations of magnetic field and size, according to Eq. 1.3, which are capable of accelerating iron nuclei up to a maximum energy of 10^{20} eV. The blue (upper) line shows the same for protons at 10^{21} eV. As can be seen, there are only a limited number of astrophysical objects which could potentially accelerate protons up to the highest energies. Most astrophysical objects do not even reach the iron confinement line up to 10^{20} eV, leaving the

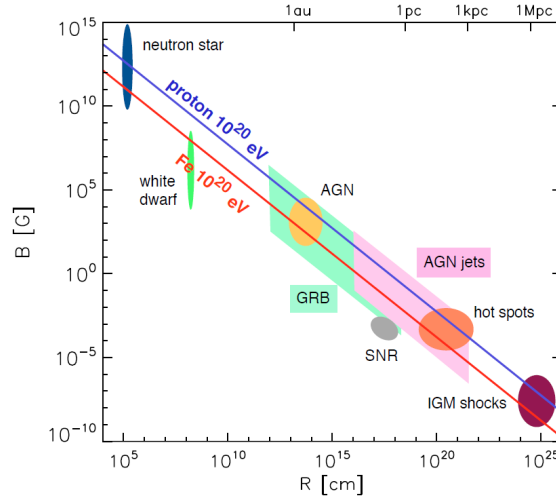


Figure 1.6: A Hillas diagram showing the possible classes of astrophysical objects versus their size and magnetic field strength taken from [5]. Above the dark blue line is the region of parameters which could confine protons above $E_{\max} = 10^{21}$ eV, while above the red line are those combinations of parameters which would allow acceleration of iron up to $E_{\max} = 10^{20}$ eV. The region occupied by each source type indicates the uncertainties in their parameters. The abbreviations in the diagram are i) AGN: Active Galactic Nuclei, ii) GRB: Gamma-Ray Burst, iii) IGM: Inter-Galactic Medium, and iv) SNR: Supernova Remnant. This plot clearly shows that the types of objects which could accelerate cosmic rays up to extreme energies is limited.

best candidates for EECR acceleration to be: neutron stars, Active Galactic Nuclei (AGN), Gamma Ray Bursts (GRBs), and accretion shocks in the intergalactic medium. The Hillas diagram also does not take into account the acceleration efficiency of the sources or corrections due to relativistic effects. Accounting for acceleration efficiency will decrease the actual reach of an accelerator, bringing down E_{\max} further, while relativistic effects could increase an accelerator's reach.

Acceleration mechanisms have to fulfil two criteria: they should enable charged particles to reach ultrahigh energies and the accelerated population should follow a power law spectrum that would fit the observed spectrum after propagation. The two best understood mechanisms which have been proposed are shock acceleration and unipolar induction. Further models can be found in literature (see [5]).

The basic principle behind shock acceleration (also known as first-order Fermi acceleration, as the second-order version is originally due to Enrico Fermi) is the transfer of energy from macroscopic motion to microscopic particles through their interaction with magnetic inhomogeneities. In second-order Fermi acceleration the acceleration is due to the random velocities of magnetic scattering centres and leads to an energy gain of $\Delta E/E \propto \beta^2$,

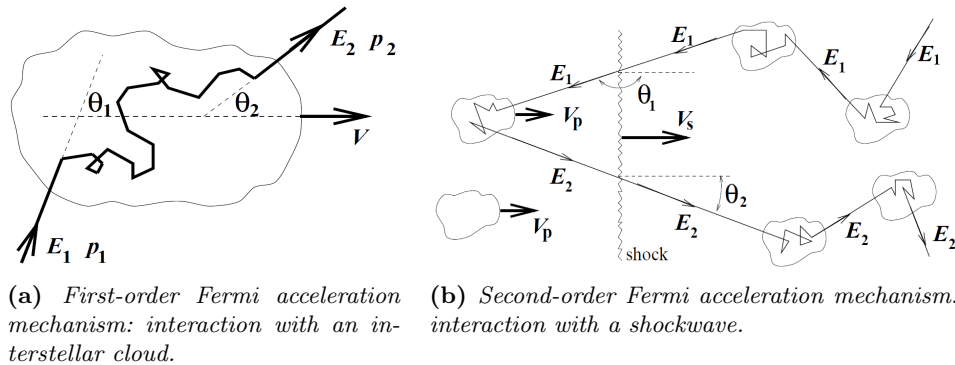


Figure 1.7: Fermi acceleration mechanisms.

where β is the average velocity of the scattering centres in units of c [13] (see Figure 1.7a). This is in contrast to first-order Fermi acceleration, in which the acceleration is due to a coherent shock wave such that the accelerated particles gain energy as they bounce back and forth and results in an energy gain of $\Delta E/E \propto \beta$ [15, 14] (see Figure 5.13b). Such shock waves are frequent in the Universe, for instance arising wherever supersonic ejecta interact with the interstellar medium. Shock regions for EECR includes SuperNova Remnants, Gamma Ray Burst shocks, Active Galactic Nuclei jets, and gravitational accretion shocks.

Supernova remnants are particularly important in the area of galactic cosmic rays. The energy density of cosmic rays in the galaxy, about 1 eV cm^{-3} , is the same order of magnitude as the magnetic field energy density and thermal gas energy density. Given the typical cosmic ray residence time in the Galaxy (*sim* 10^6 yr), this gives a cosmic ray power in the Galaxy of approximately $3 \times 10^{40} \text{ erg s}^{-1}$, which can be compared to the power emitted by supernovae in the galaxy of $3 \times 10^{41} \text{ erg s}^{-1}$, given the expected supernova rate. This implies that supernovae alone could maintain the cosmic ray population provided that about 10% of their kinetic energy is converted into cosmic rays, and supernova shock acceleration has been shown to fit the spectrum up to 10^{15} eV , that is up to the knee in the cosmic ray spectrum.

Unipolar inductors have been suggested as alternative ways to accelerate particles to ultra-high energies [?]. Unipolar induction is due to bodies such as neutron stars or other relativistic magnetic rotators, such as magnetized black holes with magnetized disks that lose rotational energy in jets [16]. These rapidly rotating magnetized bodies create relativistic winds which, combined with the magnetic field, produce an electric field $E = -v \times B/c$, where v and B are the velocity and magnetic field of the out-flowing plasma. This creates a large voltage drop, which can accelerate particles to high energy.

In addition to the acceleration mechanisms discussed above, alternative non-acceleration scenarios have been proposed. In these models, usually referred as “top-down” models, the highest energy cosmic rays are produced in decays of exotic super-heavy particles (at least 10^{23} eV). The super-heavy candidate ranges from dark matter [17] to topological defects [?, ?]. Top-down models as a class include a postulation of new particle physics and generally predict a high flux of gamma rays and neutrinos at ultra high energies. Due to these predictions, the non-observation of EECR gamma-rays by Auger and TA has put strong constraints on this type of UHECR source. Results from Auger has placed an upper limit on the photon fraction in the EECR flux, above 10^{19} eV, of less than 11.7% using hybrid events [?] and less than 2.0% using surface detector events [?] (both at 95% c.l.). The corresponding upper limit from Telescope Array is 6.2% photons above 10^{19} eV [?].

1.4 The propagation of EECR

To help discriminate between possible interpretations of recent results, in this section will be reviewed the physics of the propagation of Extreme Energy Cosmic Rays. The propagation effects which EECRs experience as they propagate away from their sources can be divided into two general categories of processes:

- interactions with cosmic backgrounds that affect their energy and their composition, but not their direction;
- interactions with cosmic magnetic fields that affect their direction and travel time, but not their energy and composition.

Both leave a variety of signatures on the observables of EECRs and generate secondary neutrinos and gamma rays. The effect of propagation on the observed spectrum, sky distribution, and composition depends on the source redshift evolution, the injected spectrum and composition, and the evolution of cosmic backgrounds and magnetic fields. The spectrum is cut-off due to photopion production of protons and photo-dissociation of nuclei of cosmic backgrounds. The composition simplifies to either proton or iron (or a mixture of the two) at trans-GZK energies. Anisotropies in the sky distribution of sources are blurred by magnetic fields for heavier primaries while protons keep most of the original anisotropies at trans-GZK energies.

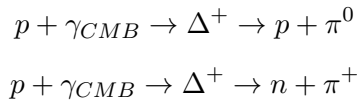
1.4.1 Interactions with cosmic backgrounds

In the intergalactic medium, cosmic rays primarily interact with the Cosmic Microwave Background (CMB) photons at the highest energies, and with

InfraRed (IR), optical, and UltraViolet (UV) background photons at slightly lower energy [5].

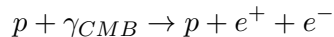
Cosmic ray protons are affected mainly by the pion production, which dominates above 7×10^{19} eV, and the pair production mechanism, which has an energy threshold with CMB photons of around 10^{18} eV.

Greisen [28], Zatsepin and Kuzmin [?] predicted that the spectrum of cosmic ray protons would have shown a cutoff at about 5×10^{19} eV due to the photopion production on the CMB. The processes that involve protons are:



Their threshold is about 10^{20} eV and the mean free path for a proton of about 10^{20} eV can be estimated as 8 Mpc. The energy loss per interaction is about 20%, thus giving an attenuation length of the order of some tenth of Mpc (GZK horizon), beyond which the proton energy falls below the GZK threshold. Therefore, the extreme high energy cosmic rays observed at ground should have been produced and accelerated within a sphere of radius limited by the GZK horizon. The same interactions can occur with IR, optical or UV backgrounds in intergalactic space, but this contribution is almost irrelevant over the entire energy range.

At lower energies, protons interact with CMB by the Bethe-Heitler pair production process:



The threshold of this reaction is 10^{17} eV. The mean free path is about 1 Gpc and the attenuation length tends to become constant and equal to the adiabatic energy loss due to the expansion of the universe, 4 Gpc. This process, however, is less relevant than the photo-pion production because the energy loss per interaction is $\sim 0.1\%$.

For primary cosmic rays nuclei with mass number $A > 1$, different interaction processes come into play. At ultra high energies, nuclei interact with the CMB and IR-UV photons mainly through the photo-disintegration of the nucleus, i.e. the ejection of one or several nucleons from the nucleus. Given that the energy of the primary nuclei is shared between nucleons, the threshold energy for these processes is typically higher than for proton and is proportional to the atomic number, in the laboratory frame of the cosmic ray. For increasing energies, different photo-erosions processes may dominate. The one with the lowest energy threshold is the Giant Dipole Resonance (GDR) which results in the emission of one or 2 nucleons and α particles. Its energy threshold is about 10 - 20 MeV in the rest frame (corresponding to few times 10^{20} eV). At energies above 3×10^{21} eV, the photopion production starts to become relevant, while the pair production and other processes are negligible on most of the energy range.

Whereas the energy threshold of the interaction processes are higher, the attenuation length of light nuclei and heavy nuclei above 10^{19} eV is smaller than for protons. As a consequence, one remarkable effect of the propagation of nuclei is that light nuclei with mass number $A < 20$ cannot travel farther than few tens of megaparsecs without disintegrating, so they should not contribute significantly to the high energy spectrum. On the other hand, the attenuation length for iron nuclei is similar to protons up to 3×10^{20} eV (see Figure 1.4), but the energy loss processes are different and, because of the ejection of nucleons, a given nucleus does not remain on the same attenuation length during its propagation. It is possible to find heavy nuclei in abundance at trans-GZK energies only if the composition were essentially dominated by iron group nuclei.

1.4.2 Interactions with magnetic fields

Magnetic deflections change the trajectory of the EECR, but not their energy. The absence of powerful astrophysical counterparts in the arrival directions of UHECRs is probably related to the effect of cosmic magnetic fields that deflect and delay particles during their propagation. The actual deflection of a given cosmic ray depends on its charge Z and on the magnetic fields through which it propagates.

Lower energy cosmic rays, those which are thought to originate from within the galaxy, must propagate an average distance of 1 Mpc. This implies that galactic cosmic rays diffuse through the galaxy and so arrive isotropically at the Earth.

At ultra-high energies, on the other hand, cosmic rays are most likely extragalactic in origin, as their Larmor radius (see eq. 1.3 exceeds the size of the galactic disk. Charged particles are subject to the influence of magnetic fields in the source environment, in the intergalactic medium, and in the Galaxy, as depicted in Figure 1.8.

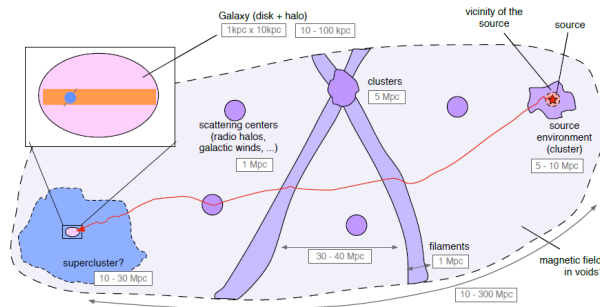


Figure 1.8: Schematic representation of magnetized regions intervening in UHECR propagation. Their approximative characteristic length scales are indicated in grey. Image taken from [5].

From equation 1.3 it can be seen that the deflection of a cosmic ray in a given magnetic field is proportional to the energy of the cosmic ray. This implies that the cosmic ray sky should become more anisotropic with increasing energy if UHECRs come from discrete sources. The expected deflection in the Galactic magnetic field for UHECR protons with energies greater than 10^{20} eV is a few degrees. The correlation between the arrival directions of UHECR and some manner of astrophysical object is then a question of statistics, which is highly limited at these energies by the low flux. At the same time, the typical deflection of a UHECR will increase with increasing charge, washing out the anisotropy. These two facts make the isolation of cosmic ray sources dependent on the composition, the source density, and the number of observed UHECR events. The number of observed EECR events is a strong motivation for experimental advancement in the field, which will be discussed later in section 1.9.

1.5 Phenomenology of EECR

Before analysing the phenomenon of Extensive Air Showers generated by cosmic rays and their observation technique, it is useful to do a brief overview of the relationship between the composition, sources, and spectra of EECR, and the open questions in the field. Different astrophysical models have been proposed which account for the different features of the spectrum and composition of the cosmic rays at the highest energies. Understanding the origin of the characteristic features of the cosmic ray flux is a key to identify their galactic and extragalactic sources and the corresponding particle acceleration and propagation mechanisms.

The knee is provided by the light elements, protons and Helium, and is explained in the framework of the Standard Model (SM) for Galactic Cosmic Rays (GCR) by the maximum energy E_{\max} of acceleration in the Galactic Sources (Supernovae Remnants). In the case of the rigidity dependent acceleration $E_{\max} \propto Z$, where Z is charge number of a nuclei, the maximum acceleration energy is reached by Iron nuclei and the Iron knee is predicted to be located at energy by factor 26 times higher than for proton knee, i.e. at energy $E_{\max}^{Fe} \sim 10^{17}$ eV. Recently, the Iron knee was found indeed at energy 8×10^{16} eV in KASCADE-Grande experiment [?] in a good agreement with rigidity acceleration prediction. The reason of the second knee are less clear, it is usually interpreted as the place where the transition from galactic to extragalactic cosmic rays starts [20], but it could be related to a change in the primary composition [19].

The explanation of the highest energy features of the spectrum are strictly related to the transition between galactic and extragalactic cosmic rays. There are three main class of models which can account for the ankle and the cutoff:

- the ankle model;
- the dip model;
- the mixed composition models.

One feature is common for all of them: the transition is described as an intersection of a steep Galactic spectrum with a flat extragalactic one [31].

In the ankle models [32] it is assumed that the transition occurs at the flat part of the observed spectrum in the energy interval $3 - 10 \times 10^{18}$ eV. The transition energy is given by the intersection of a flat extragalactic spectrum and a very steep galactic one. In the majority of ankle models the extragalactic component is assumed to be pure proton, while the galactic one should be naturally represented by Iron nuclei at energies above the Iron knee. These models predict a transition from an Iron-dominated composition to a proton-dominated one at the ankle energy and the suppression of the flux at high energies is related to the GZK effect or to the the maximum energy at which particles are injected.

In the so-called “dip-model”, on the other hand, the transition begins at the second knee and is completed at the beginning of the pair-production dip, at $E \sim 10^{18}$ eV [33]. The ankle structure in this model is due to e^+e^- pair production interaction of UHECR protons on the CMB at around 5×10^{18} eV and appears as an intrinsic part of the dip. The energy break points and shape of the UHECR spectrum is explained by GZK processes: the cut-off is then taken to be the result of photo-pion production at around 4×10^{19} eV. Since The pair-production dip and GZK cutoff are signatures of protons, the dip model predicts an almost pure proton composition above $\sim 10^{18}$ eV and a pure Iron composition below this energy, in contrast to other models. A confirmation of the shape of these features can be considered as an indirect evidence for a proton-dominated composition of primary CRs. For nuclei as primaries the shapes of the dip and cutoff are much different.

The main concept of the mixed composition model is based on the argument that any acceleration mechanism operating in gas involves different species of nuclei in acceleration process and thus the primary flux must have a mixed composition [34, 35]. In these types of models, the ankle is the signature of the transition from Galactic to extragalactic cosmic rays. In mixed composition models, the composition would be expected to be heavy up to the ankle, where it would transition to a light composition, followed by a re-transition to a heavy composition due to the charge dependence of the maximum energy of the sources [?].

Information on the energy-dependent elemental composition of cosmic rays is one of the most fundamental inputs needed to distinguish among these different classes of theories and models, which start from different assumptions. Clarifying the structure of the transition region is crucial for

reaching a coherent picture of the origin of Galactic and extragalactic cosmic rays.

The composition problem is linked to the correlation with the sources, i.e. with anisotropy in the EECR sky. If EECR are primarily protons, then they should display some anisotropy above 6×10^{19} eV as the extreme energy protons would not be deflected as much as heavy nuclei by magnetic fields. On the other hand, if the composition is indeed dominated by iron at the highest energies, then any anisotropy could be washed out by galactic magnetic fields. This could also be true if the intergalactic magnetic field is stronger than expected.

In addition to the observation of EECRs themselves, multi-messenger information can also be used to constrain EECR phenomenology. As an example, the non-observation of ultra-high energy gamma rays and neutrinos places limits on top-down models. Some number of ultra-high energy gamma rays and neutrinos are also expected as the result of pion decay from GZK interactions. Transient Large Luminosity events, such as Gamma Ray Bursts, may account for anisotropy for larger source densities. For these, source densities and transient time profiles can be used to constrain source parameters. The observation of neutrinos with energies in the range of 10^{15} to 10^{21} eV can also strongly constrain models for the origin of EECRs [?].

The resolution of the question about the origin of extreme energy cosmic rays requires a coordinated approach on three complementary fronts:

- the direct ultrahigh energy cosmic ray frontier: to understand if the observed cut-off in the EECR spectrum above 10^{19} eV is due to the particle energy loss, i.e. the GZK effect, or to the maximum energy of the EECR accelerators;
- the transition region between the knee and the ankle: to distinguish whether the composition does in fact change above 10^{19} eV, as reported by Auger, or if the observed depth of shower maximum distributions argue for a change in particle interaction at these high energies;
- the multi-messenger interface with high-energy photons and neutrinos: to understand not only at what energy does the cosmic ray flux transition from being of galactic to extra-galactic origin, but also what are the sources of EECR.

The most direct route to a resolution of this open question would be a precise measurement of the three pillars of EECR observations: spectrum, anisotropies, and composition. The following part of this chapter is devoted to explore how it is possible to measure these quantities for EECR.

1.6 Extensive Air Showers

Above 10^{15} eV, the flux of cosmic rays is so low, on the order of one particle/m²yr, that direct detection is no longer feasible, as the probability of having an event in a typical detector is too low. At such energies, the primary cosmic ray can be detected through its interaction with the Earth's atmosphere. When a cosmic ray enters the Earth's atmosphere, it interacts with a nucleus from the air (mainly nitrogen, oxygen, and argon) at a typical height of 15 to 35 km and produces a cascade of secondary particles, known as an Extensive Air Shower (EAS) [?].

Charged and neutral pions are produced in large quantities. Neutral pions ($c\tau = 25$ nm) immediately decay into two photons, charged pions ($c\tau = 7.8$ m), instead, interact again forming the hadronic shower core, that consists of long-lived secondary hadrons, i.e. baryons, charged pions, and kaons. Finally, charged pions decay into muons and neutrinos ($\pi^\pm \rightarrow \mu^\pm + \nu_\mu/\bar{\nu}_\mu$) when $E_\pi \leq 30$ GeV. Photons from π_0 decay initiate the electromagnetic cascade, in addition, γ produce hadrons or muons through photo-production or muon pair production, but these processes are infrequent. The 90% of the muon component of an air shower is produced by the decays of pions and kaons in the hadronic cascade. This component propagates through the atmosphere with small energy losses and reaches the surface of the Earth almost unattenuated. For the inclined showers, which are the showers crossing more atmosphere having large zenith angles ($\theta > 60^\circ$), the particles at ground are mostly muons and electromagnetic (EM) particles produced in the decay of muons. These EM particles form the so called "halo". Figure 1.9 shows an overview of an extensive air shower with its three components: the electromagnetic, the hadronic and the muonic component.

The properties of the primary cosmic ray, i.e. its type, mass, and energy can be inferred from the properties of the generated air shower. EAS can be characterized by several parameters:

- N_{\max} , the maximum size, in number of particles, of the shower: the size can be divided into components, such as the number of muons N_μ or electrons N_e at the shower maximum;
- X_{\max} , the depth in the atmosphere of the shower maximum;
- Λ , the elongation rate, that is the rate of increase of X_{\max} with the energy of the primary cosmic ray;
- $N_e(X)$, the mean longitudinal shower size profile, in other words the number of charged particles as a function of the shower depth;
- $dN_e = r dr d\phi$, the lateral particle distribution: i.e. the distribution of particles in the shower as a function of angle and radial distance to the shower core.

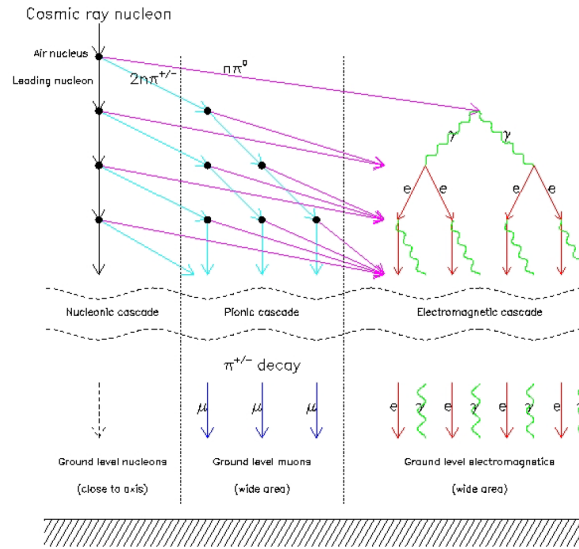


Figure 1.9: Schematic overview of an Extensive Air Shower generated by a nucleon. The shower can be divided into three components: the adronic component constituted by the primary cosmic ray, secondary nucleus and pions, the muonic component induced by charged pions and kaons, and, lastly, the electromagnetic component generated by decay of neutral pions.

Figure 2.4 shows a simulation of the distribution of the particles at ground, namely transverse to the shower axis, on the left, and along the shower axis, on the right, for each component of the shower for a proton-induced shower of 10^{19} eV. The longitudinal profile is typically studied as a function of the traversed column density (i.e., slant depth) $X = \int \rho(l)dl$, where ρ is the density of air and the integral must be taken along the shower trajectory. The shower axis indicates the axis of motion of the particle which initiated the shower. The impact point of the shower axis on the ground is called shower core. The shower reaches the ground in the form of a giant travelling nearly at the speed of light, that is called shower front.

A detailed understanding and modeling of the development of EAS are complicated by the large number of particles involved, and, in the case of a hadronic primary particle, the lack of an analytical description of QCD. Numerical simulations involve a large extrapolation of interaction cross sections and particle production mechanisms to extremely high energies where little or no data is available. However, the basic properties of EAS can be understood by using simple arguments, starting with the properties of purely electromagnetic showers.

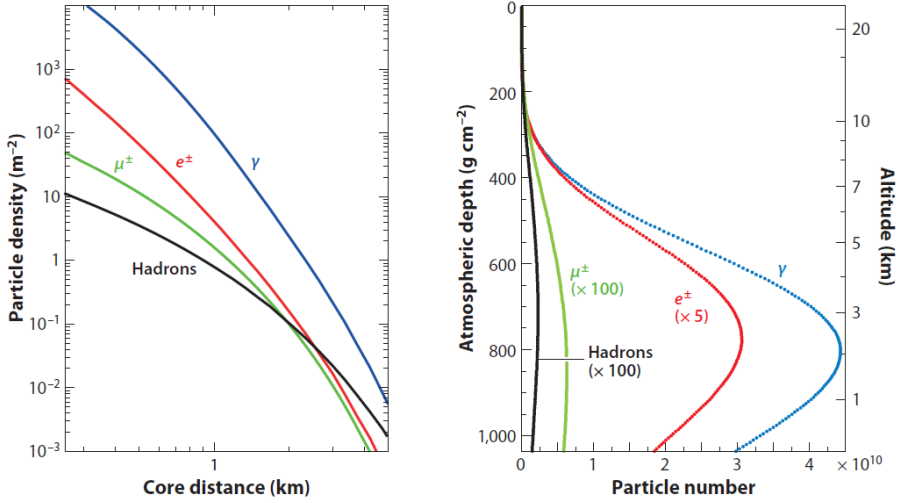


Figure 1.10: Average lateral (on the left) and longitudinal (on the right) shower profiles for vertical, proton-induced showers at 10^{19} eV. The lateral distribution of the particles at ground is calculated for 870 g cm^{-2} , the depth of the Pierre Auger Observatory. The energy thresholds of the simulation are 0.25 MeV for γ and e^\pm and 0.1 GeV for muons and hadrons. Image taken from [4].

1.6.1 Electromagnetic showers

A simple model for electromagnetic (EM) cascades which reproduces well the basic characteristics of EAS was developed by W. Heitler in 1950s [30]. In the Heitler model the evolution of an EM shower is controlled by the processes which produce additional particles: bremsstrahlung and pair production. The basic properties of EM showers follow from the scale invariance of these two dominant particle production processes.

Pair production is the creation of an electron-positron pair from an incident photon in the coulomb field of a nucleus ($\gamma\gamma \rightarrow e^+e^-$). This interaction has a threshold in energy of $2m_e c^2$. Bremsstrahlung, on the other hand, occurs when a incident charged particle is deflected in the coulomb field of a nucleus in the material through which it is passing ($\gamma e^\pm \rightarrow \gamma e^\pm$). Acceleration of a charge produces radiation, and the charged particle will lose an amount of energy proportional to $(E = mc^2)^4$ in the creation of photons. The $1/m^4$ dependence of bremsstrahlung makes it an extremely important energy loss mechanism for electrons and positrons, but less so for heavier charged particles such as muons, pions, and protons. Electrons and positrons in the EAS lose energy through bremsstrahlung and ionization, the total energy loss is:

$$\frac{dE}{dX} = -\frac{E}{\lambda_r} - \frac{dE}{dX} \Big|_{ion}$$

The first term is the radiative energy loss due to bremsstrahlung, which feeds the shower by leading to the creation of new photons. The second term is

the ionization energy loss, which is given by the Bethe-Bloch formula and transfers energy from the shower electrons and positrons to the atmosphere. As the average energy of the charged particles in the EAS decreases, the relative importance of ionization energy loss and bremsstrahlung changes. The energy at which the energy loss due to ionization and bremsstrahlung are equal is known as the critical energy E_c . The critical energy depends on the atomic number of the absorbing material, and in air is 85 MeV.

In the Heitler model, a simple picture of an EAS is created by assuming that the electrons and positrons created in the initial interaction undergo repeated 2-body splitting, in either single photon bremsstrahlung or e^+e^- pair production interactions. This is shown in part (a) of Figure 1.11. On

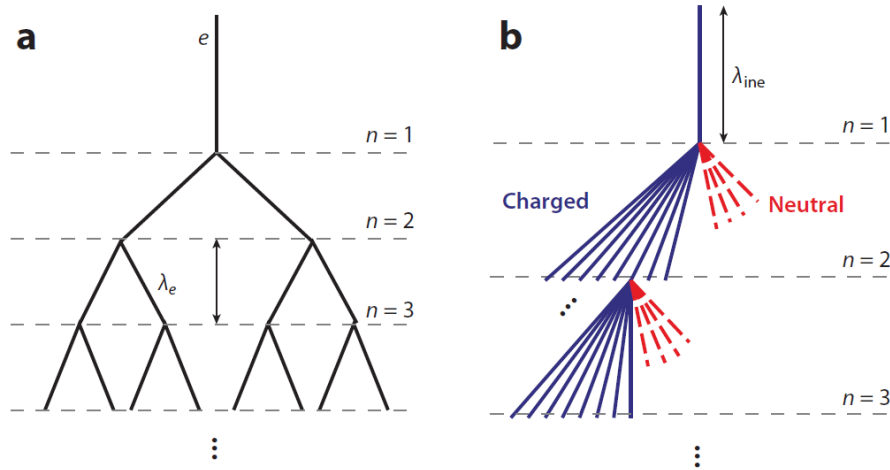


Figure 1.11: A diagram of the Heitler model (a) and a hadronic extension (b), taken from [4]. (a) An electromagnetic shower. At each interaction length each particle in the shower is assumed to split into 2 new particles, with each electron emitting a photon through Bremsstrahlung, and each photon producing a e^+e^- pair. (b) The hadronic component of a hadron-induced shower. Dashed lines represent neutral particles (π^0), and solid lines represent charged particles (π^\pm). Only one charged hadron interaction is shown for each generation. At each interaction length a number N_{ch} of charged pions and a number $1/2N_{ch}$ neutral pions are created. π^0 are assumed to decay to $\gamma\gamma$ pairs, creating EM sub-showers. π^\pm are assumed to continue to split until the average pion energy reaches E_c^π , at which point all π^\pm decay to muons and neutrinos.

average, each particle in the shower is assumed to undergo an interaction after traveling a fixed distance $d = \lambda_r \ln 2$, where λ_r is the radiation length (the radiation length in air is 37 g cm^{-2}). After travelling an average distance d an e^\pm loses one half of its energy by radiation. After n interactions there are 2^n total particles in the shower, so the number of particles at a given depth, $X = n \cdot \lambda_r$, is $N(X) = 2^n = 2^{X/\lambda_r}$. The energy E of a particle of generation n is $E(X) = E_0/2^{X/\lambda_r}$, where E_0 is the energy of the primary particle with

$n = 0$. The particle-multiplication process continues until ionization-energy losses dominate over radiative losses, i.e. when the energy reaches the critical energy E_c . The number of particles in the shower reaches the maximum at $E = E_c$, which leads to the following relations:

$$N_{max} = \frac{E_0}{E_c} \quad \text{and} \quad X_{max}^{(EM)}(E_0) \sim \lambda_r \ln \frac{E_0}{E_c}$$

The penetration depth at which the shower reaches maximum size is given by the number of interaction lengths needed for the average energy per particle to reach E_c , beyond which point no further particles are produced (by assumption). The radiation length, and thus the depth of shower maximum, are most conveniently measured as an absorber thickness in g cm^{-2} , which accounts for the density profile of the atmosphere.

The predictions of the Heitler model are confirmed by cascade theory and detailed numerical simulations. This simple model accounts well for two basic features of electromagnetic showers: the maximum number of particles in the shower is proportional to E_0 , and the depth of shower maximum, X_{max} , is proportional to the logarithm of E_0 and scales at a rate of 85 g cm^{-2} per decade of E_0 .

Multiple Coulomb scattering of electrons off air atoms leads to the lateral spread of the shower particles. The length scale of the lateral distribution of low-energy particles in a shower is characterized by the Moliere radius, $r_1 = X_0 \cdot (21 \text{ MeV}/E_c) \sim 9.3 \text{ g cm}^{-2}$. The corresponding distance in air is approximately 80 m at sea level, and it increases with altitude.

The longitudinal shower profile of an electromagnetic EAS can be calculated from cascade theory, and a related parametrization due to Gaisser and Hillas [26] is often used to fit measured shower profiles. The number of particles $N(X)$ at a given depth X is described by a Gaisser-Hillas profile:

$$N(X) = (N_{max} \frac{X - X_0}{X_{max} - X_0})^{\frac{X_{max}-X}{v}} e^{-\frac{X_{max}-X}{v}}$$

where X_0 and v are shower shape parameter. The dependence of the particle density on the distance to the shower core, i.e. the lateral distribution, is determined mainly by the multiple Coulomb scattering of electrons. Detailed calculations of the lateral shower profile by Nishimura and Kamata were parametrized by Greisen in the so-called NKG function:

$$\frac{dN_e}{r dr d\Phi} = C(s) N_e(X) \left(\frac{r}{r_1}\right)^{s-2} \left(1 + \frac{r}{r_1}\right)^{s-4.5} \quad (1.3)$$

where s is the ‘‘shower age’’, defined as $s = 3X/(X + 2X_{max})$. The shower age is defined such that $s = 0$ at the boundary of the atmosphere and $s = 1$ at shower maximum. $C(s)$ is a normalization constant depending on the shower age and Φ denotes the polar angle in the plane perpendicular to the

shower axis. The lateral density of the shower depends on the air density, due to the dependence of the lateral shower profile on the Moliere radius.

Two further effects in UHE electromagnetic showers should be mentioned before moving to hadronic EAS. The first is the so-called Landau-Pomeranchuk-Migdal (LPM) effect. The LPM effect suppresses particle production in certain kinetic regions due to the coherent addition of the interactions of photons and electrons when the interaction length is comparable to the separation between subsequent interactions. This effect becomes important above 10^{18} eV and increases shower-to-shower fluctuations while pushing X_{max} deeper into the atmosphere.

The second effect is that of geomagnetic pair production and bremsstrahlung, which is due to photons with energies above 3×10^{19} eV interacting with the magnetic field of the Earth. This causes a pre-shower in which the primary photon interacts high above the atmosphere, creating hundreds of simultaneous sub-showers. Due to the division of the primary particle energy among numerous sub-showers the LPM effect is not important and the superposition of the many lower-energy showers reduces the overall shower-to-shower fluctuations. The dependence of this geomagnetic pre-shower effect on the arrival direction allows a model-independent search of UHE photons [36].

1.6.2 Hadronic showers

Hadronic showers are characterized by very complex hadronic multiparticle productions, so it is not possible the derivation of analytic expressions for them, but with the increasing computing power, they can be calculated numerically.

A simple model to describe an hadronic shower comes from the generalization of the Heitler model has been developed by J. Matthews [?] and is depicted in Figure 1.11(b). In this model, the atmosphere is considered in layers of fixed thickness $\lambda_i n$, where $\lambda_i n$ is the interaction length of strongly interacting particles and is assumed to be constant. This is a good approximation in the energy range of 10 to 1000 GeV, where for pions in air $\lambda_i n$ 120 g/cm².

The interaction of a hadron with energy E is assumed to produce N_{tot} new particles with energy E/N_{tot} , two-thirds of which are charged particles N_{ch} (charged pions) and one-third of which are neutral particles (neutral pions). The neutral particles immediately decay into electromagnetic particles ($\pi_0 \rightarrow 2\gamma$), giving rise to the EM cascade. The charged particles interact again with air nuclei after travelling the mean hadronic interaction length $\lambda_i n$ if their energy is greater than the typical decay energy E_{dec} . Once the energy of the charged hadrons is smaller than E_{dec} , they decay producing one muon per hadron. After n generations, the energies for hadronic and

EM particles are respectively

$$E_{(had)} = \left(\frac{2}{3}\right)^n E_0 \quad \text{and} \quad E_{(EM)} = [1 - \left(\frac{2}{3}\right)^n] E_0$$

With $n \approx 6$, approximately 90% of the initial shower energy is carried by EM particles and deposited as ionization energy in the atmosphere [], since, as can be seen in Figure 2.4(b), EM particles outnumber all the other contributions. The depth of the shower maximum of a hadronic shower is expressed by:

$$N_{max}^{(had)}(E_0) \approx \lambda_{in} + X_{max}^{(EM)} \left(\frac{E_0}{2n_{tot}}\right) \sim \lambda_{in} + X_0 \ln\left(\frac{E_0}{2n_{tot}E_c}\right)$$

Therefore, a hadronic shower reaches its maximum before than an EM shower with the same energy. The number of electrons at the shower maximum of a hadronic shower corresponds to that of an EM shower with reduced energy, while the number of muons follows from that of charged hadrons:

$$N_{mu} = n_{ch}^n = \left(\frac{E_0}{E_{dec}}\right)^\alpha$$

where $\alpha = \frac{\ln(n_{ch})}{\ln(n_{tot})}$ varies in the range $0,82 \div 0,94$ and it is related to the total particle multiplicities of hadronic interactions. The number of muons is also related to the primary energy and the air density through E_{dec} .

The lateral distribution of a hadronic shower is wider than that one of an EM showers because secondary hadrons are produced at a typical, almost energy-independent transverse momentum $p_\perp \sim 350 - 400$ MeV and this leads to a large angle of low-energy hadrons relative to the shower axis. The lateral distribution of muons is wider than that of EM particles (see Figure 2.4(a)) because muons are produced mainly in the decay of low-energy pions.

1.7 Nuclei and the Superposition Model

The results derived so far assume that the shower is initiated by a proton. The interaction of a nucleus with the atmosphere can be treated in a simplified way using the superposition model. In a nucleus, the binding energy per nucleon (~ 5 MeV) is much smaller than the typical interaction energies, so a nucleus of mass A and energy E_0 can be approximately considered as A independent nucleons. Follows from this that a shower initiated by a nucleus of mass A is modelled as the sum of A independent sub-showers, each initiated by a nucleon with energy $E_h = E_0/A$. According to the superposition model:

$$\begin{aligned} N_{EM,max}^{(A)}(E_0) &= A \cdot N_{EM,max}^{(p)}(E_h) \approx N_{EM,max}^A(E_0), \\ X_{max}^{(A)} &= X_{max}^{(p)}(E_0/A), \\ N_\mu^{(A)} &= A \cdot \frac{E_0/A}{E_{dec}} = A^{1-\alpha} \cdot N_\mu^{(p)}(E_0), \end{aligned}$$

where the labels (p) and (A) denote the particle numbers and the depth of the shower maximum of proton- and nucleus-induced showers, respectively.

As can be seen, the number of charged particles is independent of the primary hadron, but X_{max} and N_{μ} are sensitive to the composition. Air showers initiated by nuclei produce a larger number of muons than proton EAS. At the same time, the lower energy of each sub-shower means that the overall shower will not penetrate as deeply into the atmosphere. An iron EAS will give approximately 40% more muons than a proton shower of the same energy (using a value of $\beta = 0.9$) and will reach its maximum 80-100 g/cm² higher in the atmosphere.

1.8 Detection technique

Cosmic rays can be studied using any typical particle detection technique. As the energy of the primary cosmic ray increases, however, several considerations come into play which allow for, or require, novel detection techniques. In what follows, the detection techniques currently used to register extensive air showers will be introduced. Detection techniques which are still in the development stages, such as radio detection, will not be discussed in detail. In figure 1.12 is shown a schematic diagram of the most commonly used detection technique for high energy cosmic rays.

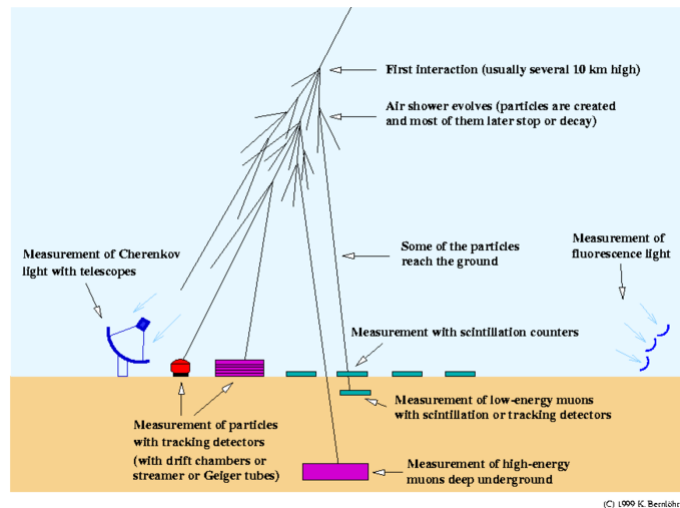


Figure 1.12: Principle of the most commonly used detector techniques for observing cosmic ultra high energy cosmic rays. Primary particles hitting the Earth's atmosphere initiate an extended air shower: EAS particles are detected by an array of particle detectors or fluorescence detector.

There have been numerous experiments which use these techniques to study high energy cosmic rays, since the pioneering measurements of EAS.

Surface detector experiments in the recent past include the Karlsruhe Shower Core and Array Detector (KASCADE) [47], its extension to higher energies KASCADE-Grande [48], and the Akeno Giant Air Shower Array (AGASA) [22].

At the moment, the main EECR observatories which are taking data are the Pierre Auger Observatory (PAO) [40], the Telescope Array (TA) [42], and the Yatkusk Air Shower Array [?]. Each of these experiments are characterized by the use of both a ground array and some form of optical detection. The Pierre Auger Observatory and the Telescope Array are particularly noteworthy, as they increased the number of observed EECR by more than an order of magnitude compared to past experiments, and these two observatories will be described in the next sections.

1.8.1 Ground arrays

The classical set-up to detect an EAS is an array of detectors at ground consisting of scintillator or water Cherenkov stations. The surface coverage needed for ground arrays is low, due to the very large number of secondary particles generated by the shower. The duty cycle of a ground array is typically close to 100%, as it is not affected by atmospheric conditions or light levels.

In scintillator and water Cherenkov ground arrays each detector samples the density of charged particles, mainly electrons and positrons at ground, in the shower and allows a mapping of the lateral distribution of the electromagnetic component of the shower. If the arrival times of particles at each sub-detector are known with a resolution on the order of a few nanoseconds, then the orientation of the shower plane can be found with an accuracy on the order of a degree, and the location of the shower core can then be determined from this information. The position of the shower plane is determined by fitting a lateral distribution function, such as the NKG function (see Eq. 1.3) to the measured particle densities. The shower size, in number of particles, is found by integration of the measured lateral distribution. The position of the shower core is generally determined with an uncertainty on the order of several meters, depending on the number of electrons in the shower [?]. The energy of the shower can be estimated in a similar manner by using the lateral distribution of muons or the correlation between the muon and electron number.

Examples of scintillator arrays in the knee region are EAS-TOP [45] and KASCADE [47]. At higher energies, there was AGASA [22] and there are still functioning KASCADE-Grande [48] and TA. The Pierre Auger Observatory is an example of water Cherenkov array.

Hadron calorimeters, such as those in KASCADE or EAS-TOP can also be employed in a surface array to measure the energy of the hadrons in the shower.

The muon component of a shower can be identified with various techniques. Frequently, particle counters are covered with absorbers of lead, iron, or soil with enough thickness to suppress the electromagnetic component or are located in underground laboratories, well shielded by rock, soil, water, or ice absorbers with a thickness corresponding to several 1000 m w.e (meter water equivalent). But muons can also be separated in tracking devices, such as the muon tracking detector of KASCADE [44]. The Pierre Auger Collaboration is studying an upgrade of its surface detector to measure the muon component of the shower.

1.8.2 Cherenkov Detector

Another possible EAS detection method is the (direct) use of Cherenkov radiation. Many particles in the shower travel with relativistic energies and approximately one third of charged particles in the shower emit Cherenkov radiation in the forward direction [49]. The threshold energy for Cherenkov radiation by electrons (at sea level) is 21 MeV, and the Cherenkov angle in the air (also at sea level) is 1.3° . Because of this low energy threshold and the large number of electrons, positrons, and photons in the shower, the majority of Cherenkov light in an EAS is due to the EM component of the shower.

The Cherenkov light can be detected with two different techniques: integrating detectors, and imaging detectors or telescopes. Both can operate only during clear moon-less nights to obtain reliable data, so their duty cycle is about 10%. The basic idea of integrating detectors is to measure the lateral distribution of the Cherenkov light with an array of photomultipliers, looking upwards in the sky, distributed over a large area at ground level. To enlarge the collection area, the PMTs are installed inside light collecting cones (Winston cones). From the Cherenkov measurements, both energy and mass of the primary particle can be derived. An example of Cherenkov arrays is Yatkusk Air Shower Array [?].

The imaging Cherenkov detectors are composed of large area collection mirrors and a camera with segmented read-out. Cosmic-ray events within the field of view of a telescope produce a focal plane image related to the direction and intensity of Cherenkov light coming from the air shower. When the direction of the shower, and so the distance of the shower axis from the telescopes are known, simple geometry can be used to reconstruct the light received from each altitude of the shower. This light is strongly correlated with the number of electrons in the shower, so it is used to estimate the shower size as a function of depth in the atmosphere and the location of the shower maximum. This procedure is essentially geometrical and has the advantage of being almost independent of numerical simulations except for the calculation of the angular distribution of Cherenkov light around the shower axis. Large Cherenkov telescopes are used to reconstruct air showers initi-

ated by primary gamma rays in TeV γ -ray astronomy. The presently largest installations are the H.E.S.S., MAGIC, and VERITAS telescopes [50, 51]. The Dual Imaging Cherenkov Experiment (DICE) [?], instead, is optimized for the reconstruction of hadron induced showers, that are background for the γ -ray telescopes.

1.8.3 Fluorescence detector

At very high energies ($E > 10^{17}$ eV), the most used technique to measure detect air showers is based on the fluorescence light. This light is emitted isotropically from the de-excitation of the nitrogen molecules of the atmosphere which had been excited by the passage of charged particles of the shower. The fluorescence light spectrum of air is shown in Figure 1.13, it can be seen that the emitted light is mostly in the UV range.

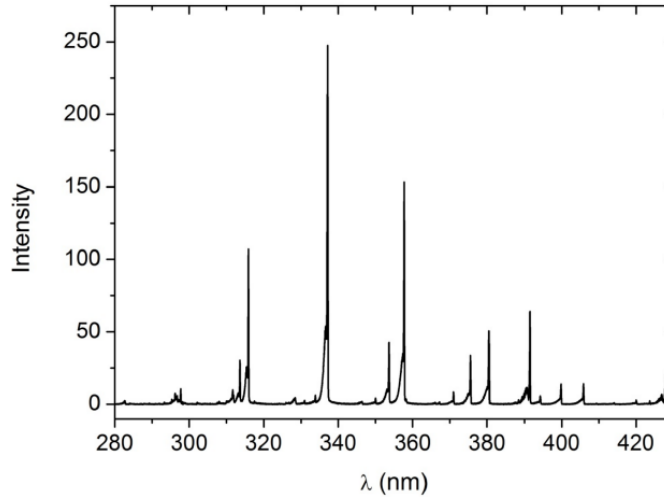


Figure 1.13: The spectrum of artificial air (80% N₂, 20% O₂) at 800 hPa measured by Dandl et al. [?]. The air mixture was excited using a 12 keV electron beam with a current of 1 to 5 μ A. The vertical scale is not absolute, but is proportional to the photon flux. The dominating 337 line of the 2P can be clearly seen.

The number of emitted fluorescence photons is proportional to the energy deposited in the atmosphere, and the constant of proportionality is known as the fluorescence yield. This yield depends on the pressure, temperature, and composition of the atmosphere and is currently known only to a low precision. The impact of uncertainties in the fluorescence yield on the reconstruction of EA is rather large, with the uncertainty on the absolute fluorescence yield being in the range of 10-15%.

Since the fluorescence yield is independent of the energy of the exciting particle, if its atmospheric dependence is taken into account, the fluorescence technique allows a calorimetric measurement of the energy deposited in the

atmosphere. About 90% of the total shower energy is converted to ionization energy and, hence, is accessible for detection. Figure 1.14 shows the average ratio between the energy deposited in the atmosphere and the primary particle energy. It depends on the primary particle type, the energy, and the

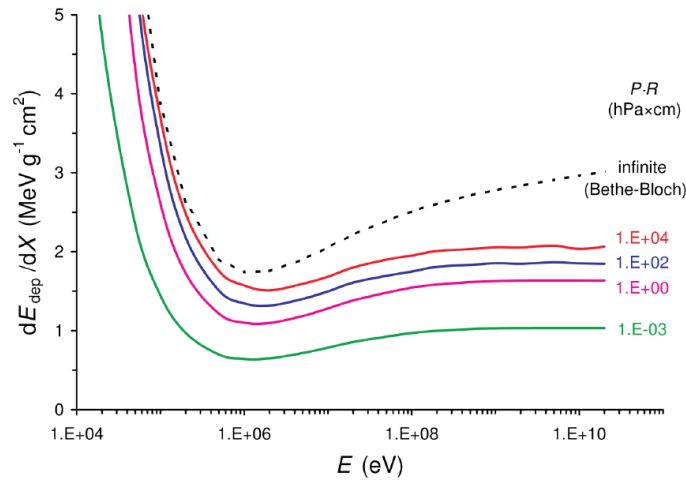


Figure 1.14: A plot showing the local energy deposit $dE_{dep} = dX$ as a function of primary particle energy in eV and the thickness parameter $P \cdot R$ in units of hPa cm. The dashed line shows the energy deposit calculated using the Bethe-Bloch formula, which does not take into account the escape of secondary particles from a thin interaction region.

hadronic model used in the simulations, but, in each case, the most of the shower energy is transferred to EM particles. In the case of a gamma-ray as a primary, about 99% of the energy is deposited in the atmosphere.

The determination of the geometry of the shower axis, the determination of the Cherenkov light fraction, and the correction for the wavelength dependent atmospheric absorption of light are also necessary to a complete reconstruction of a shower profile. The Cherenkov light signal of air showers is a highly asymmetric background for the fluorescence light. The Cherenkov light contribution to the detected signal can be estimated using parametrized models that taking into account the electron energy distributions as function of the angular distribution of the emitted Cherenkov light. Fluorescence detectors require continuous monitoring of atmospheric conditions, in particular the measurement of the wavelength dependent Mie scattering length, the detection of clouds, and the temporal variations of the density profile of the atmosphere.

Photons produced by fluorescence or by Cherenkov mechanisms are scattered by air molecules, Rayleigh Scattering, and by small particle in the atmosphere, whose size is comparable to the wavelength of the light itself, Mie Scattering. The measured light must be corrected for the attenuation related to these two phenomena.

The fluorescence detectors basically consist of mirrors that collect the light and send out it to an array of photomultipliers. The first experiments to use the fluorescence technique were Fly's Eye [41] and its successor HiRes [43]. Telescope Array and Auger experiment, that will be described in detail in next paragraphs, are using this technique combined with a surface array.

1.8.4 Hybrid Detection technique

The so-called "hybrid" detection of EAS is the observation of the same EAS by several different detector types. This technique was pioneered on large scales by the Pierre Auger Observatory and is also used by Telescope Array, both of which will be briefly presented in the next sections, both use air fluorescence telescopes and a surface array.

Since the ground array and fluorescence detector measure EAS in a different manner, they provide different information on the shower. The surface detector provides the lateral development and the location of the shower core from the EAS footprint on ground, while the fluorescence detector can give an accurate determination of the longitudinal shower development and the arrival direction of the shower within a plane from the fluorescence track. For an EAS viewed with only a single fluorescence telescope, the angular resolution is often elliptical, that is worse within the shower plane. One way to reduce this uncertainty is to view the same EAS with two FD placed some distance apart, known as stereo observation, but the angular resolution can also be improved using a hybrid approach, as the footprint of the EAS measured by the surface detector constrains the shower axis.

On the other hand, the energy determination from the surface array has a relatively high uncertainty due to the facts that only a fraction of the shower is sampled and that the energy reconstruction is dependent on shower development models. The fluorescence telescope gives an almost calorimetric determination of the EAS energy with a lower overall uncertainty than the surface array.

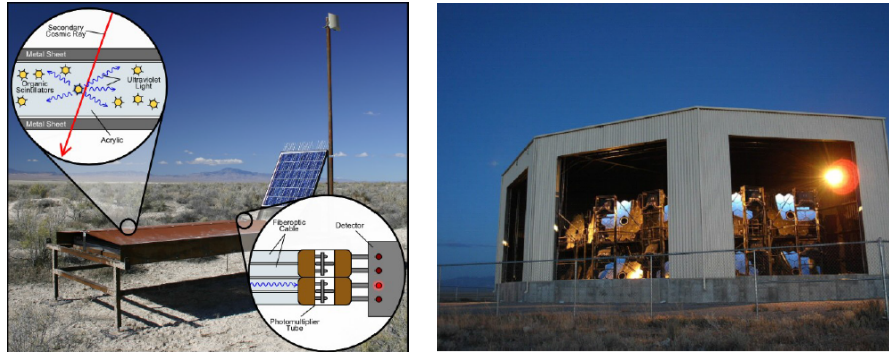
However, it has to be considered that the number of true hybrid events is limited by the small duty cycle of the fluorescence detector. It is possible to increase the number of high quality events compared to a single detector approach cross calibrating the energy reconstruction of surface array with the fluorescence energy measurement using the subset of hybrid events. Then this calibration can then be applied to the events which are viewed only by the ground array, which has a nearly 100% duty cycle.

1.8.5 Telescope Array

The Telescope Array (TA) is situated in the desert of Millard County, in Utah (USA). TA is made up of a surface array of scintillator detectors and several batteries of fluorescence telescopes, together covering a total area of

700 km².

The surface detector array is made of 507 scintillation counters deployed in a grid with a spacing of 1.2 km. A photograph of a surface detector unit is shown in Figure 1.15a. Each individual scintillating counter has two stacked layers of plastic scintillator 1.2 cm thick and 3 m² in area.



(a) A scintillator counter, 500 of which make up the TA surface array. (b) The fluorescence telescopes at Black Rock Mesa.

Figure 1.15: Picture of the Telescope Array detectors. TA is made up of a surface array of about 500 scintillator detectors and three batteries of fluorescence telescopes, together covering a total area of 700 km².

The TA has three fluorescence detectors, Black Rock Mesa, Long Ridge, and Middle Drum, located on a triangle approximately 35 km apart. There are between 12 and 14 telescopes in each station, with a field of view from 3° to 33° in elevation. One of the fluorescence station is shown in Figure 1.15b. Each telescope of the array is made of a primary mirror, consisting of 18 hexagonal mirror segments, and a read-out camera. The cameras are made of 256 UV photomultiplier tubes with attached BG3 filters.

In connection to the fluorescence detector TA operates various atmosphere monitoring equipment, which includes InfraRed (IR) cameras to monitor clouds, and a Light Detection And Ranging (LIDAR) system and a Central Laser Facility to measure the aerosol content and molecular profiles of the atmosphere.

A notable feature of TA is the calibration of the fluorescence detector using artificial air showers generated by an on-site electron linear accelerator. This Electron Light Source, shown in Figure 1.16, is placed 100 meters from the Black Rock Mesa site. The accelerator can reach 40 MeV with a bunch size of about 10⁹ electrons, and gives an energy deposit in the atmosphere equivalent to a 10¹⁶ eV cosmic ray. At 100 m from the fluorescence telescope, this gives the same detector signal as a 10²⁰ eV shower at 10 km. A comparison between the Electron Light Source air showers and true cosmic rays air showers allows a simultaneous calibration of all detector parameters

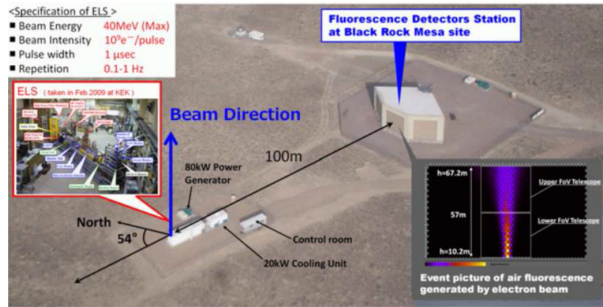


Figure 1.16: Picture of the ELS calibration system of TA, which uses an electron beam to generate test air showers.

such as fluorescence yield, mirror reflectivity, the transparencies of filters and windows, photomultiplier tube quantum efficiency, and photomultiplier tube gain. Nevertheless, the atmospheric transparency and wavelength dependence of the detector response can not be calibrated by this method, but the TA collaboration estimates that the systematic error on the energy measurement is reduced from $\sim 23\%$ to $\sim 17\%$ by the use of this end-to-end energy calibration.

TA collaboration is currently working on several extensions of their detector, known as the Telescope Array Low Energy Extension (TALE), designed to observe cosmic rays in the energy range between 3×10^{16} eV and 10^{19} eV [50]. This is accomplished by adding 10 new telescopes to the Middle Drum site, in order to extend the vertical field of view of the fluorescence detector to the range of 3° to 59° in elevation. This field of view extension is intended to allow the observation of the shower development up to the shower maximum for lower energy EAS. In addition to these upgrades, the TA surface detector will be extended by way of a graded infill of the ground array with a spacing of 400 m and 600 m.

1.8.6 Pierre Auger Observatory

The Pierre Auger Observatory (PAO) is located in western Mendoza Province (Argentina), near the Andes mountains. Auger is a hybrid observatory consisting of both a ground array and several batteries of fluorescence detectors. A schematic of Auger is shown in Figure 1.17.

The PAO ground array is composed of about 1600 water Cherenkov tanks deployed in a triangular grid with a spacing of 1.5 km. The total ground array covers an area of 3000 km^2 . A diagram of the PAO water Cherenkov detector is shown in Figure 1.20. Each cylindrical water Cherenkov detector has a footprint of 10 m^2 , stands 1.2 m high, and is made of polyethylene resin.

The PAO fluorescence detector has four sites each with six fluorescence telescopes. A photograph of the first PAO fluorescence telescope can see

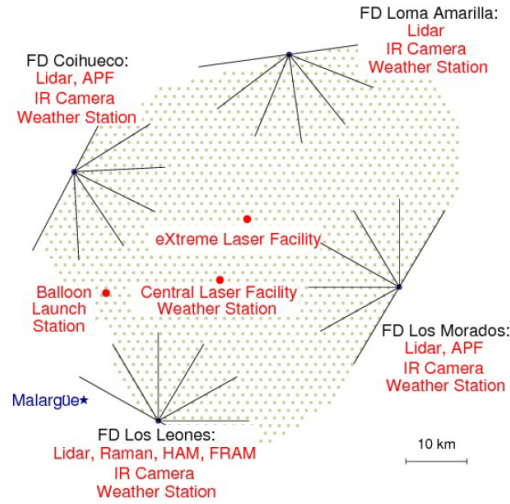


Figure 1.17: A map of the Pierre Auger Observatory showing the layout of the four fluorescence detector stations. The dots represent the individual water Cherenkov tanks of the surface detector.

in Figure ?? . In the PAO telescopes, the light is focused by a 3.5 m by 3.5 m spherical mirror into a camera made of 440 photomultiplier tubes. UV transmitting filters are installed at the entrance of the aperture of the optical system, and just inside the filter there is a ring of Schmidt corrector elements. Each telescope has a field of view of 30° in azimuthal angle and from 0° to 28.6° in elevation, and each pixel has a viewing angle of $\sim 1.5^\circ$. The fluorescence detector have uncertainty on the absolute efficiency on the order of 10%. The systematic uncertainty on EAS energy measurements is $\sim 22\%$ for the Auger fluorescence detector.

As in the case of TA, the Pierre Auger Observatory has an atmospheric monitoring system, which includes a Central Laser Facility station and an eXtreme Laser Facility. In addition, each fluorescence detector station operates a LIDAR, an IR camera for cloud detection, and a weather station. Two out of the four fluorescence stations also operate aerosol phase function monitors.

The PAO has implemented several new projects beyond its original plans. These include the Auger Muons and Infill for the Ground Array (AMIGA) [?], and the High Elevation Auger Telescopes (HEAT) [?] extensions. Both AMIGA and HEAT are similar to the TALE extensions of Telescope Array. AMIGA is an infill of the surface array with more water Cherenkov detectors at a spacing of 750 m, which extends the energy range of the ground array down to 3×10^{17} eV. HEAT, on the other hand, is a new array of tilt-able fluorescence detectors which extend the elevation range of the fluorescence detector up to 60° . The idea of HEAT is to allow the observation of lower energy showers, by enabling the fluorescence array to view the shower max-

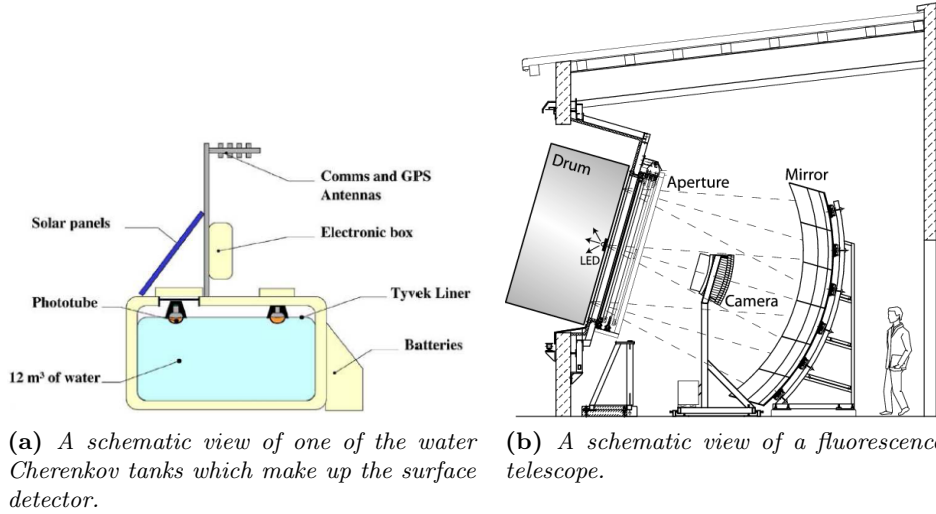


Figure 1.18: The Pierre Auger Observatory SD and FD arrays. The main elements labeled in the diagram are described in the text.

imum for showers which are close by. In addition to AMIGA and HEAT, Auger is also home to a prototype radio telescope array, the Auger Engineering Radio Array (AERA) for detecting radio emission from the shower cascades in the frequency range 30-80 MHz.

1.9 Overview of experimental results

In section 1.5 all the main open issues about EECR were reviewed, the aim of this section is to briefly resume the experimental results obtained in the last few years by high energy cosmic rays detector and their consequence on theoretical models.

The key parameter to understand the physics of EECR are spectrum, anisotropies and composition.

Concerning the spectrum, the main issues is the lack of data at extreme energy. Looking at the spectrum in Figure 1.19, all experiments show a flux suppression at the highest energies. The displayed error bars are statistical errors while the reported systematic error on the absolute energy scale is about 22%. This systematic error allows for overall energy shifts that make the two observations consistent within the estimated errors.

To ascribe the cutoff to the process of photo-pion production of protons on the CMB field (i.e. GZK suppression) one must prove that the energy scale of the cut-off and its shape correspond to the theoretical predictions and that the observed chemical composition is strongly dominated by protons. In fact, for extragalactic cosmic rays above the GZK energy threshold,

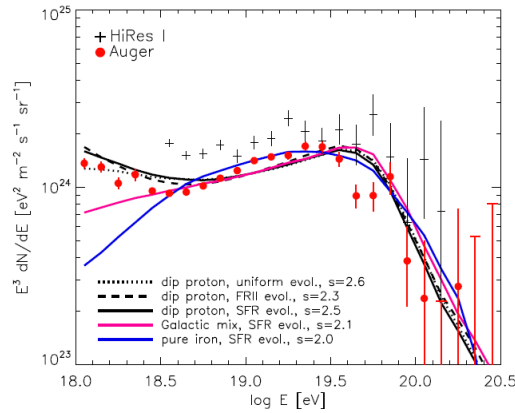


Figure 1.19: Spectrum of UHECRs multiplied by E^3 observed by HiRes I and Auger, taken from [5]. Overlaid are simulated spectra obtained for different models of the Galactic to extragalactic transition and different injected chemical compositions and spectral indices, s .

sources must be local and should follow the large scale structure of matter in the local universe. If there are protons, their arrival directions should correlate with that matter distribution on the sky. The order of magnitude increase of statistics is thus needed also above the GZK-threshold.

Figure 1.19 also shows the observed spectrum fit by different models of EECR sources. There are three models of transition from galactic to extragalactic cosmic rays: ankle, dip and mixed composition one. The ankle model is excluded or severely disfavoured by proton or Helium composition at energy $1 - 3 \times 10^{18}$ eV, i.e. below the ankle, where the particles have Galactic origin. The mass composition at these energies will be reliably measured by future low-energy detectors. However, the argument against the ankle model remains to be valid independently from mass composition at $1 - 3 \times 10^{18}$ eV, unless it is very heavy.

In some particular dip models with proton-dominated mass composition the cosmogenic neutrinos can be detectable. The flux of cosmogenic neutrinos are severely constrained by the electro-magnetic cascade upper limit and only in extreme cases it can be detectable, e.g. by JEM-EUSO. UHE neutrinos can in principle indicate directions to the sources. Even in the case when heavy nuclei dominate in the source radiation, the protons are accelerated there too, and even small produced flux can be detected from a nearby source [?].

The key issue to distinguish among different models in EECR physics is related to the measurement of chemical composition. Presently, the best method to determine the EECR composition is through the measure of the position of the maximum of the cascade developed in the atmosphere, i.e. the elongation rate $\langle X_{max} \rangle(E)$. In figure ?? are reported plot the elongation

curve as observed by PAO and HiRes [?]. Unfortunately, the determination of

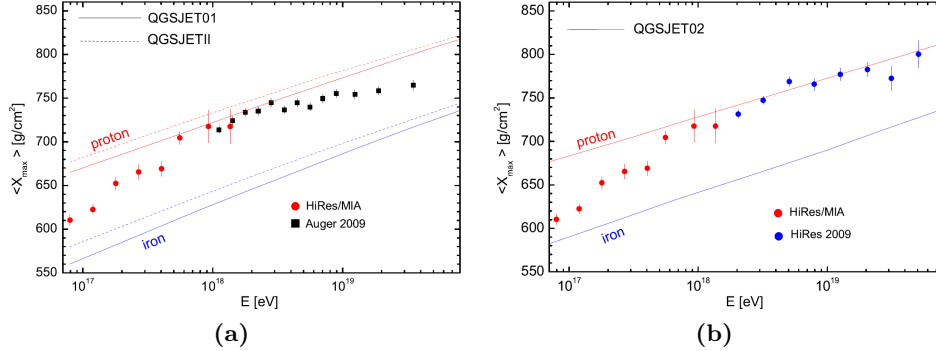


Figure 1.20: The elongation curve as observed by PAO and HiRes [?]. The calculated reference values for proton and iron are those computed in the framework of the QGSJET1-2 model.

chemical composition through $\langle X_{max} \rangle$ suffers from many systematics due to the experimental approach and uncertainties in the interaction model. Systematic errors in the $\langle X_{max} \rangle$ measurements can be as large as 20 - 25 g/cm², to be compared with the difference of about 100 g/cm² between $\langle X_{max} \rangle$ of proton and iron. A better sensitivity to distinguish different nuclei is given by the width of the X_{max} distribution, i.e. RMS(X_{max}). More experimental efforts are needed to reach a more reliable determination of the chemical composition of UHECR solving the apparent contradiction in the PAO and HiRes/TA data [?].

Though there are various hints of anisotropy in the arrival directions of extreme energy cosmic rays, no clear signal has been established with certainty so far [?]. An order of magnitude increase in exposure is needed to fully test these hints, or to find new kind of anisotropy and characterize its cause, as well as to derive significantly stronger upper limits [?]. Thus, a qualitative progress seems to require a substantially improved EECR detector that should have a number of features crucial for anisotropy searches. Since most of the analyses are limited by statistics, the exposure of any future observatory should thus be large enough to collect ten times the present world exposure in five years after construction/deployment. Anisotropy studies would take advantages from an observatory with full-sky coverage, because all possible point sources would be exposed. Finally, accurate energy assignments are essential for making precise energy cuts for trans-GZK anisotropy and also for large-scale anisotropy studies above EeV energies.

The EECR physics is one of the most interesting fields at the intersection of astrophysics and particle physics. Despite a serious progress in the experiment, presently it is not possible to say a lot about the origin of particles with energies above 10¹⁹ eV, and only a few models of particle acceleration

in astrophysical sources may simultaneously satisfy both the constraints on physical conditions in these accelerators and the strict lower bound on the number density of sources obtained recently from the absence of clustering of arrival directions.

Chapter 2

The JEM-EUSO project

JEM-EUSO (Extreme Universe Space Observatory on-board the Japanese Experiment Module) [62] on the International Space Station (ISS) [?] is a new type of observatory which aims to observe fluorescence and Cherenkov photons generated by air showers created by Extreme Energy Cosmic Rays, EECRs ($E > 5 \times 10^{19}$ eV), in the Earth's atmosphere. Looking down the Earth from space, it will utilize the atmosphere as a detector of cosmic ray air showers with the aim of significantly increasing the exposure to EECRs compared to the largest ground-based air shower arrays presently in operation [?].

The main objective of JEM-EUSO is to investigate the nature and origin of EECRs: to identify their sources by arrival direction analysis and to measure their energy spectra with a high collecting power, beyond any other previous or planned experiment so far. The scientific objectives include charged particle astronomy and astrophysics, as well as other exploratory objectives such as the detection of extreme energy gamma rays and neutrinos [55].

The JEM-EUSO telescope is designed to monitor the Earth's atmosphere from space, looking towards nadir during night-time, to detect the Ultra Violet (UV, $\lambda = 290\text{-}430$ nm) tracks generated by the Extensive Air Showers (EAS), initiated by a primary cosmic ray particle. By imaging, with a time resolution of the order of microseconds, the fluorescence and Cherenkov photons of the EAS, JEM-EUSO will reconstruct energy, arrival direction and nature of the primary EECR particle. This is an established technique that has been employed by several ground-based UHECR observatories [23], but never in space-based observations.

The instrument is planned to be attached to JEM/EF (Exposed Facility) of ISS for a three years long mission. Placed at an altitude of about 400 km from the Earth's surface, JEM-EUSO will orbit the Earth, with a speed of ~ 7 km/s, every ~ 90 minutes and will be able to reach an instantaneous aperture of about $6\text{-}7 \times 10^5$ km² sr, beyond the practical limit of any ground-

based EECRs observatory.

The JEM-EUSO telescope will have a super-wide ($\pm 30^\circ$) Field-of-View (FoV) with optics composed by Fresnel lenses; it will record the track of an EAS with a time resolution of 2.5 μ s and a spatial resolution of about 0.75 km (corresponding to 0.1°) in nadir mode. These time-segmented images allow determining energy and direction of the primary particles. The focal surface of the JEM-EUSO telescope will be formed by about 6000 Multi-Anode PhotoMultipliers Tubes (MAPMTs) with a total number of pixels of the order of three hundred thousand.

Firstly proposed as a free-flyer, the EUSO observatory was selected by the European Space Agency (ESA) as a mission attached to the Columbus module of the ISS. The phase-A study for the feasibility of that observatory (hereafter named ESA-EUSO) was successfully completed in July 2004. Nevertheless, because of financial problems in ESA and European countries, the green-light to start the ESA-EUSO phase-B was postponed for a long time. In 2006, Japanese and USA teams redefined the mission as an observatory attached to the Japanese Experiment Module/Exposure Facility (JEM/EF) of the ISS. They renamed it as JEM-EUSO and started with a renewed two-year-long Phase A study, whose results were firstly reported in December 2008. The Phase A study has then been continued with extensive simulations, design, and prototype hardware developments that have significantly improved the JEM-EUSO mission profile, targeting the launch in the framework of the second phase of JEM/EF utilization. At the moment, the mission consortium includes 17 countries and is lead by RIKEN (Japan), in coordination with the Japanese Space Agency (JAXA).

With respect to the first design, JEM-EUSO reduces the threshold energy down to $\sim 10^{19}$ eV and increases the effective area by means of advances in technology and taking advantage of specific features of the JEM/EF module. The reduction in the threshold energy is realized thanks to new lens material, improved optical design, detectors with higher quantum efficiency and improved algorithm for event trigger. The increase in effective area is realized by inclining the telescope from nadir (Fig. 2.1); under this so-called “tilted mode”, the threshold energy gets higher since the mean distance to EAS and atmospheric absorption both increase.

The JEM-EUSO telescope, as it is designed, can reconstruct the incoming direction of the EECRs with accuracy better than few degrees and its observational aperture of the ground area is a circle with 250 km radius. The instantaneous aperture of JEM-EUSO is larger than the Pierre Auger Observatory by a factor ranging from 65 in nadir mode to 280 in tilted mode. A comparison between the exposure of JEM-EUSO and current or past cosmic ray observatories is shown in Fig. 2.2.

While the research and development work for JEM-EUSO is ongoing, the JEM-EUSO collaboration is completing several pathfinder experiments: EUSO-TA, EUSO-Balloon, and Mini-EUSO.

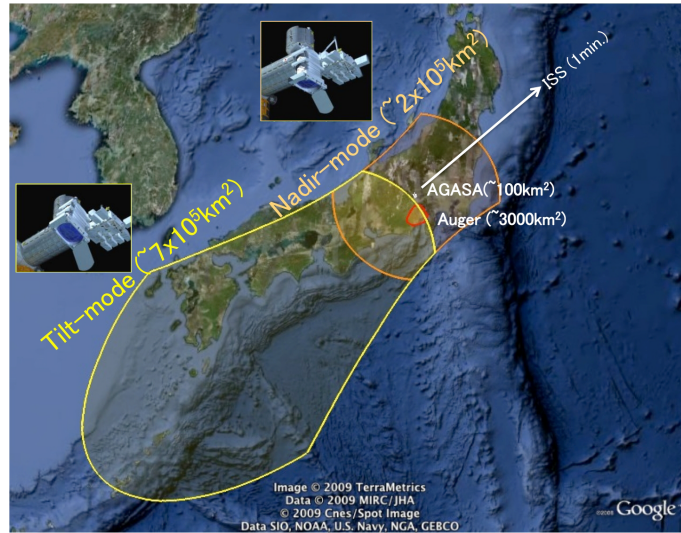


Figure 2.1: Area monitored from the JEM-EUSO telescope in tilted and nadir mode.

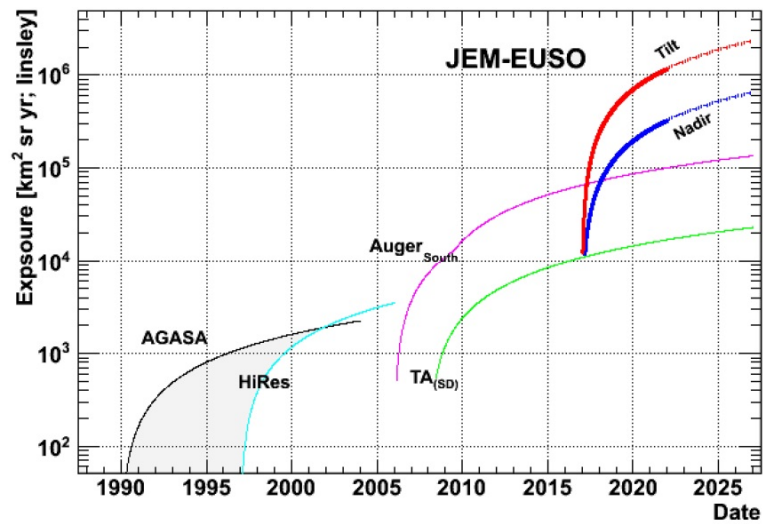


Figure 2.2: A comparison of the estimated JEM-EUSO exposure to that of current and past UHECR observatories. The expectation is that JEM-EUSO will deliver an order of magnitude increase in total exposure compared to both Auger and TA.

- The EUSO-TA project is a joint effort of the JEM-EUSO and Telescope Array collaborations with the aim of placing a small scale JEM-EUSO prototype at the Black Rock Mesa site of Telescope Array. The field of view of EUSO-TA will partially overlap with the one of TA fluorescence detector, allowing the simultaneous observation of Extensive Air Showers by both experiments.
- The EUSO-Balloon instrument is a similar reduced-scale prototype of JEM-EUSO, which was launched with a stratospheric balloon. EUSO-Balloon is a project of the French space agency, Centre National d'Études Spatiales (CNES), and was built as a technology demonstrator for the hardware and methods to be used in the full space mission. The main objective of EUSO-Balloon is to measure the UV background looking down from an altitude of 40 km.
- Mini-EUSO is a special project to place a very small version of the JEM-EUSO detector inside the ISS, observing the atmosphere through an UV transparent window. One of the important issues of Mini-EUSO is the significant increase of the technological maturity levels required for several innovations necessary for JEM-EUSO, developing several components upstream in this small demonstrator, including having the opportunity to test them in space. The second issue of this demonstrator will be its ability to produce unpublished data, paving the way for a family of large-scale projects.

This chapter is devoted to an analysis of the scientific goals of JEM-EUSO and its innovations compared to the other observatory of EECR. Then a detailed description of the operating principles of the telescope and its main components will be presented, paying particular attention to the timing and synchronization system and to its links with the electronics of the focal surface. The information presented here on JEM-EUSO is taken from work done by the entire collaboration, which can be found in [] and the references therein.

2.1 Science Objectives

JEM-EUSO has been designed to address basic problems of fundamental physics and high-energy astrophysics investigating the nature of the Extreme Energy Cosmic Rays, EECRs ($E > 5 \times 10^{19}$ eV), which constitute the most energetic component of the cosmic radiation.

JEM-EUSO will pioneer the investigation from Space of EECR-induced Extensive Air Showers (EASs), making accurate measurements of the primary energy, arrival direction and composition of EECRs, using a target volume far greater than is possible from the ground. Such data will shed light on the origin of the EECRs, on the sources that are producing them,

on the propagation environment between the source and the Earth and, possibly, on the particle physics mechanisms at energies well beyond the ones achievable in man-made accelerators. In addition, the scenario of the JEM-EUSO science goals is completed by several exploratory objectives such as the constraining the Galactic and extragalactic magnetic fields, the detection of extreme energy neutrinos and gamma rays, the verification of special relativity at extremely large Lorentz factors, the examination of possible quantum gravity effects at extreme energies, and the systematic surveillance of atmospheric phenomena.

2.1.1 Main Objective: Astrophysics through the Particle Channel

The main objective of JEM-EUSO is to begin the new field of particle astronomy and astrophysics using the extreme energy particle channel ($10^{19.5} \text{ eV} < E < 10^{21} \text{ eV}$). JEM-EUSO can reach almost full efficiency for a restricted subset of events at energies around $5 \times 10^{19} \text{ eV}$, and for the full aperture at energies $E \gtrsim 6 - 7 \times 10^{19} \text{ eV}$. The expected annual exposure of JEM-EUSO around 10^{20} eV for the full sample of data is expected to be of more than $6 \times 10^4 \text{ km}^2 \text{ sr yr}$, which is about 9 times larger than the annual exposure of the Pierre Auger Observatory which is of about $7000 \text{ km}^2 \text{ sr yr}$. This will permit to achieve about $3 \times 10^5 \text{ km}^2 \text{ sr yr}$ above 10^{20} eV during five years of operation [?]. Such a great exposure will make possible the following targets:

- unprecedented anisotropy studies;
- high precision measurement of the energy spectrum not only for the whole sky, but for different directions over the celestial sphere to constrain acceleration or emission mechanisms;
- identification of individual sources by high-statistics arrival direction analysis.

As we saw in the first chapter, only a few astrophysical candidates are known which can attain the energy of EECRs with the acceleration mechanisms we are presently aware of. This fact makes mandatory the identification of both, sources and powering mechanisms at play.

As they traverse cosmological distances, UHECRs lose energy through interactions with cosmic photon backgrounds limiting the observable horizon to about 100 Mpc for energies above 60 EeV (see paragraph ??). The horizon effect limits the number of sources contributing to the observed flux for proposed source models. This decrease in source number translates into an increase in anisotropies at the highest energies making source identification easier above energies of about 80 EeV. Thus, JEM-EUSO can discover the closest sources by a significant increase in statistics at extreme energies.

The expected sky map of events that will be observed by JEM-EUSO depends strongly on the primary composition and the density of sources, in addition to other model parameters such as the injected spectrum and E_{max} . It is broadly accepted that the particles have an extragalactic origin, but the observed spectrum, composition, and lack of strong anisotropies impose additional requirements. In particular, the lack of anisotropies towards the Galactic plane implies an extragalactic origin for protons above $\sim 10^{18}$ eV and above $\sim 10^{21}$ eV for nuclei with charge Z , as discussed by [?] based on Auger limits on the dipole amplitude and reasonable models of Galactic magnetic fields.

In addition to the significantly increased exposure, an advantage of an orbiting observatory, such as JEM-EUSO, with respect to a ground observatory is the full sky coverage. An all-sky survey offers access to large scale multipoles such as dipoles and quadrupoles which are challenging for observations with partial sky coverages [] (see chapter ??). For example, a partial sky map may be unable to distinguish a dipole from a quadrupole depending on the orientation, while a full sky survey with the same statistics can distinguish the two cases.

Apart from the large aperture and the full sky coverage, the merit of JEM-EUSO is to be relatively free from the problems which ground-based experiments have. Fluorescence telescopes, including JEM-EUSO, measure the electromagnetic component that carries 90% of the energy of EAS. Observing from Space, JEM-EUSO telescope may capture EASs that develop at high altitudes (above 20 km), where the Landau-Pomeranchuk-Migdal effect does not work due to the low atmospheric density (see chapter ??). Achieving high accuracy in energy determination and high statistics will allow to discover more on the origin and propagation of the EECR. At the moment, JEM-EUSO is the only project able to reach such expected scientific outcomes, which will initiate the new astronomy through the particle channel.

2.1.2 Exploratory Objectives

Aside from the primary scientific objectives, several exploratory objectives in astrophysics have been set for the JEM-EUSO mission. These are areas to which the experiment may contribute, depending on the actual nature of the EECR flux, and include:

- the study of the UHE neutrino component which can be achieved by discriminating weakly interacting events through the position of the first interaction point and of the shower maximum;
- the discovery of UHE Gamma-Rays, whose shower maximum is strongly affected by the geomagnetic and LPM effects;

- the study of the Galactic and local extragalactic magnetic fields, through the analysis of the “magnetic point spread function” of one or more identified sources.

In fact, EECR propagation through the cosmic background radiation produces Extreme Energy Gamma-Rays (EEGRs) and neutrinos ($EE\nu$ s) as a natural consequence of π_0 and charged π production respectively (usually called cosmogenic photons and neutrinos). The attenuation length for EEGRs is very short depending on the Cosmic Radio Background. The expected flux of EEGRs on Earth is small and highly model dependent, (e.g., nuclei primaries produce much fewer gamma-rays than proton primaries). JEM-EUSO will search for EEGRs events and place stronger constraints on their flux [66] [65]. A detection of a flux higher than expected can be due to a new production mechanism such as top-down decay or annihilation [67], or the breaking of Lorentz Invariance.

Concerning the $EE\nu$ s, since the flux of cosmogenic neutrinos around 10^{20} eV is highly dependent on E_{max} of cosmic rays, a flux of cosmogenic neutrinos is within reach of the JEM-EUSO mission if E_{max} is high enough [63]. A neutrino flux from extremely energetic sources may also be observed by JEM-EUSO. Because the acceptance for $EE\nu$ s events is well above current ground detectors. Finally, JEM-EUSO will have an order of magnitude larger acceptance results for Earth-skimming events transiting ocean compared to transiting land, as is discussed in [64]. Since ground-based observatories cannot observe ocean events, only space-based missions can realize the advantage of this possible enhancement of the acceptance over the ocean.

In addition to the astrophysics objectives of the mission, JEM-EUSO would also be able to contribute in several areas of atmospheric science due to its continuous monitoring of the Earth’s atmosphere in the UV band (290 - 430 nm). JEM-EUSO will allow a characterization of atmospheric night-glow and of Transient Luminous Events (TLE). JEM-EUSO would also be able to detect the slow (compared to EAS) UV tracks created by meteors and meteoroids, with important scientific outcomes.

The observing strategy developed for JEM-EUSO to detect atmospheric and meteor events will also be sensitive to other hypothetical slow velocity events such as nuclearites or massive strangelets (quark nuggets with a fraction of strange quarks similar to up and down quarks). JEM-EUSO is sensitive to nuclearites with mass $m > 10^{22}$ GeV/ c^2 . A null observation of these events will set strong limits on their flux, reaching one order of magnitude more stringent limits than current ones in only one day of observations [68].

2.2 Observation Principle and Requirements

In order to meet the scientific goals, a list of instrumental requirements have been determined. The current design of the JEM-EUSO instrument is foreseen to meet or exceed all following requirements. The statistics collected by the experiment should be of the order of several hundred events above 7×10^{19} eV, which implies a total exposure of more than $10^5 \text{ km}^2 \text{ sr yr}$ over three years. The angular resolution of the telescope should be better than 3° for EAS of energies greater than 8×10^{19} eV. Similarly, the energy resolution, as a 68% interval, should be better than 30% for EAS of energy above $E_0 = 8 \times 10^{19}$ eV. JEM-EUSO will have the capability to distinguish between nuclei, gamma rays, and neutrinos, which would require a determination of X_{max} with an uncertainty of less than 120 g/cm^2 at $E_0 = 10^{20}$ eV for showers at zenith angles of 60° . As JEM-EUSO will be placed on the ISS, it will observe the full sky with much less than 30% nonuniformity between hemispheres, which is ideal for anisotropies studies.

An EECR of about 10^{20} eV produces an EAS with approximately 10^{11} particles in the region of the shower maximum. Secondary charged particles, predominantly electrons, deposit their energy in the atmosphere, exciting atmospheric nitrogen molecules and causing the emission of UV fluorescence photons. The UV light emitted allows the detection of EAS by the air fluorescence technique, discussed in chapter ??.

From its orbit on the ISS, at an altitude of ~ 400 km, JEM-EUSO would detect the fluorescence light and Cherenkov emission from EAS occurring in its FoV. The basic observation principle of the telescope is shown in Fig. 2.3. The fluorescence light from the EAS is emitted isotropically along the shower track and traces the longitudinal development of the EAS; it is observed directly. The Cherenkov radiation, on the other hand, is forward-beamed and it is emitted in a cone around the axis of the EAS. The Cherenkov light seen by JEM-EUSO would be that which was either scattered by the atmosphere or reflected off the ground or a cloud top. The reflected signal is known as the ‘‘Cherenkov mark’’ and provides additional information about the geometry of the shower.

The air fluorescence yield has been intensively studied by many groups and is found to be $\sim 3 - 5$ photons m^{-1} per electron. During the development of a 10^{20} eV EAS, an order of 10^{15} photons are emitted. Seen from ~ 400 km distance the number of photons which actually reach the telescope will be strongly attenuated, the solid angle subtended by a telescope with a few m aperture is of the order of 10^{-11} sr. This implies several thousands of photons will reach the entrance aperture of the telescope from each EAS in the field of view in a time window of about one hundred μs , under clear atmospheric conditions. Given the throughput of the JEM-EUSO optics and the quantum efficiency of the photodetector (see Table 3.1), these several thousand photons will yield several hundred photoelectrons. As each pho-

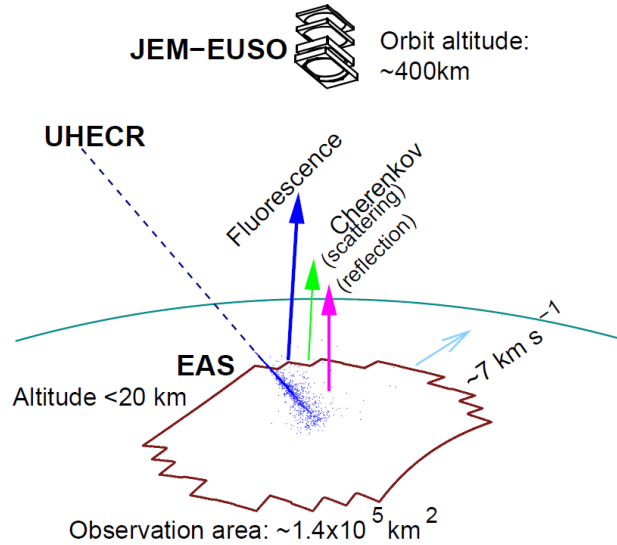


Figure 2.3: Illustration of UHECR observation principle in the JEM-EUSO mission. For the telescope at $H_0 \sim 400$ km altitude, the main signals are fluorescence photons along the EAS track and Cherenkov photons diffusely reflected from the Earth's surface.

toelectron registered occupies ~ 8 ns, the focal surface of JEM-EUSO will operate in single photoelectron counting mode.

The distribution of photons at the entrance aperture from an EAS originated by a primary with an energy of 10^{20} eV according to arrival time is shown in Fig. 2.4. As can be seen, the shower develops over a time span of 200 μ s. The fluorescence light, shown by the solid blue, is the dominant contribution to the signal. It is also the most prompt part of the signal to arrive at the telescope. The Cherenkov contribution, on the other hand, is lower and arrives later in time. The Cherenkov reflection, shown in Fig. 2.4 by the red area provides a time mark for the end of the shower and thus gives information on the altitude of the reflection. The domination of the fluorescence signal (for low albedo) allows the energy of the UHECR to be determined with only small corrections for the Cherenkov component. At the same time, the Cherenkov light reflected from ground or cloud-top is useful for providing a time mark for the terminus of the shower.

Since JEM-EUSO is at an altitude of around 400 km, the shower maximum, which generally occurs below 20 km altitude (~ 10 km in Fig. 2.4), will be at an almost constant distance for a given location of the EAS in the field of view, regardless of the direction of the EAS. This greatly reduces the importance of proximity effects in the shower reconstruction. The fixed distance and the domination of the fluorescence component, are beneficial characteristics of observation from space. For these reason, JEM-EUSO can be seen as essentially turning a volume of atmosphere into a Time Projection

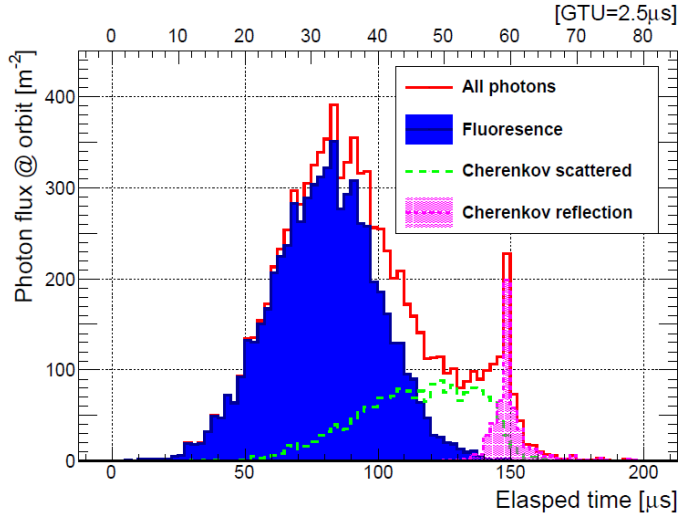


Figure 2.4: Arrival time distribution of photons at the entrance aperture for a standard EAS with $E = 10^{20}$ eV at an angle of 60° (from simulations). The fluorescence light is the dominant component, with smaller contributions coming from reflected and back-scattered Cherenkov light. The end of the shower (on the ground or a cloud top) is marked by reflected Cherenkov light. As can be seen, the development time of the EAS is on the order 200 μs .

Chamber in which the drift velocity is that of light.

2.3 The JEM-EUSO system

The JEM-EUSO system consists of a Flight Segment, Ground Support Equipment (GSE), Ground Segments (GS), a Global Light System (GLS) and a science data center which are shown in Fig. 2.5.

The Flight Segment mainly consists of a science instrument system which basically consists of the following elements:

- the JEM-EUSO telescope which is a large diameter telescope to observe EECR;
- the Atmospheric Monitoring System (AMS);
- the Calibration System.

These systems will be described in the following sections.

GSE consists of mechanical, electrical, optical and calibration GSE. GSE supports the project during the manufacturing of the Flight Segment.

The GS consists of Launch Site Operation and Mission Operation Control and supports launching and mission operation.

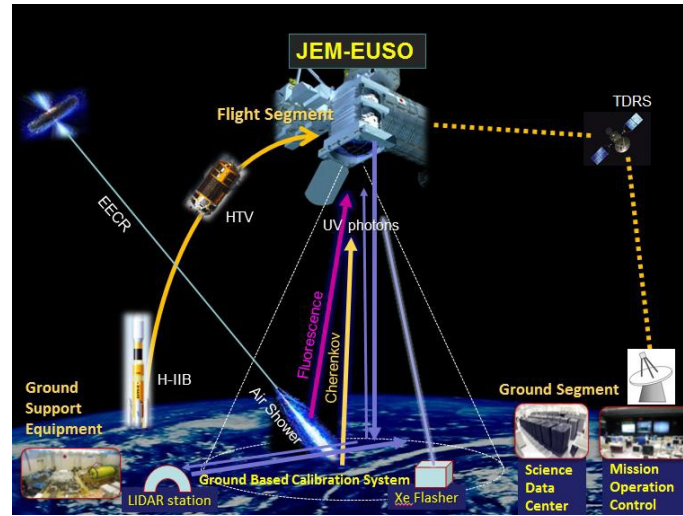


Figure 2.5: A conceptual overview of the JEM-EUSO mission from launch by H-IIIB (or SpaceX) to attachment on the International Space Station.

The GLS would be a world-wide network combining ground-based Xenon ash lamps and steered UV lasers, which will be used to generate known optical signatures in the atmosphere with similar optical characteristics to EAS and with a known event energy, time, and direction. The GLS will be used to calibrate the instruments while the mission is in operation by using a dozen of Xenon flashers installed on the ground. There are planned to be 12 ground based units placed at sites around the world, with six locations equipped with Xenon ashers only (GLS-X) and six equipped with both ashers and remotely operated steerable lasers (GLS-XL). The future GLS sites will be chosen for low background light and an altitude above the planetary boundary layer. The calibration will be done about once a day at each station, when JEM-EUSO passes overhead. Ultraviolet lasers from the ground LIDAR stations are also foreseen as a part of the GLS.

Data taken by the Science Instrument System on the ISS will be sent to a Mission Operation Control (MOC) on the ground through a Tracking and Data Relay Satellite (TDRS), and then to a science data center.

The current baseline mission plan is that JEM-EUSO will be launched by a Japanese HIIIB rocket and transported to the ISS by an unmanned H-IIB Transfer Vehicle (HTV). The accommodation of JEM-EUSO in the HTV requires that the telescope be cut on two sides so that the maximum diameter of the lenses is 2.65 m and the minimum diameter is 1.9 m. Another recent launch possibility, however, is the use of the SpaceX Dragon as transfer vehicle. The accommodation of JEM-EUSO in the trunk section of the SpaceX Dragon Spacecraft will require slight modifications to the instrument and an optimization of the instrument shape and size. This would

include a return to a circular shape.

In either case, the instrument will then be attached, using the Canadian and Japanese robotic arms, to one of the ports for non-standard payloads of the Exposure Facility (EF) of the JEM. In order to be accommodated in either the HTV or the Dragon, the JEM-EUSO instrument will be stored in a folded configuration during launch and transport, and the telescope will be deployed after the attachment procedure is completed. Data from the JEM-EUSO mission will be transmitted via Tracking and Data Relay Satellite (TDRS) to a Mission Operation Center hosted by JAXA in the Tsukuba Space Center and managed by RIKEN with the support of the collaboration. It is also planned to establish several data centers in the major participating countries. According to the currently planned mission profile, JEM-EUSO should be operated for one to three years in a Nadir configuration, i.e. looking directly towards the ground. This would be done to maximize the number of events at the lowest energies so that the cosmic ray spectrum measured by JEM-EUSO overlaps well with that measured by the current generation of ground-based detectors, because the acceptance for low energy events is better in Nadir configuration. Then the instrument will be tilted (by up to 35 degrees) with respect to Nadir, to increase the viewed volume of atmosphere and maximize the event statistics at the highest energies.

During flight, JEM-EUSO will be calibrated by an on-board calibration system, which will check for changes in photodetection efficiency and lens throughput relative to the precise on-ground calibration.

2.4 The telescope

The JEM-EUSO telescope is an extremely-fast and highly-pixelized ($\sim 3 \times 10^5$ pixels) digital camera with a large diameter (2.35 m) and wide Field of View (FoV, $\pm 30^\circ$), working in near-UV wavelength range (290 - 430 nm). The instrument has a single photon counting capability, but is also capable of switching to charge integration mode in case of strong illumination. The telescope consists basically of four main components (Fig. 2.6):

- optics: three high transmittance optical Fresnel lenses focusing the arriving UV photons onto the Focal Surface (FS);
- the FS detector, made up of about 5000 Multi Anodic PhotoMultipliers Tubes (MAPMT) of 64 pixels;
- the FS electronics, which includes the front-end electronics and the subsystems performing trigger, data acquisition and controls;
- the mechanical structure.

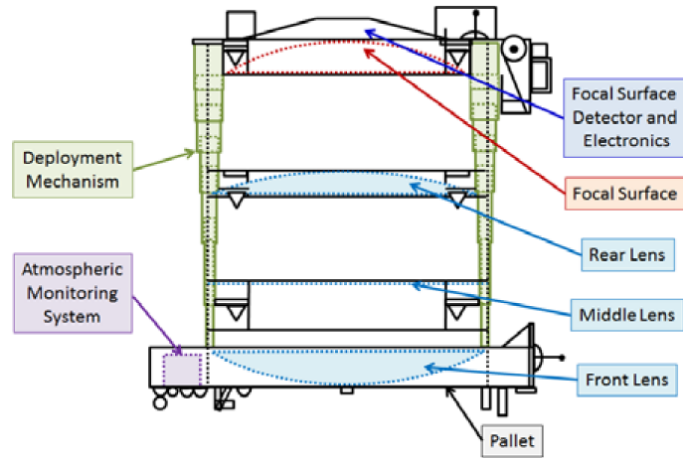


Figure 2.6: A conceptual overview of the JEM-EUSO instrument after deployment. The telescope is composed of three lenses, a focal surface with electronics, and an atmospheric monitoring system. All of these are mounted on a transport pallet. The instrument is transported in a vertically collapsed configuration and expanded after attachment.

Each of these components will be presented in turn in the next paragraphs. The mission parameters give strict limits on the weight and power budget of the instrument, which heavily influence the chosen designs.

2.4.1 Optics System

JEM-EUSO optics focuses the incoming photon toward a pixel of the detector set on the optical focal surface. The collection of photons by the optics requires:

- Field of View (FoV) of optics larger than $\pm 30^\circ$;
- Entrance Pupil Diameter (EPD) on axis: 2.3 m;
- Focal number $f/\# = 1.25$;
- Spot size smaller than the pixel size of the FS detector.

The large FoV is required to view as much of the atmosphere as possible, in order to retrieve enough statistics of the rare most energetic events; the pupil aperture must be as big as possible in order to detect the faint fluorescence and Cherenkov photons with enough signal; the system must be as fast as possible (i.e. small $f/\#$) in order to have an acceptable focal surface in terms of dimensions and weight.

The optic system of JEM-EUSO foresees three plastic lenses. The first and the third lens are each curved double-sided Fresnel lenses with an external diameter of 2.65 m. The middle lens has a curved precision Fresnel lens

on one side with a diffractive optical element on the other and was added to the design in order to correct the chromatic aberration. The combination of these three lenses gives a full angle FoV of 60° and an angular resolution of 0.07° . This resolution corresponds to 550 m on the ground at an altitude of 400 km in the Nadir configuration.

A system of plastic Fresnel lenses was chosen because a light-weight design is mandatory for a space mission. In addition, the Fresnel-type lens have the advantage of a higher transmission factor, which is critical when observing only several thousands of photons from a given EAS.

Two possible lens materials have been studied, CYTOP and PMMA-000. CYTOP (basically transparent Teflon) provides less dispersion, higher transmittance, and a generally lower refractive index than PMMA-000. CYTOP also has a greater resistance to damage caused by exposure to atomic oxygen in orbit. At the same time, CYTOP is more expensive and heavier than PMMA. The baseline design is for all three lenses to be made from PMMA, while the advanced design is for the front lens to be made of CYTOP with the inner two lenses made of PMMA. Each of these designs is shown in Fig. 2.7.

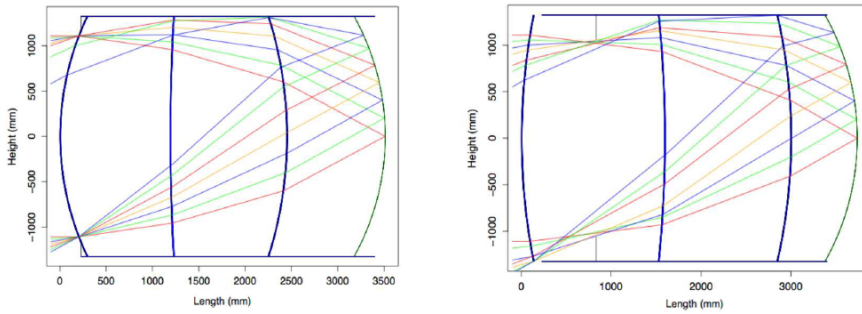


Figure 2.7: Ray tracing simulations of the Baseline, on the right, and Advanced, on the left, optics designs. The baseline design is a three lens system with each lens made of PMMA. The advanced design uses the same number of lenses, but with the first lens being made of CYTOP.

A full-scale set of JEM-EUSO lenses, i.e. a so-called Bread Board Model (BBM), has been manufactured at RIKEN using a large ultra-precision (~ 4 nm) diamond turning machine. The optics requirements are shown in table 3.1, and include a point-spread function of less than 5 mm, to be compared to a pixel size of 2.88 mm, and a throughput of 50% at normal incidence. The BBM was tested at Marshall Space Flight Center in Huntsville, Alabama, and was found to meet or exceed all the optics system requirements.

2.4.2 Focal Surface

The Focal Surface (FS), shown in Fig. 2.8, is the heart of the JEM-EUSO instrument. The FS main components are the FS Detector and the FS Elec-

Table 2.1: Optics requirements and specifications of both the baseline and advanced optics designs.

	Requirements	Baseline Optics	Advanced Optics
f/# (F number)	< 1.25	1.0	1.0
Lens diameter [m]	≥ 2.5	2.5	2.5
Spot size (RMS) [mm]	≤ 5	5.0	5.0 (2.5)
Throughput	50% @ $0^\circ \div 10^\circ$	59% @ $0^\circ \div 10^\circ$	62% @ $0^\circ \div 10^\circ$
	40% @ $10^\circ \div 20^\circ$	52% @ $10^\circ \div 20^\circ$	58% @ $10^\circ \div 20^\circ$
	30% @ $20^\circ \div 30^\circ$	39% @ $20^\circ \div 30^\circ$	42% @ $20^\circ \div 30^\circ$
Filter transmittance	$\geq 90\%$	$> 90\%$	$> 90\%$

tronics, both of them will be described in more details in the next paragraphs.

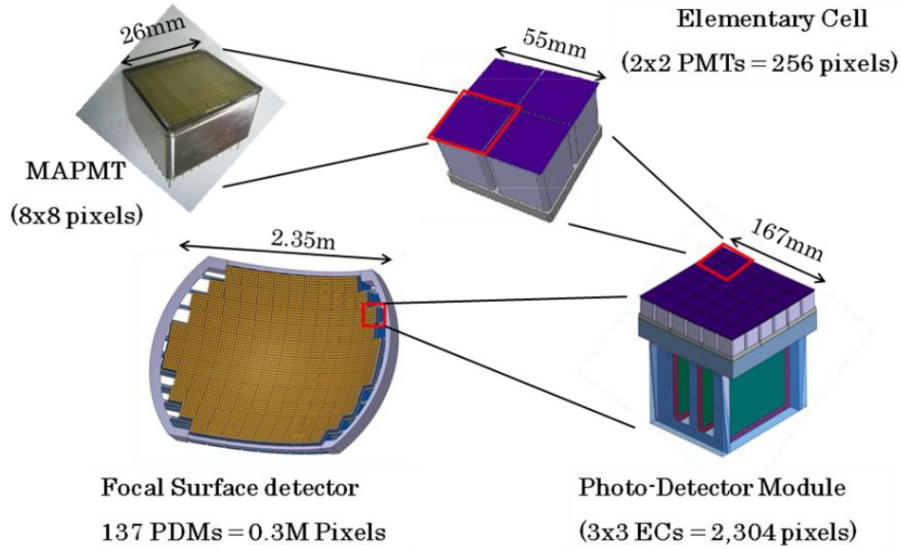


Figure 2.8: A conceptual breakdown of the JEM-EUSO focal surface. The total focal surface is made of 137 Photodetection Modules (PDM). Each PDM is made of 9 Elementary Cells (EC) and their read-out electronics. Every EC is composed of 4 Multi-Anode PhotoMultiplier Tubes, each having 64 pixels.

The surface of the FS Detector is accommodated on the focal surface of the optics. It has a curved surface of about 2.35 m of diameter, covered with more than 5000 Multi-Anode PhotoMultiplier Tubes (MAPMTs). The FS detector consists of Photo-Detector Modules (PDMs), each of which consists of 9 Elementary Cells (ECs), the smallest flat surface of the detector, arranged in an array of 3×3 . About 1,233 ECs, corresponding to 137 PDMs, are arranged on the whole FS. Each MAPMT is read-out through a dedicated Application Specific Integrated Circuit (ASIC), which is the first level of the

front-end electronics.

Data acquisition is based on a hierarchical architecture designed to reduce at each level the amount of data through a series of triggers controlling an increasingly growing area of the focal surface. It is necessary to pass from the ~ 10 GB/s on the Focal Surface to the ~ 10 kb/s which can be down-linked on the ground.

The Data Acquisition and Handling System is designed to maximize the detector observation capabilities to meet the various scientific goals, but also to monitor system status, autonomously taking all actions to maintain optimal acquisition capabilities and handle anomalies. Rad-hard technology will be employed, with ground beam tests to qualify and test resistance of new devices; in addition, space qualified devices will be employed wherever required by safety and agency requirements. Particular care is devoted to the use of off-the-shelf technologies in the development of the laboratory models and breadboard systems used to refine and test the various trigger and data reduction algorithms. The same approach is followed in the choice of communication protocols and interfaces (VHDL, SpaceWire) and in the realization of the Ground Support Equipment. Hot/Cold redundancy will be implemented in all systems and in all stages of data processing with the exception of intrinsically redundant devices such as the focal surface detectors.

2.4.2.1 FS detector

The photodetector in JEM-EUSO has to be fast, with high pixel density and detection efficiency and single photon counting capability in near-UltraViolet (UV) wavelength region with a low background count rate. In addition, it should be reliably and stably operational in Space environment for at least 3 or 5 years mission period. For the above reasons, a multianode vacuum photomultiplier tube with UV-glass entrance window is the preferred photodetector. The chosen photodetector is the Hamamatsu R11265-M64 multi-anode PMT (Fig. 2.9), which has been developed for JEM-EUSO as a collaboration between Hamamatsu Photonics and RIKEN. The M64 has 64 individual pixels, each 2.88 mm^2 , and an ultra bialkali photocathode with a quantum efficiency of 35-45% for light in the 290 to 430 nm wavelength range. The MAPMT amplifies photoelectrons by means of a stack of 12 metal channel dynodes, with typical gains of 10^6 at a cathode voltage of 900 V.

Since the rate of photons from an EAS on the focal surface is extremely low, the best read-out strategy is to use photon counting. This means counting the individual anode pulses coming from the collection and multiplication of single photoelectrons. At the same time, the observation of other atmospheric phenomena, such as TLE, implies a photon flux several orders of magnitude larger. In this situation, the arrival rate of photons is such that

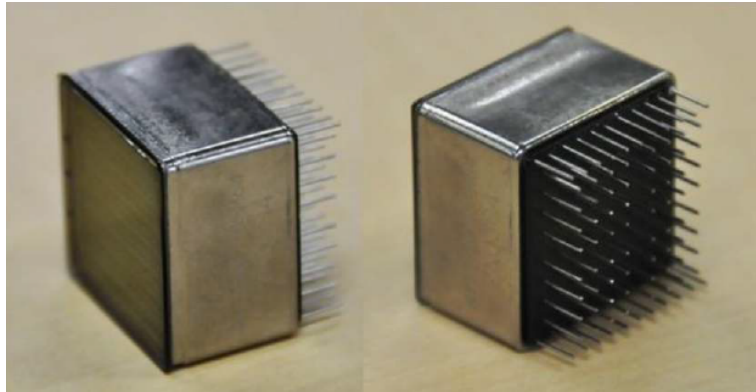


Figure 2.9: Two photographs of the Hamamatsu R11265-M64 multi-anode PMT, taken from two different angles. On the left side, the photocathode of the M64 can be seen, along with the pixel structure. On the right, the M64 is turned to show the anode pins. The 11 pins on the top and bottom are the cathode and dynode pins (some pins are repeated).

anode pulses from single photoelectrons will overlap, giving large pulses of light or a DC level, depending on the time profile of the phenomena. To accommodate these two response modes, the front-end electronics contains both a single photoelectron counting part (a preamplifier and discriminator) and a charge integration part.

2.4.2.2 FS electronics

Focal Surface electronics is located inside the FS structure, it includes the MAPMTs control circuits and the data handling electronics. In particular, the main functions of the FS electronics are:

- interface the MAPMTs and provide the first level of trigger (analogue and digital);
- provide further level of trigger, the ring memory buffers and the communication between the FS detector and the control electronics;
- provide the power to the MAPMT (High Voltage Power Supply) and to all the front end electronics (Low Voltage Power Supply).

The front-end electronics has to digitize the output signals of the MAPMTs in successive time slices, called Gate Time Units (GTUs), of $2.5 \mu\text{s}$ each. The length of a GTU was chosen for several reasons. Firstly, since an EAS develops completely in around $200 \mu\text{s}$, the read-out should be on the microsecond scale. A higher read-out rate, however, implies a larger front-end electronics power consumption and a greater difficulty in design. Another motivation is that, since the size of a single JEM-EUSO pixel projected on the ground is

0.5 km, the length of one time slice of $2.5 \mu\text{s}$ at the speed of light is roughly comparable to the lateral size of a pixel on ground.

The first level of the front-end electronics is the read-out ASICs of each MAPMT. The ASIC contains both an analog part which handles the 64 anode signals from the phototube, and a digital part which returns photon counting and charge integration data. The designed ASIC, called SPACIROC, is a low-power, rad-hard ASIC which is intended for reading out a 64-channel Multi-Anode Photomultiplier and is a result of the collaboration between OMEGA/LAL-Orsay, France, RIKEN, ISAS/JAXA and Konan University, Japan on behalf of the JEM-EUSO consortium. A diagram of the general architecture of the SPACIROC ASIC is shown in Fig. 2.10. Each of the 64 pixels of the MAPMT go through a integrating pream-

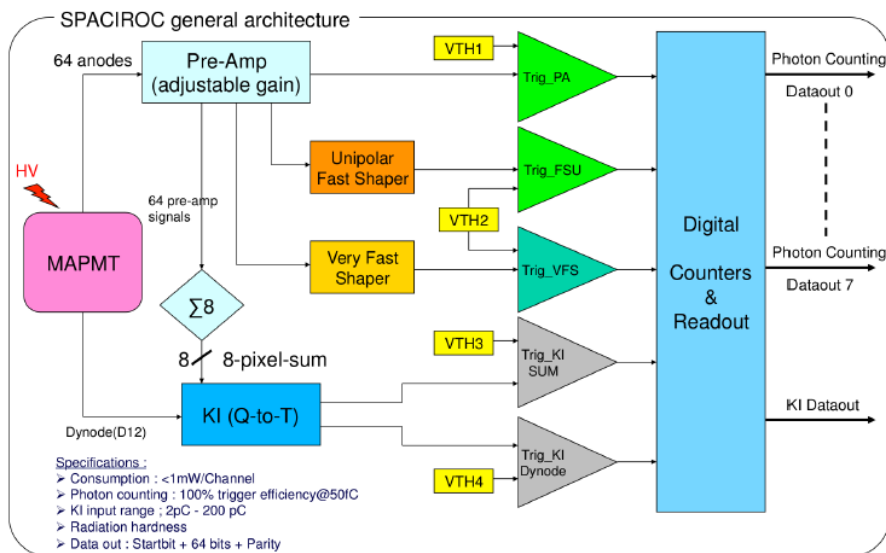


Figure 2.10: A diagram of the general architecture of the SPACIROC ASIC. Each of the 64 pixels of the MAPMT go through a integrating preamplifier with an adjustable gain. The signals are then sent through a unipolar fast shaper and on to discriminator (Trig FSU). The number of counts over threshold is returned each GTU for all 64 pixels. At the same time, the SPACIROC includes a time over threshold charge integrator (KI) which takes the sum of 8 pixels. This read-out mode is used for phenomena which give a large illumination.

plifier with an adjustable gain. The signals are then sent through a unipolar fast shaper and on to discriminator (Trig FSU). At the end of each GTU, the ASIC related to each MAPMT returns the number of pulses over a set threshold in each of the 64 pixels into a ring memory while waiting for trigger assertion. For large signals, the charge in a group of 8 pixels is returned using a time over threshold method. A few properties of the ASIC are listed in the bottom-left corner of the figure.

The overall JEM-EUSO trigger philosophy is at the core of the concept of the instrument. The goal of the trigger system is to detect the occurrence of a scientifically valuable signal among the background noise detected by the JEM-EUSO telescope. Since the total number of pixels in the array is very large ($\sim 3 \times 10^5$), a multi-level trigger scheme has been developed.

The general JEM-EUSO trigger philosophy foresees a trigger system organized into two main levels. The two levels of trigger work on the statistical properties of the incoming photon flux in order to detect the physical events hindered in the background, basing on their position and time correlation. This scheme is necessary to extract real EAS events from the background and to reduce the overall data rate to fit within the limited budget. An overview of the data processing scheme is shown in Fig. 2.11. The raw data

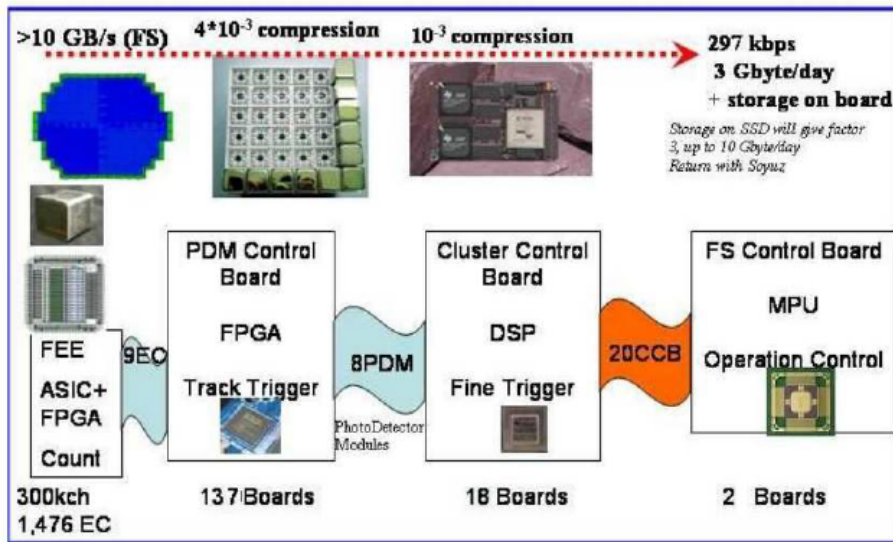


Figure 2.11: A diagram of the data handling in JEM-EUSO. Since it is a space mission, the data budget available is extremely limited, requiring a large reduction in data rate between the raw focal surface read out and event data. There are two triggers, one at the PDM level, and one at the CCB level, as described in the text. There are a total of 20 CCB, each controlling at most 8 PDMs. Using this trigger scheme the expected data rate is reduced from 10 GB/s to 297 kb/s.

raw of more than $\sim 10 \text{ GB/s}$ is reduced at each level down to a final data rate of $\sim 297 \text{ kb/s}$ for storage or down-link to the ground operation center. This trigger scheme relies on the partitioning of the Focal Surface in subsections, named PDM (Photo Detector Module), which are large enough to contain a substantial part of the imaged track under investigation (which depends on the energy of air shower and the zenith angle).

The counting and charge integration output of each ASIC are passed on to the PDM electronics boards. The PDM boards are grouped into units of eight, each unit is controlled by a Cluster Control Board (CCB), in this way

the detector is subdivided in 18 clusters.

The PDM board implements the first level trigger in order to reduce the overall data rate. The first level trigger is designed to reject the majority of background fluctuations by requiring a locally persistent signal over a predefined threshold during the course of several GTUs. If the first level trigger is issued, then the photon counting data in the ring buffer of the PDM is requested by the CCB, which implements the second level trigger.

The readout procedure is started according to the second level trigger, issued at the cluster level. The algorithm working as a second level trigger, presently proposed for JEM-EUSO, is called “Linear Track Trigger” method (LTT) and searches for light points moving with the light speed at 400 km ahead. The photon count along each predefined line through the PDM is integrated across GTUs, and, if the integration along any direction exceeds a preset threshold, then the LTT is issued. If the LTT trigger is issued, then the data from an entire cluster of 8 PDMs is saved, along with data from the atmospheric monitoring system. The threshold of the LTT depends on the background rate, and is tuned to reduce the event rate (including fake triggers) to about 0.1 Hz over the whole FS.

The CCB interfaces the PDMs with the Data Acquisition and Handling System. More in details, every CCB is connected to PDMs, Data Processor (DP), Housekeeping System (HK) and Timing and Synchronization System (CLK-Board). These systems will be described more in details in the next sections.

2.4.2.3 The data acquisition and handling system

The data acquisition and handling system is designed to maximize detector observation capabilities to meet the various scientific goals, monitor system status, autonomously taking all actions to maintain optimal acquisition capabilities and handle off-nominal situations. The data handling electronics includes Mission Data Processor (DP), Telemetry Command Unit (TCU), Data Acquisition Interface (IDAQ) and the Timing and Synchronization System (CLK-B). All of these electronics systems must be radiation hard in order to operate correctly in a space environment for 5 years and must run on a limited power budget.

Main DP tasks are:

1. power ON/OFF of all subsystems;
2. perform periodic calibrations;
3. acquire observation data from the FS detector and atmospheric monitor;
4. define trigger mode acquisition;

5. read Housekeeping data related to the mission system;
6. take care of real time contingency planning;
7. perform periodic download/downlink;
8. handle slow control commands.

The communication between CPU, CCBs and CLK-Board will be realized with a SpaceWire interface due to its proved reliability. In the current baseline, the interface runs at 200 MHz, which translates into a data rate of 200 Mbit/sec. The complete data traffic between the CPU and the other subsystems will take place over this interface in form of standardized data packets. All messages to CPU will be provided with a 4-byte large CRC in order to allow the CPU to assure their data integrity.

2.4.2.4 Timing and Synchronization System

In the previous paragraphs it has been showed that the apparatus is segmented in various zones; in each of these zones, different units process independently different sets of data. In order to correctly assign to an event all its own data sets, it is mandatory to perfectly synchronize the whole system and to tag properly the data sets. This task will be accomplished by the Timing and Synchronization System of JEM-EUSO, which will be made up by the clock and time synchronization board (CLK-board) and a GPS receiver.

The CLK-board is the part of the data processor devoted to generate and to distribute the system clock (40 MHz), the GTU clock (400 kHz) and the synchronization signals to all devices of the Focal Surface electronics in order to provide time synchronization of the events. The master clock is generated by a 40 MHz Temperature Compensated Crystal Oscillator capable of a frequency stability of ± 1 ppm in the temperature range of -40°C to 85°C . The GTU clock is obtained from the master clock.

Furthermore, the board generates and receives all the signals needed to control the timing of data acquisition. Another important task of the CLK-Board is the management of trigger signals. The CLK board receives the second level trigger signal from CCBs and forwards to CCBs any trigger signal coming from CPU. The CLK-Board implements also the logic to measure the fraction of live time and dead time of the apparatus.

The board has an interface with the GPS receiver which allows to collect, for each event, information on the position of the instrument and the UTC time with a precision of few microseconds. The CLK-board is connected to the GPS receiver through a serial port in order to collect data and deliver commands according to the NMEA protocol. The 1PPS pulse generated by the GPS receiver is used in order to synchronize, at level of 1 GTU, the apparatus with the UTC time.

The board receives commands from CPU and transmits/receives data to/from the CPU by using the SpaceWire communication protocol and is interfaced with the Housekeeping System, which monitors temperature and alarms of the CLK-Board.

The design and the development of the Time and Synchronization System for the JEM-EUSO pathfinder has been one of the main part of this thesis work and it will be described widely in chapter ??.

2.4.2.5 Housekeeping System

The aim of the Housekeeping System (HK) is to monitor and to relay control commands to the subsystems which constitute the JEM-EUSO instrument [?]. The HK has to perform several tasks:

- sensor monitoring of different subsystems in order to detect faults;
- generation of alarms for the CPU;
- distribution of telecommands to subsystems;
- temperatures and voltages acquisition from all the subsystems;
- monitoring of the status of the electronics of the FS;
- switching between main and spares boards when needed;
- interaction with the power distribution system of the telescope, in order to turn ON and OFF the secondary power supplies, and therefore the FS, and to verify adequate levels of power consumption.

In order to distribute commands to the various subsystems and to collect telemetry to monitor in real-time the status of the detector and optimize its observational parameters, the HK is directly interfaced with the CPU. Commands received and executed by the HK can be either generated by the CPU itself or sent from ground through the CPU. The module is capable of handling single, periodic and time-tagged instruction according to the CPU commands. All the subsystem anomalies detected by the HK are reported as alarms to the CPU. All the activities of the HK are defined as slow control, i.e., with reaction time scales typically larger than a second. The HK subsystem architecture is conditioned by the wide variety of subsystems that constitute the JEM-EUSO instrument and with which it has to interact.

2.5 Atmospheric Monitoring System

The aim of the Atmospheric Monitoring System (AMS) is to observe the condition of the atmosphere in the field of view of the JEM-EUSO telescope, providing information on the optical properties of the atmosphere and the

distribution of clouds and aerosol layers. Since the amount of both fluorescence and Cherenkov signals reaching JEM-EUSO depends on the extinction and scattering of UV light in the atmosphere, the correct reconstruction of EECR energy and of the type of the primary cosmic ray particle requires information about absorption and scattering properties of the atmosphere. In fact, while extinction leads to the reduction of the overall intensity of the EAS signal as it propagates from the production region toward the detector, scattering properties of the atmosphere at the EAS location determine the amount of Cherenkov light, which is re-directed from the direction along the EAS axis toward JEM-EUSO. In addition, the depth of the shower maximum will be affected by the uncertainty in the determination of the location and physical properties of clouds and aerosol layers, in such a way that uncertainties in the determination of both extinction and scattering properties of these features will directly affect the precision of the measurement of the shower maximum position (X_{max}).

The AMS includes an infrared (IR) camera, a Light Detection And Ranging (LIDAR) system and global atmospheric models generated from the analysis of all available meteorological data by global weather services [60] (see Fig. 2.12).

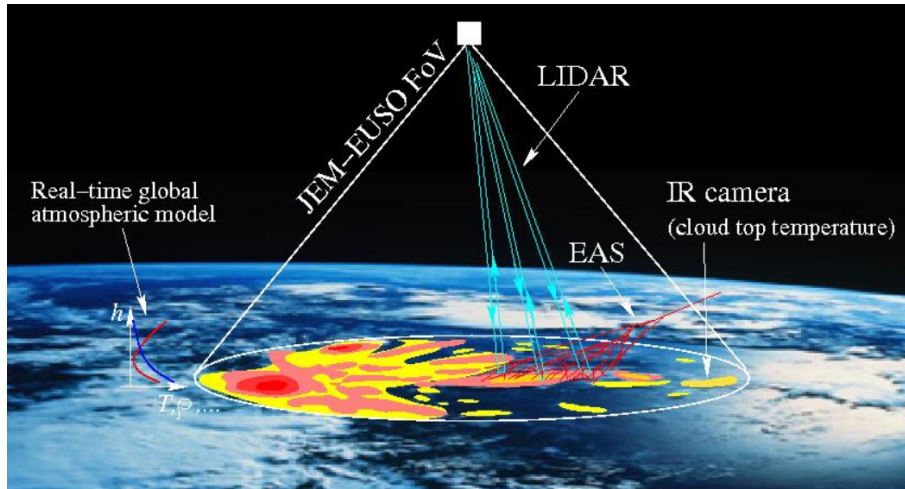


Figure 2.12: A pictorial view of the Atmospheric Monitoring System of JEM-EUSO.

2.6 Calibration System

The calibration system is needed to measure the efficiencies of the optics, the focal surface detector and the data acquisition electronics. These values are needed to determine energy and arrival direction of EECR. The calibration system can be outlined as composed of four part:

- Pre-flight calibration: detection efficiency, uniformity and gain will be measured with UV LEDs [?].
- On-board calibration: to measure efficiencies of FS detector, several diffuse LED light sources with different wavelengths in the near UV region are placed on the support of the rear lens in front of the FS. To measure efficiencies of the lenses a similar light source is placed at the center of the FS. Reflected light at the inner surface of the lid is observed with the FS [?].
- Calibration in flight with on ground instruments: the system will be calibrated with a dozen ground light sources when JEM-EUSO passes over them [?]. The Global Light System (GLS) is a network of ground-based Xenon flashlamps and steered UV lasers. GLS units will generate benchmark optical signatures in the atmosphere with similar characteristics to the optical signals of cosmic ray EASs. The lasers will generate tracks and the flashers will generate point flashes. But unlike air showers, the number of laser and flasher pulses, their energy, precise time, direction (lasers) can be specified. JEM-EUSO will reconstruct the pointing directions of the lasers and the energy of the lasers and flashlamps to monitor the detector triggers, and accuracy of energy and direction reconstruction.
- Atmospheric monitor calibration: the amount of UV absorption in the atmosphere will be measured with Xe flasher lamps. The systematic error in energy and direction determination will be empirically estimated, by observing emulated EAS images with a UV laser by the JEM-EUSO telescope. The transmittance of the atmosphere as a function of height will be also obtained; the IR camera monitors the FoV by periodically taking pictures during observations. The IR data will help to estimate the effective area.

Since an absolute calibration is very difficult to maintain for the whole mission time of JEM-EUSO, it is mandatory to monitor changes in the detector. Therefore the on-board calibration system will be used to do a relative calibration of the detector with respect to the absolute pre-flight calibration.

Chapter 3

The EUSO-Balloon pathfinder

EUSO-Balloon has been developed by the JEM-EUSO consortium as a demonstrator for technologies and methods featured in the space instrument [?]. This balloon-borne instrument points toward the nadir from a float altitude of about 40 km. The instrument monitors a $12^\circ \times 12^\circ$ wide Field of View (FoV).

The EUSO-Balloon mission has been proposed by a collaboration of three French laboratories (APC, IRAP and LAL) involved in the international JEM-EUSO consortium. The instrument was built by various institutes of the JEM-EUSO collaboration. The first balloon flights was performed by the balloon division of the French Space Agency, CNES, on 24 August 2014.



Figure 3.1: A pictorial view of the EUSO-Balloon mission.

The main objective of the EUSO-Balloon mission is to perform a full scale end-to-end test of all the key technologies and instrumentation of JEM-EUSO detectors and to prove the global detection chain. It aims to measure the atmospheric and terrestrial Ultra-Violet (UV, 300-400 nm) background components, in different observational modes, testing and adjusting trigger and switching algorithms and the acquisition capability of the Infra-Red (IR) camera (Figure 3.1). The EUSO-Balloon mission and instrument will be described in details in this chapter.

3.1 Objectives of the balloon flights

EUSO-Balloon will serve as a test-bench for the JEM-EUSO mission as well as any future mission dedicated to the observation of Extensive Air Showers (EAS) from space. Through a series of stratospheric balloon flights different level of objectives can be attained.

As a first step, EUSO-BALLOON is an in situ technology demonstrator, in fact, it is a full scale end-to-end test of all the key technologies and instrumentation of JEM-EUSO. Crucial issues that will benefit from the balloon flights include the High Voltages (HV) power supplies, the HV switches (HV relays commuting the HV in case a bright atmospheric event comes into the field of view and on a pixel), the Front-End Electronics (including the ASICs and FPGA), the on-board hardware and software algorithms involved in the triggering and recognition of cosmic-ray initiated air showers.

The second level objective is the study of the UV background. Although the physics and the detection technique of EAS through ultraviolet light emission is well established and widely used in ground based detectors, their observation from space has never been performed. Since JEM-EUSO uses the Earth's atmosphere to observe UV fluorescence tracks and Cherenkov reflections from EAS, the observations will be sensitive to the variation of the background sources in the UV range. Whereas a number of background measurements have been performed by previous missions, even from space, no focusing instruments have been employed so far and, most importantly, spatial resolutions were extremely low, i.e. the pixel size was much larger. Important localized background signals could have been washed out by the integration over a large surface and, likewise, possible temporal variations on small scales were not observable, and thus went unconstrained. Measuring a representative background for JEM-EUSO has been the principal driver for determining the pixel size, and hence the global Field of View of EUSO-Balloon. The EUSO Simulation and Analysis Framework (ESAF) has been adapted to simulate the response of the instrument. The configuration used for JEM-EUSO has been modified, scaling for the altitude of the instrument, changing the surface parametrization, introducing the new optical system and field of view.

Observing EAS from space will confirm the feasibility of the technique and provide valuable data for JEM-EUSO and all future space-borne Extreme Energy Cosmic Ray (EECR) experiments. The second level objectives are thus:

- experimental confirmation of the effective background below 40 km observed with a pixel size on ground representative for JEM-EUSO (175 m x 175 m in a 6° FoV);
- acquisition of UV signal and background in a format similar to the one of JEM-EUSO;
- testing of observational modes and switching algorithms;
- testing/optimizing trigger algorithms with real observations, i.e. different ground-covers and time-variable background;
- testing of the acquisition capability of the Infra-Red camera.

Lastly, EUSO-Balloon can be seen as a pioneering mission for JEM-EUSO. A “bonus” objective for EUSO-BALLOON is the actual detection of one or several EAS by looking downward from the edge of space. Since detecting these obviously rare events is unlikely during a first short balloon flight (threshold $\sim 10^{18}$ eV), Xenon-flashes and LASER-induced events will provide a proof of principle and a way to calibrate threshold and sensitivity.

The basic principle of these test is to fly an helicopter equipped with two types of calibrated pulsed UV light sources. If the helicopter flies in field of view and fire a flash lamp, the light travels directly from lamp to detector and it is possible to make point test. Whereas, flying the helicopter outside field of view and shooting a UV pulsed laser across field of view, the light scatters out of the beam to the detector. In such a way it is possible to make track test, considering that a 5 mJ Laser simulates the light emission of a cosmic ray of about 100 eV.

The first detection of a cosmic ray event will be guaranteed if EUSO-Balloon could accumulate several nights of flight. According to the estimation, EUSO-Balloon can get 2-3 events/night at $E > 2.1 \times 10^{18}$ eV, where the threshold energy arising from the background value measured by Yoshiya et al.. However if, as an example, the background is two times higher, the energy threshold of the detector is also two times higher and the event rate will be less than one event per night.

3.2 Description of the instrument

The telescope is composed of a self-contained, watertight instrument booth containing Photo Detector Module (PDM), electronics, telemetry and an optics module serving as optical bench for the lenses (see Figure 5.10). PWP

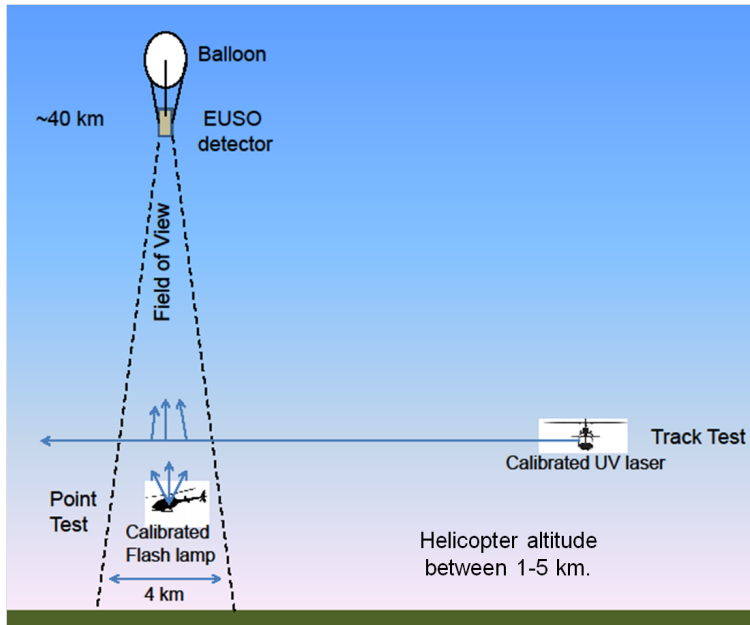


Figure 3.2: The basic principle of the “in flight” calibration with light sources on board a helicopter.

provides an average power of 225 W to the instruments and enough transient current generated at instrument booting. The structure of both the instrument booth and the optics module is made of 10 mm “Fibrelam” aerospace panels. Fibrelam panels are manufactured from honeycomb that is bonded between composite facing skins; they are light-weight, structurally sound and exceptionally stiff. The total weight of structure, instrument, dedicated electronics, telemetry systems and batteries is around 250 kg.

Integrating one of the Fresnel lenses as a port-hole window directly into the telescope structure will make the electronics compartment (with its crucial payload elements such as the PDM) entirely watertight without moving parts to permit offshore recovery. The instrument, in fact, has been laid out from the beginning for a recovery in water (even if the first flight was performed over land, because in Canada there are a lot of lakes during the warm seasons).

The instrument has been designed to face all the environmental constraints due to high altitude, such as the low pressure (3 mbar), but also to the wide thermal range: $-30^{\circ} \div 50^{\circ}$. To cope with the thermal problems, the electronics is mounted inside the instrument booth on a radiator plane, which has been designed to ease electronics cooling in a low pressure environment transferring the heat to the outer part of the gondola. In Figure 3.4 is showed a schematics of the the positioning of the various subsystems inside the instrument booth.

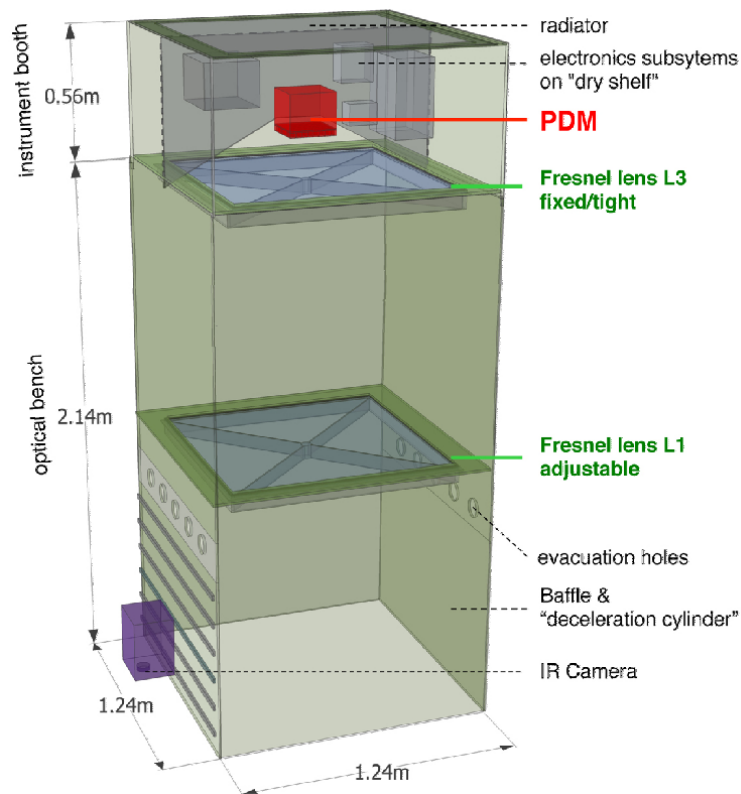


Figure 3.3: An overview of the EUSO-Balloon instrument. The PDM is a copy of the current JEM-EUSO design. The PDM and electronics are located on a dry shelf behind the third Fresnel lens. This metal shelf also acts as a radiator towards the top of the gondola to maintain the internal temperature of the instrument. The optics are a system of two Fresnel lenses, adapted from the JEM-EUSO design.

During the first flight (nadir pointing), the spin rate was determined by the natural azimuthal oscillations of the flight train. For later flights, the inclination of the pointing axis will be controlled (between 0° and 30° wht respect to the nadir and an azimuth motor will provide the possibility to perform revolutions with a spin rate of up to 3 rpm. Performing azimuthal revolutions will simulate a ground speed comparable to the $\sim 7 \text{ km s}^{-1}$ of the International Space Station (see Figure 3.5).

The instrument monitors a $12^\circ \times 12^\circ$ wide Field of View (FoV) in a wavelength range between 290 and 430 nm, at a rate of 400000 frames/s. The working bandwidth of the instrument, 290-430 nm, is determined by the spectral distribution of the fluorescence lines of Nitrogen in atmosphere. The FoV will be resolved into 2304 pixels, its dize is determined by a trade-off between using a JEM-EUSO like prototype and manufacturing constrains. The performances of EUSO-Balloon were maximized keeping parameters as

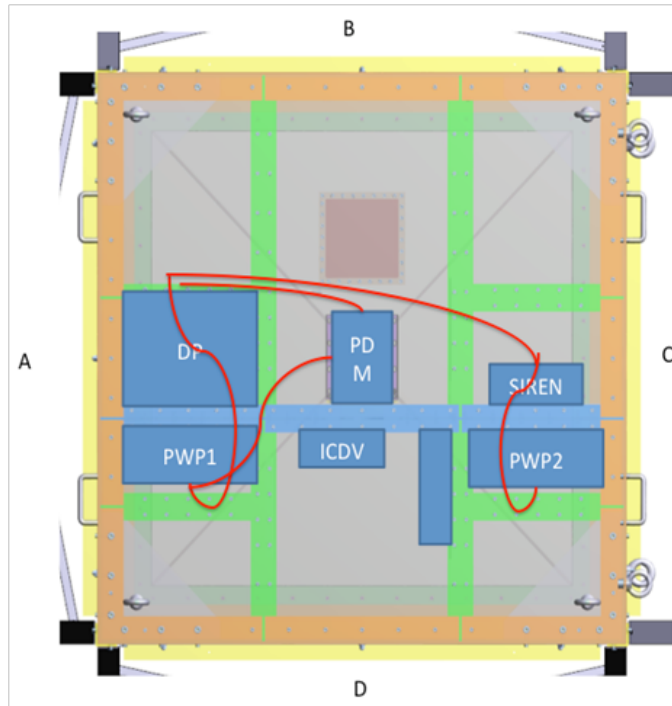


Figure 3.4: Top view of the full instrument showing the positioning of the various subsystems inside the instrument booth.

close as possible to JEM-EUSO, as is shown in table 3.1. The pixel size in the field of view is $0.25^\circ \times 0.25^\circ$, corresponding to $175 \text{ m} \times 175 \text{ m}$ on the ground for a float level of 40 km. The pixel size is mainly determined by the combination of the field of view and the focal surface pixel size. This is in turn determined (see next paragraphs) by the use of the PDM prototype designed for the JEM-EUSO mission.

In order to monitor the actual cloud coverage, a co-aligned IR camera observes the FoV of the main instrument. The IR-camera device studies the atmospheric properties, such as clouds coverage and top height, light scattering in the atmosphere, etc..

3.3 The working principle

The prototype instrument operates as follows: the UV light entering a two-lens Fresnel optics made from two PMMA square flat-type lenses is imaged on the PDM, an array of nine 8×8 pixels Multi Anode PhotoMultiplier Tubes (MAPMTs). The signal from the MAPMTs is processed by the Front-End Electronics (based on 36 SPACIROC ASICs) and preliminary processed in the so-called PDM board, which stores the data in round buffer and

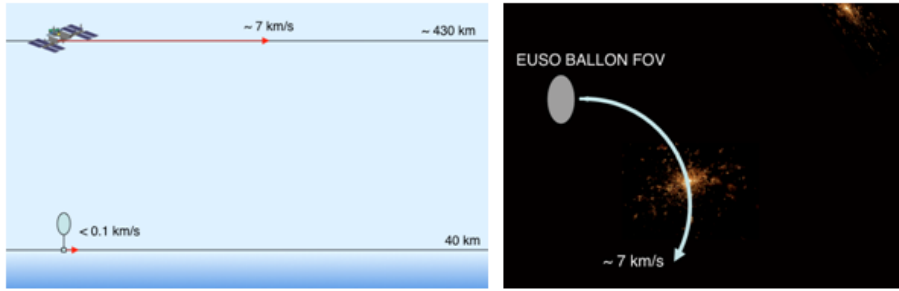


Figure 3.5: During later flights, the inclination of the pointing axis with respect to the nadir and azimuthal revolutions will simulate a ground speed comparable to the $\sim 7 \text{ km s}^{-1}$ of the ISS.

Table 3.1: Comparison of the principle characteristics between JEM-EUSO and EUSO-BALLOON. The field of view of EUSO-BALLOON, and hence its pixel size, has been dimensioned to measure a background level comparable to the one expected for JEM-EUSO.

	JEM-EUSO	EUSO-Balloon
Number of PDMs	14	31
Flight Altitude [km]	420	40
Diameter of Optics [m]	2.5	1
Field of View / PDM	3.8°	12°
PDM@ground [km]	28.2	8.4
Field of View / pixel	0.08°	0.25°
Pixel@ground [km]	0.580	0.175
Signal w/r JEM-EUSO	1	17.6
BG w/r JEM-EUSO	1	0.9-1.8
S/\sqrt{N} w/r to JEM-EUSO	1	20-10
Threshold Energy [eV]	3×10^{19}	$1.5 \div 3 \times 10^{18}$

performs the first-level trigger. Data are then transferred to the Digital Processor (DP) component where the second level trigger is applied by the Cluster Control Board (CCB) and data are prepared by CPU to be sent to telemetry. The DP performs data management, data storage, as well as instrument control and commanding. A block diagram of the functional architecture of the instrument is shown on Figure 3.6.

Analysing the image of the event track, the direction of the primary particle can be determined with triangulation techniques. The measurement of the light intensity in the pixels provides the energy of the incident cosmic ray. A schematic of the technique is shown in Fig. 3.7.

The UV light collected by the optical system is detected by the MAPMTs of the PDM. The PDM is mounted on a translation stage inside the telescope

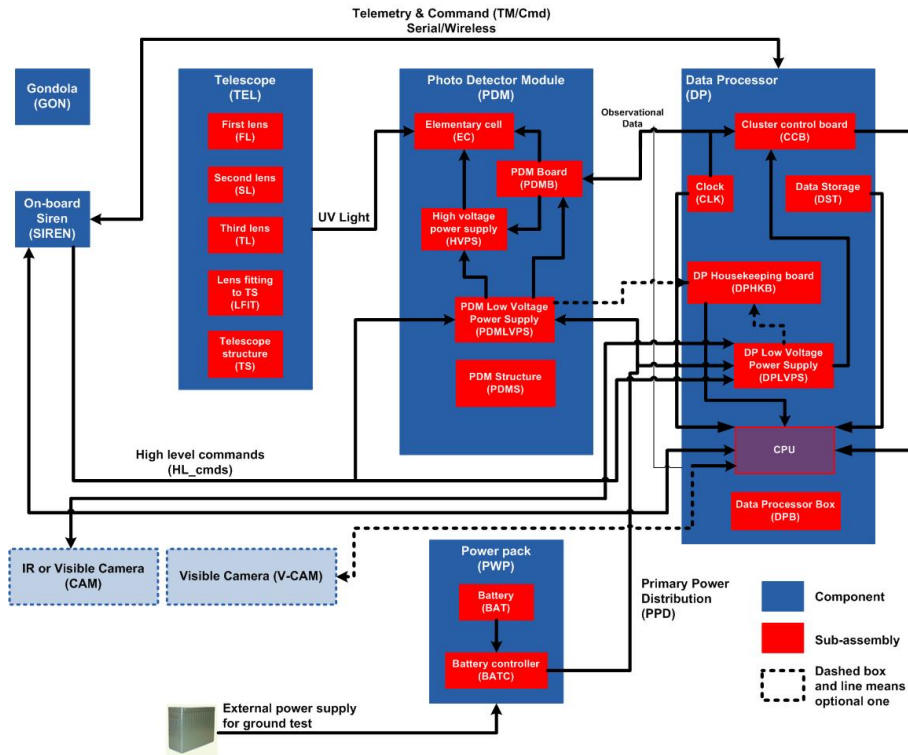


Figure 3.6: Architecture of the EUSO-BALLOON instrument functional diagram.

to adjust its position along the z-axis (perpendicular to the focal plane). Besides monitoring the UV background, the PDM can detect candidate shower events by the first trigger implemented in the PDM-board. The main operational mode, for low photon number signals, is the single photo-electron mode, also called “single photon counting”. In this case, the gain of the photo-detector is about 10^6 . The instrument however shall also operate in strong light mode and therefore the expected dynamic scale will be $1-10^6$. In case of strong light signal, the gain is automatically reduced and the acquisition mode switches to charge integration. Data acquired by the PDM are transferred via the PDM-board to the DP. The block diagram of the instrument summarizing the subsystems, and the main sub-assembly items is shown in Figure 3.8. The development of all components and sub-assemblies is based on similar JEM-EUSO components and sub-assemblies.

The basic data processing chain of JEM-EUSO, as shown in Fig. 3.8, is implemented in the EUSO-Balloon mission. Data from CCB are transferred to CPU, which controls the instrument and interfaces telemetry. The CPU manages the disks for on-board storage and the collection of the house-keepings from a dedicated Housekeeping sub-assembly. The power supply completes the DP component.

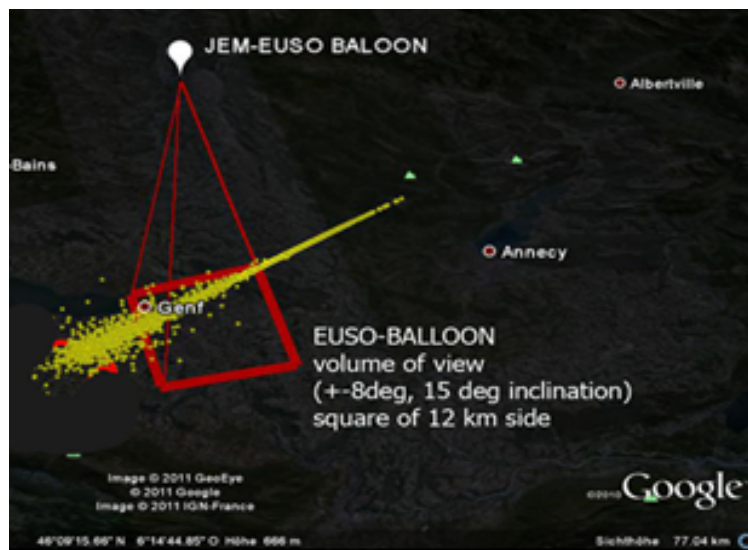


Figure 3.7: A 3-D view of the development of an EAS in the field of view of the EUSO-Balloon instrument located at 40 km of altitude is an example of phenomenon that could be observed.

The system is completed by the Ground Segment Equipment (GSE), which addresses the question of issuing external commands (TC) and receiving telemetry data (TM) from the instrument both during Assembly, Integration and Tests (AIT) operations at ground and during the flight. The control of the instrument is done via two entries points:

- serial line inside HK;
- the Ethernet line inside the DP-CPU.

During flight (Figure 3.9), the connection to the instrument (HK and DP-CPU) is done from ground via the CNES Siren module which is inserted inside the instrument. The Siren module transfers the TM/TC to/from the CNES NOSYCA. During most AIT operations (Figure 3.10), the CNES Siren module is replaced by a computer called the GSE server. The TM/TC are sent to/from the computer running the dedicated GSE server, actually a laptop having its serial line connected to HK and a connection with CPU through Ethernet link. The team can send commands to the instrument and retrieve the data results through GSE client interfaces running on their own computer connected to the LAN. During the balloon flight, the TM/TC is centralized on a single computer connected to the LAN, around which the full team on shift gathers to operate the instrument and monitor the telemetry data.

The Power Pack (PWP), which provides the necessary power to the instrument, is another component. PWP provides the primary power in 12

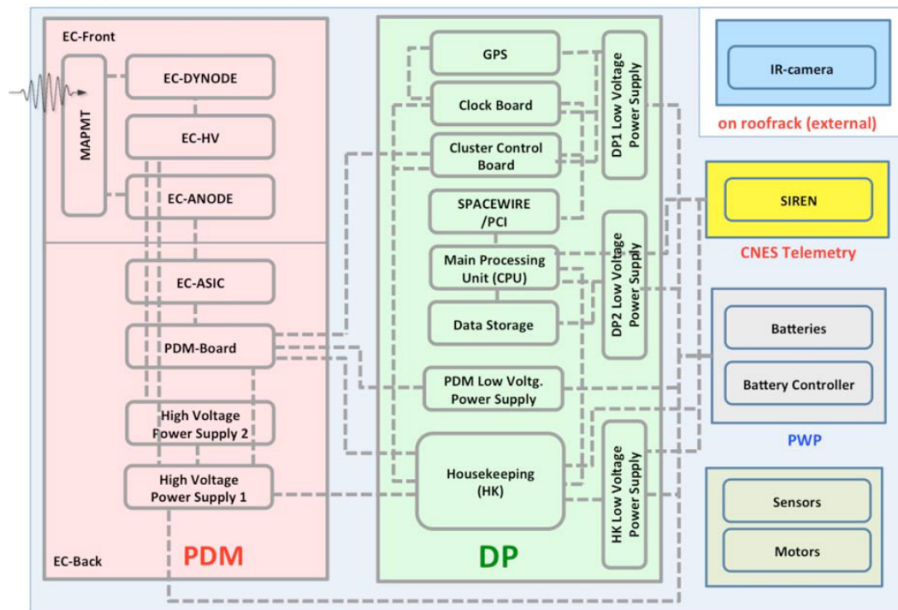


Figure 3.8: Functional Block Diagram of the EUSO-BALLOON instrument.

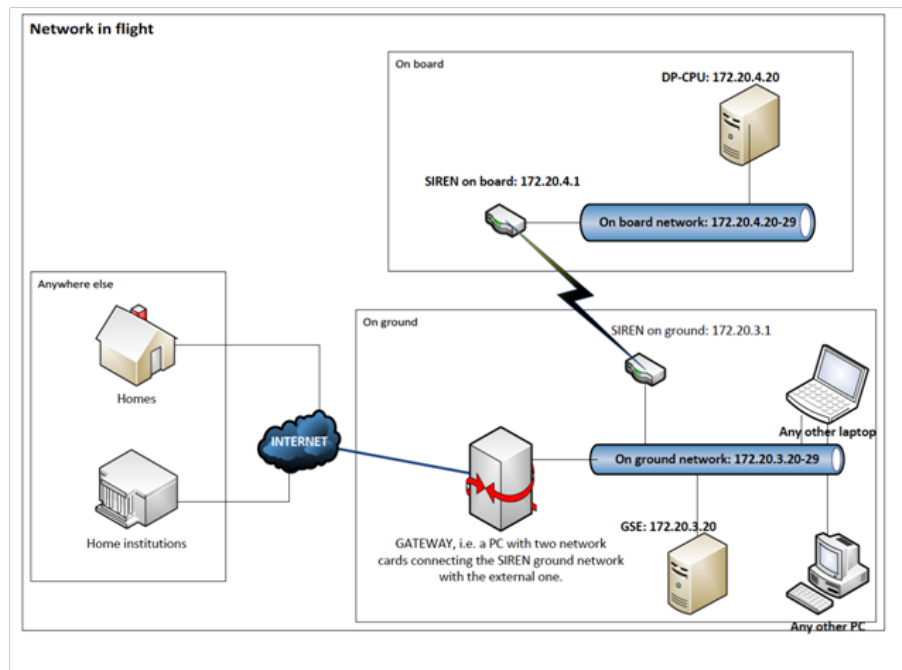


Figure 3.9: Ground Segment Equipment during the final AIT phase with SIREN or during flight.

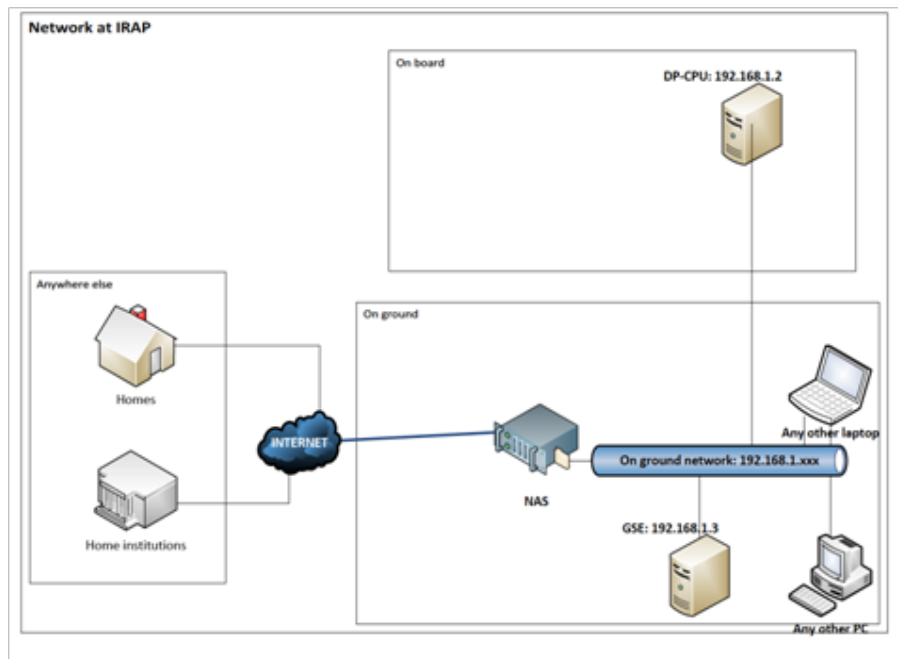


Figure 3.10: Ground Segment Equipment configuration during the final AIT phase without SIREN.

hours minimum, and 24 hours maximum level flight and rising operation.

The three main components of the instrument, the Optical System, the PDM and the DP will be described more in details in the next sections.

3.3.1 Optical system

The optical system focuses the incoming UV photon toward a pixel of the detector on the optical focal surface. The mechanical system of the instrument provides the frame in which the lenses are mounted. The FoV of the optics is $12^\circ \times 12^\circ$. A one meter long baffle defines an Entrance Pupil Diameter, the aperture of the optical system is $1\text{ m} \times 1\text{ m}$. The distance between the front surface of the front lens and the focal surface is 1620.7 mm. Each lens has a 1 m^2 square surface, a thickness of 8 mm and a weigh of 9.6 kg. Both lenses are Fresnel flat-types lenses and are made of PMMA.000. A four-armed “spider” supports every lens and minimizes deformation under its own weight. The lens is supported/aligned by the spider and a central plug. A seal makes the lens assembly watertight.

3.3.2 Photo Detector Module

The PDM (Fig.3.11) is the core element to detect the UV light coming from the optics. It is composed of 36 MAPMTs containing 64 anodes each and

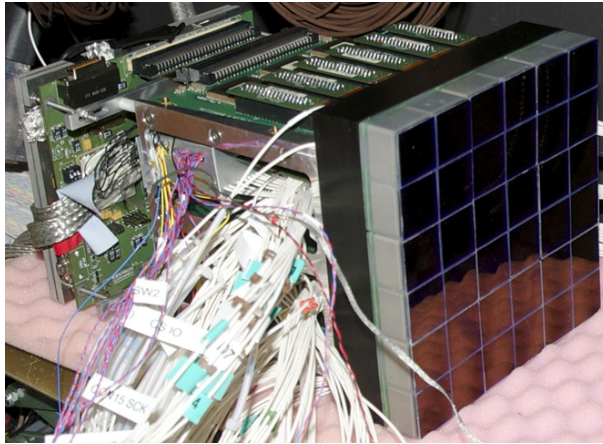


Figure 3.11: The whole PDM of the EUSO-Balloon instrument.

their associated electronic chain [?].

Every MAPMT senses the UV photons arriving through the lenses, it captures single photons, converts them in its photocathode into photoelectrons and induces pulses from the charges on its anodes and dynode output. On the mechanical structure the MAPMTs are grouped in 9 Elementary Cells (EC) which supply the voltages needed for each of them and collect signals from their anodes. These signals are transmitted to the SPACIROC ASIC for processing. The output signals of all the ASICs are delivered to the PDM board.

The PDM is equipped with two High Voltage Power Supply (HVPS), based on a Cockroft-Walton design, providing the necessary voltages to MAPMT dynodes. To cope with strong light signals (the dynamic scale of the signal ranges from 1 to 10^6), the High Voltages Power Supply are provided with switches that can modify the voltage between the cathode and the first dynode reducing the number of photo-electrons reaching the cathodes of the MAPMTs. In case of bright light, the gain will be such that no damage happens to the MAPMTs and that this strong light can be measured. A block diagram of the PDM is shown in Figure 3.12.

The MAPMTs are manufactured by Hamamatsu and has been developed specifically for the JEM-EUSO mission. The model number is the R11265-M64. The size of the MAPMT is $26.2mm \times 26.2mm \times 17.4mm$ and it has a maximum sensitive area of $23.04mm \times 23.04mm$, a quantum efficiency greater than 35% as well as a cross talk of about 1%. Their sensitivity is as low as a few tenths of photon and their dynamic range can extend up to few thousands photons per μs when working at their nominal high gain of 10^6 . An optical filter “SCHOTT BG3”, which transmits the UV photon and absorbs the visible light, is glued on each MAPMT. The transmittance of the BG3 filter is taken at 66% of the maximum corresponding to a band-

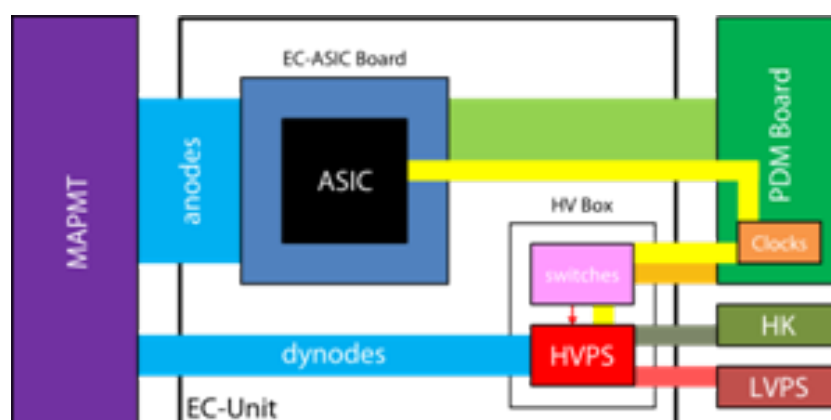


Figure 3.12: A block diagram of the main PDM components is shown. The PDM board receives the clock from the CCB (not shown here) and distributes it to the PDM electronics. All sub-assembly items are described in the text.

width of 290-430 nm. For the severe conditions of pressure (3 mbar at 40 km of altitude), the whole EC electronics are potted with resin to protect them against destructive sparking, induced possibly by the HV.

The analog signals coming from MAPMTs are collected by six ASIC boards fixed perpendicularly to the mechanical frame that houses the nine EC. As shown in the Figure 3.13, an ASIC board is composed of six (three on each side) SPACIROC ASICs packages, six 68-pin connectors toward the EC and one 120-pin connector toward the PDM board. Each of paired ASIC board read three halves of EC.

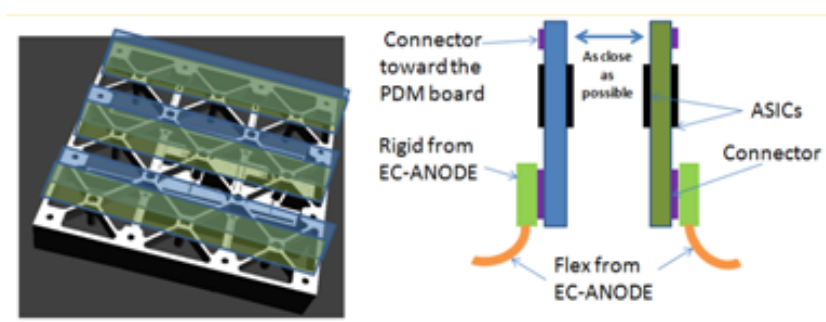


Figure 3.13: On the left a schematic view of the PDM mechanical structure with the 6 EC-ASIC boards mounted on it. On the right a side view of a pair of 2 ASIC boards.

The front-end SPACIROC ASIC must be able to deal with different types of anode signals. In fact, in the normal mode the ASIC detects the signal of the MAPMT produced by the very faint light of the background (about 1.5 MHz UV photons on each pixel) or the light from an EAS, which

ranges from the background level to 100 times it. The pulse from the PMT is 4 ns wide, with a rate of about 0.5 MHz for the background. Pulses are hence very well separated. The normal mode is called single photo-electron (SPE) mode. In case of strong illumination, pile-up occurs, and the SPE mode cannot be used. In this case, integrating circuits (KIs) integrate the charge delivered at each anode during each acquisition window, called Gate Time Unit (GTU = 2.5 μ s). The charge integration mode is meant to be used for the wide range of signals originated by the different types of event which could be observed by JEM-EUSO.

The SPACIROC ASIC is designed to read out MAPMT 64 anodes signals. The analog part of the ASIC has two main purposes: counting the number of SPEs reaching each pixel of the MAPMTs and measuring the intensity of photon flux by performing charge to time (Q-to-T) conversion. In addition, the SPACIROC ASIC digitizes the analog signal inputs during each GTU and sends the previously acquired data to the PDM board via dedicated digital serial connections. The ASIC has a 64 channels preamplifier with independent gain (8-bit) adjustment in order to correct for the non-uniformity of the 64 MAPMT anodes. The SPACIROC ASIC has been designed by Omega group at LAL in AMS 0.35 μ m SiGe technology [?] and has to meet the requirements for 5 years operation of JEM-EUSO as following:

- Low power consumption: < 1 mW/ch (for 1 ASIC 74.88mW for one ASIC and 2.696 W for a PDM unit);
- 100% trigger efficiency in Photon Counting at 50 fC (\sim 1/3 PEs at a PMT gain of 10^6);
- dynamic range in charge measurement 1.5 to 150 PEs/GTU/pixel or a sensitivity of factor 100;
- linearity in Photon Counting: \geq 30 PEs/GTU;
- time resolution for 1 photo-electron pulse: *leq* 30 ns.

The PDM board handles all the nine EC units. It performs the 1st level trigger looking for pixels firing for several contiguous Gate Time Units(GTU) on the PDM. It manages the interfaces with the EC boards, CCB board as well as the HV system. From the EC boards, the data transmission runs at the rate of 400 kHz. To the CCB, the data transmission rate, via SPI (Serial Peripheral Interface) bus, is at a lower level, 7Hz. The PDM board receives both the system clock and the GTU clock, generated by CLK-Board, from the CCB and distributes it to the PDM electronics. This system will be described in the next section.

3.3.3 Data Processor

The DP system is the component of the electronics subsystem which includes most of the digital electronics of the instrument. It controls the front-end electronics, performs the 2nd level trigger filtering, tags events with arrival time and payload position, manages the data storage, measures live and dead time of the instrument, provides signals for time synchronization of the event, performs housekeeping monitor, handles the interfaces to the Tele-Commands and Telemetry (TC/TM) system.

The DP system of EUSO-Balloon operates at high altitude in unpressurised environment and this represents a technological challenge for heating dissipation. To cope with thermal problems, a passive cooling system that exchanges heat directly from the modules through the mechanics of the DP box to the gondola structure has been developed. The metal cooling plate of the DP box is mechanically connected to each subsystem and transfers the heat by conduction to the outside of the gondola. Moreover, every subsystem is provided with a temperature monitoring system.

The DP functionalities are obtained by connecting different specialized items, which form a complex system. The main sub-assembly items are:

- Control Cluster Board (CCB);
- CPU;
- Data storage;
- Clock Board;
- GPS receiver;
- Data Processor Power Supply (DP-LVPS);
- Housekeeping system.

A block diagram of the DP is shown in Figure 3.14.

The DP is hosted in a Eurocard 6U subrack with 3U dividers. Each sub-assembly, in turn, is hosted in a metallic frame-type plug-in units which accepts boards in eurocard format. The DP mass and power budgets are 15 Kg and 50 W respectively.

The CCB [?] has a direct connection to the PDM through a 40 MHz parallel bus. It processes and classifies the received data performing the 2nd level trigger. Moreover, CCB has to pass the clock signals from the CLK-Board to PDM and the configuration data from CPU to PDM. The event size is 324 kbyte plus headers/footers for each event, so full transmission is not possible, since it would require 0.96 Gbyte/second or 3.5 Tbyte/hour. The circuit is developed around a Xilinx Virtex-4 FX-60 with extended industrial temperature range on a eurocard board.

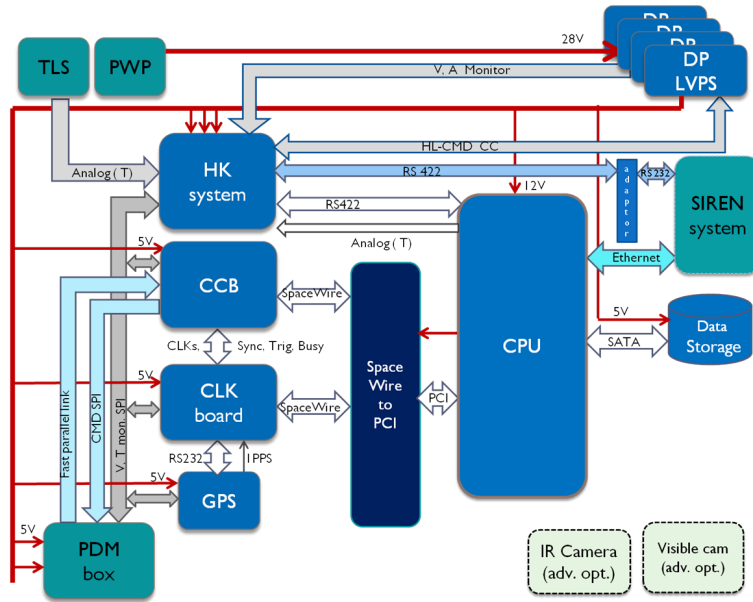


Figure 3.14: Functional block diagram of the Data Processor.

The CPU is the core of the DP and it is in charge of the following main functions:

- to manage the acquisition of science data from the instrument;
- to manage the mass memory storage in order to store science and telemetry data received from the instrument and the on board sensors and transducers;
- to manage communication with the SIREN system to transmit data to ground and receive tele-commands;
- to prepare and broadcast control commands needed to configure and operate the payload subsystem;
- to control the HK board and collect HK data;
- to switch ON/OFF (through the HK) all the DP sub-assemblies.

The CPU records large amounts of data produced by the FS electronics, via the CCB board, the GPS receiver, via the CLK-Board, as well as the HK system. The CPU collects all the data, for each triggered event, and records them into the storage system and, in case, transmits them to the SIREN system. The data storage operation is usually a bottleneck in a real time system and should be kept as fast as possible in order to keep the dead time of the apparatus as small as possible. For EUSO-Balloon the typical size of

an event is 330 kbyte which, at trigger frequency of few tens of Hz, imply a sustained transfer rate up to 150 Mbits/sec . A high-speed, high-capacity mass storage system is required to properly archive such a large amount of data. Moreover, a capacity of at least 512 GB was required in order to store all the data produced by the apparatus in a ten hours flight. The chosen mass storage is composed by an array of two Solid-State Drive operating in disks fault-tolerant mode RAID-1 (Redundant Array of Independent Disks). The selected Solid-State Drive devices are the 1 TB CZ Octane SATA II 2.5” Solid-State Drive drive with a SATA II interface.

For each trigger roughly 330 kB of data are transmitted via SpaceWire protocol [128] from CCB to the CPU. All the communications with CCB and CLK-Board is done via the SpaceWire interface. Ethernet ports are used for transmission and reception of commands to/from the SIREN system. The CPU controls the HK system and transmits/receives housekeeping data to/from it by using a serial protocol and through a RS422 serial port. The interface which transforms SpaceWire data packets in a data stream compatible with the port/expansion available on the CPU boards is a commercial off-the-shelf device, the “SpaceWire to PCI MK2” board manufactured by the Star Dundee Ltd. The CPU Motherboard is the iTX-i2705 model, manufactured by Arbor. It is based on Atom N270 1.6 GHz processor. The power consumption of the board is less than 12 W.

The CLK-Board [?] is the part of the data processor devoted to generate and distribute the system clock (40 MHz), the GTU clock (400 kHz, 98% duty cycle) and the synchronization signal to all the devices of the FS electronics and to provide time synchronization of the events. The board has an interface with a GPS receiver which allows to collect, for each event, information on the position of the instrument and the Coordinated Universal Time with a precision of few microseconds.

In addition, the CLK-Board has to measure live and dead times of the detector; to calculate these quantities the CLK-Board needs to know when the system is busy and cannot generate triggers that are disabled. For this reason, the CLK-Board receives the second level trigger information from the CCB and is in charge to generate system busy to disable trigger generation. It receives the 2nd level trigger signal and a end-of-transmission signal from the CCB and a release-busy signal from CPU. These signals drive the logic implemented on the board to measure the live time and dead time of the apparatus.

The CLK-Board receives commands from CPU and transmits data to the CPU by using the Space-Wire communication protocol. Finally, the CLK-Board is able to generate fake trigger signals in two ways: on a CPU command or by an external trigger signal coming from an external trigger source, such as TA trigger signal or a signal generator. The fake trigger signal coming from CLK-Board is then forwarded to the PDM, which acquires the MAPMT photons counting and sends back a first level trigger signal.

An FPGA Xilinx Virtex5 XC5VLX50T (Industrial grade) implements all the required functionalities of the Clock Board. The master clock is generated by a 40 MHz Temperature Compensated Crystal Oscillator capable of a frequency stability of ± 1 ppm in the temperature range of -40°C to 85°C . The GTU clock is obtained from the master clock. All the signals to the CCB boards through differential LVDS as output protocol and point-to-point connections. The CLK-Board has a direct connection with the GPS receiver through a serial port in order to collect data and deliver commands. The 1PPS (Pulse Per Second) signal generated by the GPS receiver is used in order to synchronize, at level of one GTU, the apparatus with the UTC time.

The GPS receiver provides location and time information of the payload during the flight. The precision required in determining the position of the payload during the mission is widely ensured by a civilian receiver operating in the L1 band (1575.42 MHz). The GPSR interfacing with Data Processor is performed through the CLK-Board, which associates the GPS relevant data to each acquired event. In order to properly interface with the CLK-Board the GPS receiver has a 1PPS output and RS232 data/command communication port. The main difficulty in the procurement of a GPS receiver for a balloon mission was the ITAR restrictions for all GPS receivers capable of functioning above 18 km altitude and 515 m s^{-1} . To respect these restrictions almost all the COTS GPSR stop operating at altitude greater than 18 km. The GPS receiver selected was the Oncore M12 manufactured by Motorola.

The DP-LVPS is responsible for distributing low voltage power to the components of the DP. Three boards comprise the LVPS-DP system. One board is dedicated solely to supply power to HK and is turned on through SIREN. Two boards supply the rest of DP: one supplies CCB, GPS and CLK-Board, while the last one supplies CPU and disks.

The HK performs ON/OFF and status monitoring of all the LVPS boards and, through them, of their associated subsystems, as well as monitoring of temperature, current and voltage, distribution of TC and reception of TM, and the generation of alarms in slow control mode, i.e. for tasks that do not require response on time scales below 1 second. Alarms signals generated by other subsystems to prevent any malfunctions are also handled by HK, which, under the control of the CPU, can turn ON/OFF or reset all the DP components. The HK works in two modes: cyclic and on-demand from the CPU or ground through SIREN.

The Housekeeping is implemented around an off-the-shelf micro-controller board (Arduino Mega 2560), combined with 5 custom-made protocol interface boards to pre-process the various signals. The Housekeeping system has also to monitor alarms and temperature coming from every subsystems to prevent any malfunction and, under the control of the CPU, can turn on and off or reset all the DP components.

Chapter 4

The timing and synchronization system of the JEM-EUSO pathfinders

This chapter will describe the first part of my thesis work, which consisted in the design of the timing and synchronization system for the JEM-EUSO pathfinders.

Before moving to the description of the timing and synchronization board it is necessary to recall the main function and components of the data acquisition chain in which the system operates.

The Data Processor (DP) system is the component of the electronics subsystem which includes most of the digital electronics of the instrument. It controls the front-end electronics, performs the 2nd level trigger filtering, tags events with arrival time and payload position, manages the data storage, measures live and dead time of the instrument, provides signals for time synchronization of the event, performs housekeeping monitor, handles the interfaces to the Tele-Commands and Telemetry system. The DP functionalities are obtained by connecting different specialized items, which form a complex system. Apart from the timing and synchronization system, the main sub-assembly items of DP are:

- Control Cluster Board (CCB);
- CPU;
- Data storage;
- Data Processor Power Supply (DP-LVPS);
- Housekeeping system.

A functional block diagram of the whole EUSO-Balloon instrument, with all the connections of the DP shown, is reported in Figure 4.1.

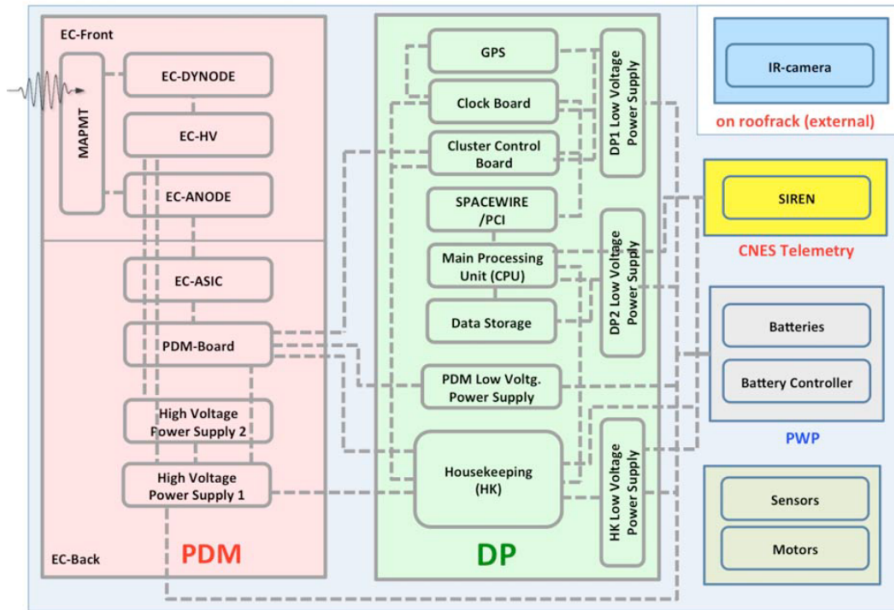


Figure 4.1: Functional block diagram of the EUSO-Balloon instrument.

The DP acquires and stores data from the Photo Detector Module (PDM) through a dedicated Field Programmable Gate Arrays (FPGA), called PDM-Board. This board handles the front end electronics, namely the Elementary Cell (EC) units, to perform the data acquisition. It manages the interfaces with the EC boards, CCB as well as the HV system. From the EC boards, the data transmission runs at the rate of 400 kHz. The PDM board receives both the system clock and the GTU clock, generated by CLK-Board, from the CCB and distributes it to the front end electronics.

As mentioned in section 3.3.3, the timing and synchronization system is composed by an FPGA, i.e. the CLK-Board, and a GPS receiver. The CLK-Board, as well as generating and distributing the system clock and the clock GTU, has to create a time synchronization between the various electronic devices and act as interface with the GPS system, store the trigger signals coming from CCB and measure live time and dead time. The GPS receiver provides location and time information of the payload during the flight, it allows to tag every event with an absolute time stamp.

The core of the timing and synchronization system is the CLK-Board and my work was mainly devoted to the design of the firmware and the hardware of this item. At the same time, a description of the system cannot disregard the GPS receiver. In order to make a clear and continuous description of the CLK-Board, I will introduce first the GPS receiver and its characteristic, together with the main features of the board that hosts the receiver.

To clarify the development of the CLK-Board it is necessary to intro-

duce first the philosophy of the FPGA programming and the design techniques and device used for the development of the CLK-Board of JEM-EUSO pathfinders.

After this brief introduction, I will move to the actual description of the CLK-Board. All the implementation of the different tasks of this board will be presented according to the scheme used for the design in order to clarify the choices made and the operation of various module. The design can not be closed down before a simulation of the behaviour of the system; given the large number of subsystems implemented, every component has been simulated and tested individually and then inserted into the complete project. In the course of the description, I will present some simulations of the different subsystems to clarify and verify their operation.

4.1 The GPS receivers

The GPS receiver allows to collect, for each event, information on the position of the instrument and the UTC time with a precision of few microseconds. The precision required in determining the position of the payload during the mission is widely ensured by a civilian receiver operating in the L1 band (1575.42 MHz).

The GPS receiver interfacing with Data Processor is performed through the CLK-Board, which associates the GPS relevant data to each acquired event. In order to properly interface with the CLK-Board, the GPS receiver was chosen with a 1PPS (Pulse Per Second) output and RS232 data/command communication port.

For EUSO-Balloon the GPS receivers shall be capable of functioning at 40 km of altitude. The main difficulty in the procurement of a GPS receiver for the balloon mission are the ITAR restrictions for all GPS receivers capable of functioning above 18 km altitude and 515 m s^{-1} . To respect these restrictions almost all the COTS GPS receivers stop operating at altitude greater than 18 km.

The GPS receiver chosen for TA-EUSO, the SiRFstarIII 20-channel GPS receiver, provided by Inventek and based on low power devices, was tested at CNES with a GPS Constellation simulator. Differently from what stated by the manufacturer, it stops working properly at altitudes greater than 18 km. The GPS receiver actually used for EUSO-Balloon is the Oncore M12 manufactured by Motorola. This is one of the major differences between the Data Processor of EUSO-Balloon and TA-EUSO. Both GPS receivers chosen have a power consumption below 1.5 W and have been tested and integrated in PCB designed to provide them all the connections to others DP components.

The M12+ Oncore receiver provides position, velocity, time, and satellite tracking status information via a serial port. The receiver is capable of

tracking twelve satellites simultaneously. The M12+ receivers receive electrical power and receive/transmit I/O signals through a 10-pin power/data connector mounted on the receiver. To cope with ITAR restrictions, there is a limit in velocity (515 m s^{-1}) above 18 km altitude, the working temperature range is -40°C - 85°C . The receiver is capable to transmit data in two format: the standard NMEA at a baudrate of 4800 baud and a proprietary format at 9600 baud.

The native binary data messages used by M12+ Oncore receiver consist of a variable number of binary characters (hex bytes). All binary messages begin with the hex characters '0x40 0x40', which most users convert to the ASCII equivalents "@@". The first two characters after the "@@" header comprise the message ID and identify the particular structure and format of the remaining data. This message data can vary from one byte to over 150 bytes, depending on the message being transmitted or received. Immediately following the message data is a single byte checksum which is the Exclusive-Or (XOR) of all bytes after the "@@" and before the checksum. The message is terminated with the Carriage Return/Line Feed pair: "0x0D 0x0A". The message ID is made by two ASCII characters which identify the message type and imply the correct message length and format.

The receiver can output position, velocity, and time data on the serial port at a maximum rate of once each second. For every message, it is possible to select a polling time, in order to receive a certain set of information at a fixed rate. I choose to receive three messages every second:

- 12 channel position/status/data message (154 bytes): this message provides position and channel related data such as date, time, speed and number of satellites tracked
- ASCII Position Message (96 bytes): the ASCII position output message contains position, time and receiver status information simil. The ASCII message may be a more convenient interface for certain applications where the ASCII output of NMEA is desired, but operation at 4800 baud is not desirable. The units and style of the data is similar to NMEA output.
- self-test message (10 bytes): the M12 Oncore is able to perform an extensive self-test to check the antenna connection, the real time clock communication and time and other features. The output of the self-test command is a 24-bit field, where each bit of the field represents Pass/Fail condition for each parameter tested. Once the self-test is complete, the acquisition process starts all over as if the receiver were first powered on. The date, time, position, almanac and ephemeris information is all retained.

The M12+ receiver timing is established relative to an internal, asynchronous, 1 kHz clock derived from the local oscillator. The receiver counts

the 1 kHz clock cycles, and uses each successive 1000 clock cycles to define the time when the measurement epoch is to take place. The measurement epoch is the point at which the receiver captures the measurements for computing position, velocity, and time. When the M12+ processor computes receiver local time, this time corresponds to the time of the last receiver measurement epoch. The Oncore process precisely determines this time to an accuracy of approximately 20 to 300 ns depending on satellite geometry. The computed time is relative to UTC or GPS time depending on the time type as specified by the user using the Time Mode command (“@@Aw”). The Oncore system timing is designed to slip time when necessary in discrete one millisecond intervals so that the receiver local time corresponds closely to the measurement epoch offset. The Oncore observes the error between actual receiver local time and the desired measurement epoch offset and then slips the appropriate integer milliseconds to place the measurement epoch to the correct integer millisecond. When a time skew occurs (such as after initial acquisition or to keep time within limits due to local oscillator drift), the receiver lengthens or shortens the next processing period in discrete one millisecond steps. The rising edge of the 1PPS signal is the time reference. The falling edge will occur approximately 200 ms (± 1 ms) after the rising edge. The falling edge should not be used for accurate time keeping.

Generally, the first data byte in the first message will be output between 0 to 50 ms after a measurement epoch. For the Position/Status/Data Message, the time output in the message reflects the best estimate of the most recent measurement epoch. A simple timing diagram of the GPS output signals is shown in Figure 4.2.

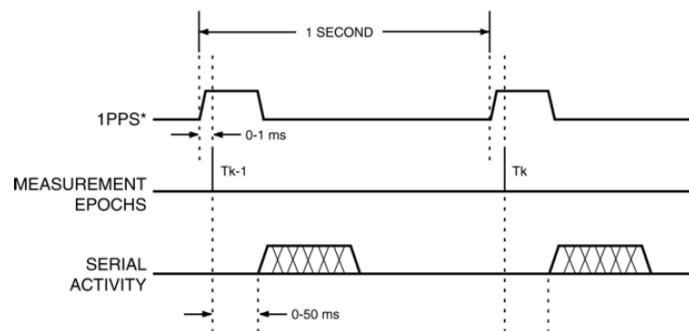


Figure 4.2: The timing diagram of the GPS output signals.

The receiver can output position, velocity, and time data on the serial port at a maximum rate of once each second. The start of the output data is timed to closely correspond with the receiver measurement epoch. The measurement epoch is the point in time at which the receiver makes satellite range measurements for the purpose of computing position. The first byte of serial data in the position message is output between 0 and 50ms after

the most recent receiver measurement epoch.

In figure 4.4 is shown the flight model of the GPS receiver board manufactured and tested with connectors mounted and soldered, while in figure ?? is reported the electrical scheme of the board.

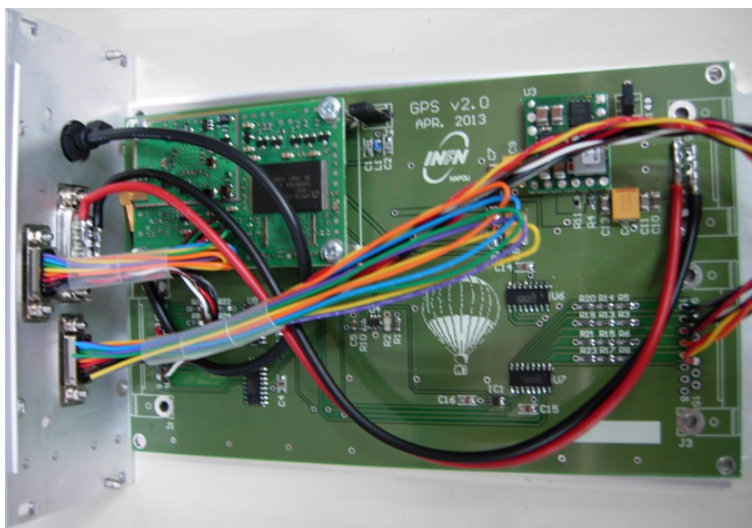


Figure 4.3: Flight model of the GPS receiver board manufactured and tested with connectors mounted and soldered.

The GPS receiver used in TA-EUSO is the Inventek—. This receiver can use only NMEA protocol at 4800 baud,

The GPS receiver has two interfaces with the DP:

- three couples of differential LVDS point to point connections with the CLK-Board;
- five couples of differential LVDS lines with the HK.

The lines exchanged with the CLK-Board are:

- data output;
- command input;
- 1PPS signal.

More details about these lines will be given in section 4.1.

Concerning the interface with the HK, it is based on two COTS device, one for monitoring the temperatures and the other for voltage. The HK uses a SPI protocol.....



Figure 4.4: Electrical scheme of the GPS receiver board.

4.2 Introduction to Field Programmable Gate Arrays

An FPGA is a type of integrated circuit (IC) that can be programmed for different algorithms after fabrication. FPGAs allow the designer to create a custom circuit implementation of an algorithm using an off-the-shelf component composed of basic programmable logic elements. Modern FPGA devices consist of up to two million logic cells that can be configured to implement a variety of software algorithms. An algorithm implemented in an FPGA benefits from the inherent parallel nature of a custom circuit. In addition, FPGAs provide significant cost advantages in comparison to ICs development effort and offer the same level of performance in most cases. Another advantage of the FPGA when compared to the IC is its ability to be dynamically reconfigured. In fact, FPGAs can have a “volatile” or “non-volatile” configuration, according to whether or not the configuration is lost each time the device is switched off. There are also devices which can be programmed only once.

FPGAs are based on a matrix of on-field programmable logic resources. Logic resources are homogeneously distributed in blocks on the whole surface of the chip. Blocks can work in combinational (executing boolean functions) or sequential mode (executing boolean functions whose result may depend on the history of the inputs). In order to connect the blocks among them and with the Input/Output (IO) logic there are dedicated interconnection

resources, which are also programmable. Interconnection resources are a grid of conductive segments, which can be in contact with each other and with the logic in such a way to make the connect the blocks. The basic structure of an FPGA is composed of the following elements:

- Look-up table (LUT): performs logic operations;
- Flip-Flop (FF): register elements which stores the result of the LUT;
- wires: interconnection resources;
- IO pads: physically available ports that get data in and out of the FPGA.

Although this structure is sufficient for the implementation of any algorithm, the efficiency of the resulting implementation is limited in terms of computational throughput, required resources, and achievable clock frequency.

Contemporary FPGA architectures incorporate the basic elements along with additional computational and data storage blocks that increase the computational density and efficiency of the device. These additional elements, which are discussed in the following sections, are:

- embedded memories for distributed data storage (BlockRAMs);
- Phase-locked loops (PLLs) for driving the FPGA fabric at different clock rates;
- high-speed serial transceivers;
- off-chip memory controllers;
- multiply-accumulate blocks.

The combination of these elements provides the FPGA with the flexibility to implement any software algorithm running on a processor and results in the contemporary FPGA architecture shown in Figure 4.5.

The LUT is the basic building block of an FPGA and is capable of implementing any logic function of N Boolean variables. Essentially, this element is a truth table in which different combinations of the inputs implement different functions to yield output values. The hardware implementation of a LUT can be thought of as a collection of memory cells connected to a set of multiplexers. The inputs to the LUT act as selector bits on the multiplexer to select the result at a given point in time. A LUT can be used as both a function compute engine and a data storage element. The contents of the truth table of the small memory of a LUT are written during device configuration. Due to the flexibility of the LUT structure, these blocks can be used as small memories and are commonly referred to as distributed memories. This is the fastest kind of memory available on the FPGA device, because it

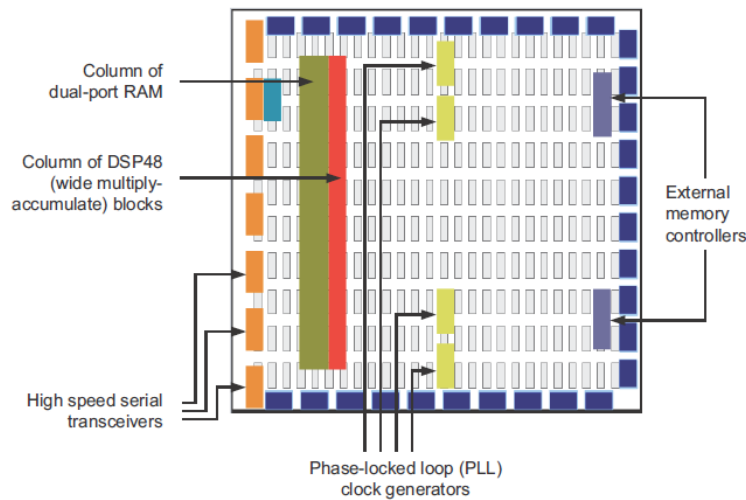


Figure 4.5: Contemporary FPGA Architecture. In this picture is shown an example of a typical Xilinx FPGA.

can be instantiated in any part of the fabric that improves the performance of the implemented circuit.

The flip-flop is the basic storage unit within the FPGA fabric. This element is always paired with a LUT to assist in logic pipelining and data storage.

LUT and FF constitute the heart of the device, the so-called Configurable Logic Blocks (CLBs): programmable elements which can execute combinational and/or sequential operation. The designer may program CLBs and then connect them together in such a way to build the required logic.

The IO blocks permit interfacing the internal logic with external devices while the wires connect LUT, FF and IO pads.

BlockRAMs are configurable embedded memory elements which can be used as a support for the logic implemented with the CLBs: in fact, they allow to store information inside the device, without using the sequential resources of the CLBs. BlockRAMs can be configured as double-port or single-port random-access memory (RAM), read-only memory (ROM), shift registers or first in, first out (FIFO) memory circuit. The shift register is a chain of registers connected to each other. The purpose of this structure is to provide data reuse along a computational path, such as with a filter. By using a shift register to store the input data, a built-in data transport structure moves the data sample to the next multiplier in the chain on every clock cycle. A FIFO can be thought of as a queue with a single point of entry and a single point of exit. This kind of structure is typically used to transmit data between program loops or functions.

The specific task executed by an FPGA changes according the configuration of its logic elements, and this translates into a good versatility of the

device, which enables the user to emulate a big number of possible fixed-logic circuits. An FPGA includes an internal memory (the “configuration memory”), used for storing the programming code of all the logic elements (the bitstream). Usually, the FPGA configuration memory is volatile, therefore the bitstream is loaded into a non-volatile external memory (for instance a PROM, a flash memory or the hard-disk of a computer) and at the powerup the configuration is copied to the configuration memory. The bitstream defines also the content of each BlockRAM at the device power-up.

When compared with processor architectures, the structures that comprise the FPGA fabric enable a high degree of parallelism in application execution. The FPGA is an inherently parallel processing fabric capable of implementing any logical and arithmetic function that can run on a processor. The FPGA implementation instantiates independent sets of LUTs for each computation in the software algorithm. In addition to assigning unique LUT resources per computation, the FPGA differs from a processor in both memory architecture and the cost of memory accesses. Scheduling is the process of identifying the data and control dependencies between different operations to determine when each will execute. In traditional FPGA design, this is a manual process also referred to as parallelizing the software algorithm for a hardware implementation. High Level Sintetizer analyses dependencies between adjacent operations as well as across time. This allows the compiler to group operations to execute in the same clock cycle and to set up the hardware to allow the overlap of function calls.

4.3 FPGA design flow

Today digital designers mostly use high level Hardware Description Languages (HDL) to design digital systems. The most widely used HDLs are VHDL and Verilog. Both of them allow the user to design digital systems by writing a program that describes the behavior of the digital circuit. The program can then be used to both simulate the operation of the circuit and synthesize an actual implementation of the circuit in the FPGA.

The main difference between hardware and software design is that in hardware design all the input signals are processed in parallel, as they travel through a set of execution engines-each one a series of macrocells and interconnections-toward their destination output signals. Therefore, the statements of a hardware description language create structures, all of which are executed at the very same time.

Since the digital design implies an hardware implementation, the design specification stage includes the following activities:

- I/O specification;
- system timing requirements and timing constraints;

- memory requirements;
- verification methodology;
- selection of the FPGA family and device, including the speed grade: it is necessary to estimate the size of the design in order to meet the power and heat dissipation requirements; after the size of the logic is estimated and operating frequencies are specified, the approximate size and speed grade of the device can be selected.

Once the design is specified, it starts the actual hardware design process. Designing with FPGAs can be divided in three main steps: development and optimization of the logic according to the available resources, logic partitioning, allocation and interconnection of the resources and physical programming of the device.

The hardware compilation consists of two main distinct steps: synthesis, which is the process of converting a design representation from RTL code to a gate-level netlist, and place and route, which results in a bitstream, which can be loaded into the FPGA to cause that chip to execute a particular hardware design. The process the development software goes through to compile a design into a bitstream is depicted in more details in Figure 4.6 [115]:

1. The designer develops a logic circuit using a hardware description language or a schematic editor, optimizing the logic according to the available resources.
2. A logic synthesizer transforms the HDL into a gate-level netlist, which is device independent. The netlist is a description of the various logic gates in the design and how they are interconnected.
3. The implementation phase employs three different tools. A translator merges together one or more netlists along with any design constraints. Then a mapper combines gates in the netlist into groups that will fit efficiently into the LUTs of the FPGA. The gate groupings are sent to the place and route tool that assigns them to LUTs at various locations in the FPGA and then determines how to connect them together using the routing resources in the switching matrix and input and output pins.
4. A bitstream generator takes the output of the implementation phase, combines it with a other configuration settings, and outputs a binary bitstream. This bitstream is a binary data which contains the truth-tables that will be loaded into the RAM of every LUT and the connection settings for the wiring matrix that will connect them.
5. The downloader transfer the bitstream into a physical FPGA chip.

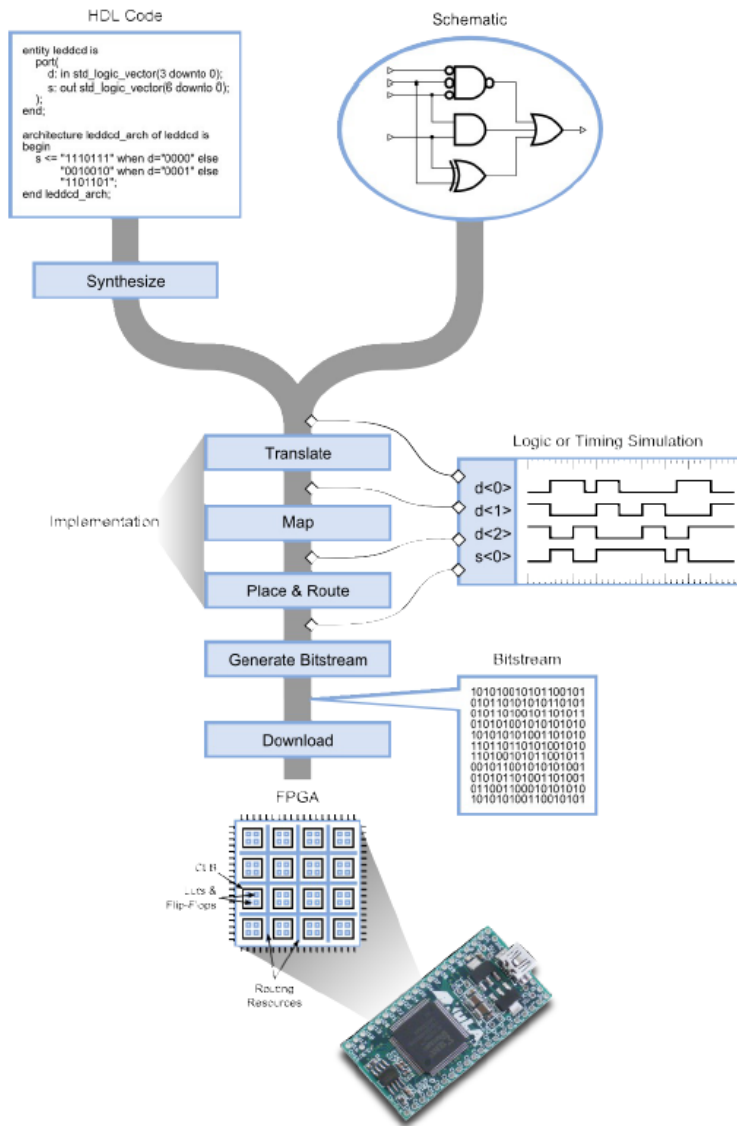


Figure 4.6: The typical design flow of an FPGA.

After downloading the bitstream into the device, it is possible to apply patterns of input signals (or test vectors) to the I/O pins of the FPGA to check the operation of the design. However, sometimes it's difficult to set up a particular combination of signals and look deeply into the internals of the design to see why it may not be performing as intended. For this reason, it is common practice to use a simulator to execute the design and confirm that the correct outputs are produced for a given set of test inputs before actually load it into an FPGA. Although problems with the size or timing of the hardware may still crop up later, the designer can at least be sure that his logic is functionally correct before going on to the next stage of development.

There are several places in the design flow where it is possible to perform a functional simulation. To debug the basic functions of a design, it is useful to run a logic simulation that only tests the logical operations of the gates in the circuit. Going down through the design flow, the netlist is augmented with more and more information about how the design will be placed into the FPGA. This allows to perform a more realistic timing simulation that incorporates the effects of gate and wiring delays on the operation of your circuit. This is useful for detecting errors caused when signals arrive too quickly or slowly at their destinations, but it has to be considered that timing simulations take longer to run than a pure logic simulation.

4.4 The device and the design tool used

The functions of the CLK-Board are implemented on a FPGA device of family Virtex-5 produced by Xilinx [75]. In order to move from the VHDL code to its physical implementation on FPGA, I used a proprietary software provided by the vendor: Integrated Synthesis Environment (ISE). ISE is a Computer Aided Design (CAD), i.e. a set of programs which cover all the design phases: from the synthesis of the logic to the definition of the layout of the resources into the device. ISE includes also a simulator which allows the user to check the correct the working of the circuit in the various design phases (for instance after the synthesis and after the layout definition).

In order to realize the project on the FPGA I initially used a ML505 [?] demo board from Xilinx (Figure 4.7). Demo boards are designed for the evaluation and testing of digital electronic circuits; specifically this board is built around a Xilinx Virtex-5 XC5VLX50T FPGA, which is interfaced to buttons, dipswitches, LEDs, seven-segments displays and other auxiliary hardware. In addition, the board includes an RS-232 interface, which was used for connecting the FPGA to a PC. On the board there is also quartz oscillators, providing the clock. The loading of the bitstream on the FPGA is performed trough a dedicated serial programming port (JTAG). The project on the evaluation board was used to take some measurement to evaluate the

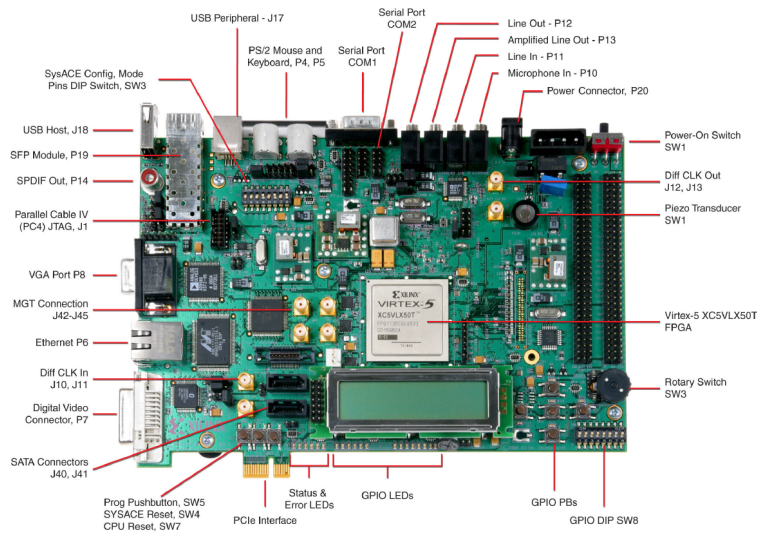


Figure 4.7: The ML505 evaluation board of Xilinx.

integrity of the clock distribution network (see section ??) and the occupation of the logic resources implementing a project as closer as possible to the final one. Most of required functionality of the CLK-Board were implemented and successfully tested on the prototype model:

- clock generation: 40 MHz and 400 kHz (98% duty cycle);
- RS232 interface with GPS device (using NMEA protocol);
- 1PPS GPS time interface;
- GTU counters for synchronization;
- dead and live time counters;
- data strobe interface (but not full SpaceWire).

I wrote the HDL description of the system, then I realized a prototype and I developed a test benches in order to verify the logic description of the project. The test benches stimulates the system by emulating the behavior of external elements, which it will be interfaced to once it will be in real operation: the other components of the DP. This methodology allowed me to verify the successful operation of the system permitted me to quickly develop and debug the firmware to be executed by the FPGA.

Then, in collaboration with a team of the Servizio Elettronica e Rivela-tori of Istituto Nazionale di Fisica Nucleare of Naples, I developed a board to hosts the FPGA, which is shown in Figure 4.8. The board has been designed to host also a 40 MHz clock generator, the DC/DC converter to feed



Figure 4.8: The CLK-Board of EUSO pathfinder. Apart from the FPGA, the board hosts the components to provide FPGA power and connections.

the FPGA, the JTAG connector and the connectors for CPU, CCB, HK, LVDS and external trigger signal, but also additional connectors, switches and buttons for test purpose. The clock generator is a 40 MHz Temperature Compensated Crystal Oscillator with a frequency stability of $\pm 1\text{p.p.m.}$ in the temperature range of -40°C to 85°C .

All the connections are point-to-point Low Voltage Differential Signaling (LVDS), in order to minimize the power consumption maintaining high speed and wide signal integrity connections. In addition, all the input are in failsafe mode to help system reliability by preventing errors. Failsafe guarantees that the outputs are in a known state when the receiver inputs are under certain fault conditions. Without the failsafe feature, any external noise above receiver thresholds could trigger the output to an unknown state. When the receiver inputs are open, not connected to the generator, or if the generator is powered off, the failsafe feature will drive the outputs in the safe state. If the receiver inputs are shorted, the outputs will be in failsafe mode.

In Figure 4.9 it is possible to observe the layout of the final CLK-Board project implemented in the FPGA. The device includes 18 and 36 kbit Block-RAMs, which are configurable with different address space and word width. The occupation of logic resources of the system is the 18% of the available resources, while the BlockRAM utilization is the 23%. All the timing constraints (maximum desired operating frequency, maximum skew on the clock distribution network, clock to output delay on the output pads and setup time on the input ones) posed on the design are met.

The hardware architecture designed is highly pipelined and parallelized in order to perform the necessary calculations as fast as possible and look-

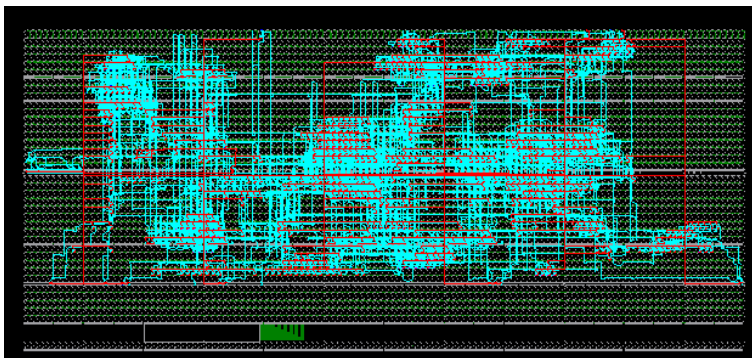


Figure 4.9: The layout of the final project of the CLK-Board implemented in the Virtex-5. The clock lines are represented in red.

ahead design technique were implemented. Look-ahead techniques force a portion of the large combinational logic function into the previous clock cycle, and force the remaining logic function to be performed in the next clock cycle. This technique, also known as register balancing, balances the levels of logic between registers, resulting in much faster execution. Thus, by splitting the combinational logic over two clock cycles, your logic can run faster without additional latency.

The CLK-Board of EUSO-Balloon was implemented in the industrial grade FPGA, in order to cope with the extended thermal range due to the high altitude.

The designed boards were tested along with the different firmware developed for TA-EUSO and EUSO-Balloon. In fact, even though the CLK-Board has to accomplish to the same tasks, there are some differences between the projects, principally in the interface with the two different GPS receiver. In what follows, the functionality and the implementation of the CLK-Board will be accurately described.

4.5 The CLK-Board

In this section I will describe the main block of the CLK-Board. The CLK-Board has to:

- generate and distribute the system clock and the synchronization signal to all the devices of the FS electronics;
- interface with the GPS receiver to collect, for each event, information on the position of the instrument and the UTC with a precision of few microseconds;
- receive the second level trigger signal and a release-busy signal from the CCB, to measure the live time and dead time of the apparatus

and to set the whole apparatus in a busy state;

- receive commands from CPU and transmit data to CPU by using the Space-Wire communication protocol;
- send trigger signals (provided by a CPU command or by an external trigger signal) to CCB. The trigger signal sent by CLK-Board is then forwarded to the PDM Board, which acquires the MAPMT photons counting and sends back a first level trigger signal.

In addition, the CLK-Board has to transfer all the monitoring parameter such as temperatures and voltages to the HouseKeeping. In order to make a clear description, the description of the functionality of the board will be divided according to the interface involved.

All the input and output lines of the CLK-Board are shown in figure 4.10. The lines are grouped by the DP component with which they are exchanged. The *clock* 40 MHz line comes from the oscillator hosted on the board.

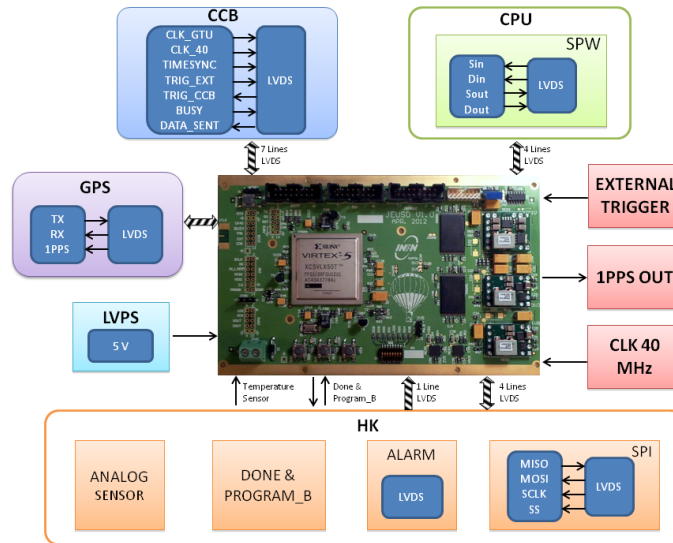


Figure 4.10: A scheme of the input and output lines of the CLK-Board. The lines are grouped by the DP component with which they are exchanged. Input are shown on the right, while output lines are on the left side.

Before analysing the interfaces, it is important to clarify how the acquisition process works. A time diagram of the data acquisition is shown in Figure 4.11.

When the PDM Board issues a first level trigger, it transmits all the data stored in a FIFO to CCB and then acquires new data. The event data are transferred to the CCB via a 8-bit wide, source synchronous data bus working at 40 MHz. After receiving the request command from the CCB,

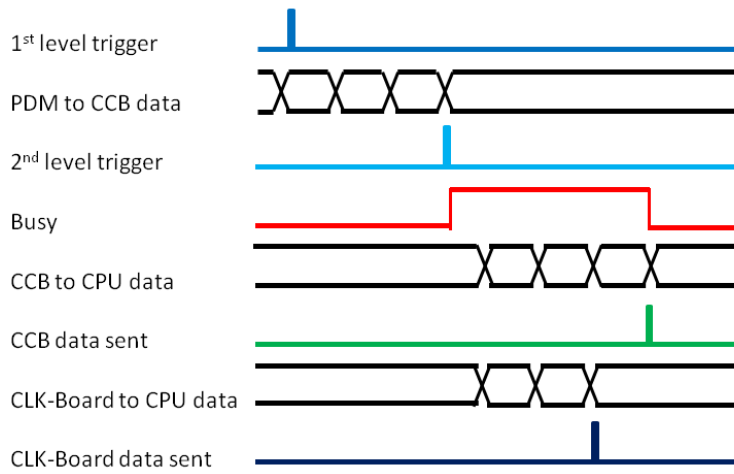


Figure 4.11: A time diagram of a standard acquisition. If the CCB does not assert the “Data sent” in —, the CPU issues a timeout and sends a command to CLK-Board to exit from the busy state.

the PDM will start the data upload within a time lapse of $20 \hat{I}\frac{1}{4}$ s. If the PDM does not comply within this time, the CCB will communicate the malfunction to the HK.

The data package is composed of one Event Summary (256 bytes data plus 2 bytes of CRC) followed by 128 GTU data frames. Each GTU data frame consists of 2304 bytes (48x48 pixels, 8 bit data) for PMT data and 288 bytes KI data, then the 2 bytes of CRC. In case the CRC algorithm detects an error, the affected PDM will be instructed to stop the current transmission via SPI. The PDM should keep the data and wait for another request from the CCB. If all data are received correctly a command is sent and the PDM is allowed to clear the event buffer. Assuming the size of 256 bytes for the Event Summary and 2 bytes for its CRC, 2304 bytes for the pixel data and 288 bytes for KI data and again 2 byte for the frame CRC, the total size of one event will be $256+2+128*(2304+288+2)=332290$ bytes and it will take about 8.3 ms to transfer it over the PDM Data bus.

The CCB, in turn, collects data from PDM, issues a second level trigger and sends a message to CPU. The 2nd level trigger is transmitted to the CLK-Board and the event is buffered in the CCB memory, ready to be transferred to the CPU upon receiving a dedicated command.

Upon trigger arrival from CCB, the CLK-Board tags the trigger arrival time and sets the system in a busy state, in this condition, the system is not able to receive other triggers. At the same time, the CLK-Board sends its set of data to CPU through the SpaceWire link. The CPU requests data from the CCB and is able to receive data from CCB and CLK-Board at the same time, using two different dedicated SpaceWire channels.

The CPU merges data from CCB and CLK-Board into an event saving it into disk. The data from CLK-Board are 537 bytes each, while data from CCB are roughly 330 kB, so the transmission takes more time. When the CCB finishes transmitting its data, it communicates the end of transmission to the CLK-Board through the dedicated line (“Data sent” in figure ??) and the CLK-Board releases the busy state, so the system can acquire other events. If there is some problems in the transmission between CCB and CPU, after a — the CPU issues a timeout and sends a release busy command to CLK-Board. In this way, the system is never stacked. At the initialization the detector is set in a busy state, that is released when the CPU sends to CLK-Board a command to start the acquisition (START-RUN command, see Table 4.4).

The role of the CLK-Board is essential for the data acquisition. At the moment the first level trigger is not implemented in the PDM Board, so data are acquired on a signal generated by CLK-Board. This signal is sent to the CCB and then propagated to the PDM Board, which starts the acquisition process already described. The CLK-Board can send this fake trigger signal both on a CPU command or using an external signal. This second option is particularly useful in TA-EUSO: sending the TA trigger signal to the external trigger input of the CLK-Board makes possible to acquire data in coincidence. In addition to these two main acquisition mode, two trigger mode linked to GPS signals are implemented. The first one is based on the 1 Pulse Per Second (1PPS) signal provided by the GPS receiver: once a second, in correspondence of the 1PPS, a trigger signal is forwarded to PDM board. This trigger can be used in OR with triggers from CPU or external triggers. The second one has been implemented for the EUSO-Balloon first flight in Timmins in order to synchronize the acquisition with the light emission from calibrated light sources, as will be described in section 5.5.3.

As normal operation the CLK-Board goes through a sequence of states, itemized in Table 4.1, to reach acquisition stage. In the start-up phases,

Table 4.1: States of CLK-Board working mode.

Status	Signal & command required	Signal & data sent
Initialization	Start run by CPU configuration parameter to GPS	Busy to CCB
Acquisition (trigger waiting)	External trigger Trigger by CPU Trigger by PPS Self-trigger	Trigger to CCB
Busy	Data sent by CCB Release busy by CPU	Data to CPU Busy to CCB

the CLK-Board needs to be switched on and configured correctly. This is

done by HK under the control of CPU. Since the GPS can be configured only through the CLK-Board, an additional initialization phase to configure the GPS is needed. After the initialization, the interfaces (SPW, SPI, GPS) have to be tested to verify that they are properly working. It is possible to do also a test of the entire acquisition chain. If everything is working, the CPU sends a command to start the acquisition phase. During the acquisition the CLK-Board has to accomplish different tasks. While it is waiting for a trigger from CCB, the CLK-Board has to be able to forward TA trigger or test trigger to CCB. When a trigger comes from CCB, the CLK-Board sends a busy signal to CBB and waits for data transfer request from CPU. CPU can request data in every moment. In addition, at every stage, the CLK-Board is always ready to detect malfunctions. In case an error is detected, the CLK-Board sets the alarm line at '1' and store information about the cause of the alarm in the alarm register. In case of alarm, the CPU can reset the CLK-Board through the HK or set a command to set the *busy* state (in which further triggers are inhibited).

The next paragraphs are devoted to describe how the specific tasks of the CLK-Board are implemented.

4.5.1 The clock generator

The time and synchronization system has to provide to CCB two clock signals:

- the system clock at 40 MHz, with a duty-cycle of 50%;
- the GTU clock, at 400 kHz, with a duty cycle of 98%.

These signals are forwarded to PDM-Board and, through this, to all the ASIC of the front end electronics.

In the board designed to host the FPGA was placed only an oscillator to generate a 40 MHz clock. The 40 MHz clock, also called system clock, is required by CCB, PDM and front-end ASICs to work. This signal is generated in the CLK-Board sending the clock coming from the 40 MHz oscillator mounted onboard to an LVDS driver.

Apart from generating the GTU clock, it is necessary to generate a 200 MHz clock to feed the SpaceWire interface and a 100 MHz clock for the time and synchronization system itself. The latter two clocks are generated by a Digital Clock Manager (DCM), coupled with a control circuit which monitors the operation. The DCMs in Virtex-5 FPGAs provide a wide range of powerful clock management features:

- clock deskew: the DCM contains a delay-locked loop to completely eliminate clock distribution delays, by deskewing the DCM's output clocks with respect to the input clock.

- frequency synthesis: separate outputs provide doubled frequency, but also frequencies derived from the input clock by simultaneous frequency division and multiplication. An internal calculator determines the appropriate tap selection, to make the output edge coincide with the input clock whenever mathematically possible.
- phase shifting: the DCM allows coarse and fine-grained phase shifting.

The DCM is a very powerful and delicate circuit, if the input clock is stopped for 100 ms or longer, the DCM powers down. The DCM needs an active high asynchronous reset signal, asserting the reset signal asynchronously forces all DCM outputs low after some propagation delay. To ensure a proper DCM reset and locking process, the reset signal must be held until the input clock signal is present and stable for at least three input clock cycles. In addition, the DCM must be held in reset until input clock is stable. For these reason the DCM a Finite State Machine (FSM) has been designed to control DCMs and provide them the proper reset signal. The DCM working as frequency digital synthesizer allows to obtain the 100 MHz and 200 MHz frequency from the input one, moreover, being based on Digital Delay Locked Loop, it allows to obtain clock signals which are perfectly in phase with the board clock at 40 MHz. The control circuit of the DCM works with the clock of 40 MHz and the plate is made

The 400 kHz clock, also called GTU clock, is strictly connected to the working mode of the SPACIROC ASICs. In fact, the Gate Time Unit (GTU = 2.5 μ s) is the basic time unit for the data acquisition and readout of the photo-electron counting performed by the digital block of the ASICs. As is shown in Figure ??, when the signal level is high, the present data are acquired and the previously acquired data are sent out to DAQ system via serial links, while when the signal is low the counters are resetted and the next acquisition is prepared. In addition, the GTU clock is used to feed the counters which measure event time, live time and dead time and is used for the time synchronization of all the electronics. In order to correctly reconstruct every event, merging data from PDM, CCB and CLK-Board, time information have to be in the data structure and have to be synchronized with a precision of a GTU.

The GTU clock is generated by a Finite State Machine (FSM) to obtain the required duty cycle and frequency, then this signal is routed to a clock buffer which drives it to dedicated clock routes in order to reduce skew and jitter.

The GTU clock is very important to guarantee the timing synchronization of all the electronics and the CLK-Board, after generating it, has to forward it to CCB. In order to send the GTU clock outside the FPGA, it was used an Output Double Data Rate (ODDR) with an input tied to ground and the other to V_{cc} , as suggested by the user manual of Virtex-5 device [[75]]. The signal at the output of the DDR is then sent to a LVDS

driver (OBUFDS), in this way it is possible to drive an high precision clock as best as possible.

4.5.2 The CPU interface

The CLK-Board communicates with the CPU through a SpaceWire link. The SpaceWire protocol has full-duplex capabilities permitting almost simultaneous transmission of both commands, from the CPU, and data, from the CCB. Moreover the high level protocol takes care of marking the frame edges. For this reason the end of frame is not added to the frame. All messages transmitted by the CCB to the CPU terminates with a 32 bit long Circular Redundancy Check (CRC) word. The CRC chosen is the CRC-32 IEEE 802.3 (Ethernet). In order to maintain a certain uniformity in communication protocols, the commands sent from the CPU to CLK-Board and CCB have the same format and both includes a 32-bit CRC. For the CLK-Board these commands have a length of three bytes. The first byte, called “msg_type”, identifies the type of command, while the following two constitute the pkt_number, the data command frame transmitted by the CPU to CLK-Board is shown in table ??). Commands are simple actions on the CLK-Board, but also read register requests.

The communication with the CPU is realized using the SpaceWire Light Core. The VHDL core has been configured at a frequency of 200 MHz, both in transmission and in reception, this translates into a transmission data rate of up to 200 Mbits s^{-1} . All the messages leaving the CLK-Board are provided with a 4 bytes CRC, in order to allow the CPU to assure data integrity. The general data structure of CPU commands, used both for CCB and CLK-Board, is constituted by three words of 8 bit divided as follows (see Figure 4.12):

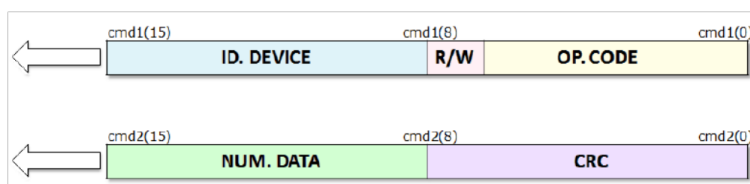


Figure 4.12: Data structure of a CPU command.

- ID. DEVICE (cmd1(7:0)): identifies the address of the device the CPU want to interact;
- R/W (cmd2(7)): is a single bit which determines whether the command requires a response message from the device polled;
- CMD CODE (cmd2(6:0)): defines the operative code of the command;

Table 4.2: Structure of the commands from CPU to CLK-Board. Every command is 3 B long. The message type is specified in table 4.4.

Message type	Packet number
1 byte	2 bytes

The CPU sends commands to the CLK-Board for several purposes, such as: receive the status register of the CLK-Board, to request the generation of a trigger or interrupt status busy in which is located the CLK-Board, subsequent to the generation of a trigger. If the command received from the CPU, is not correctly interpreted, the CLK-Board responds by sending a packet of 10 bytes: the first byte contains the code of the nack (X“4C”), the following three are the repetition of the command received by the CPU, followed by two bytes of the status register of the CLK-Board and of the GPS receiver, while the last 4 bytes constitute the CRC (table 4.4).

Table 4.3: Structure of reply in case of non acknowledged commands, i.e., commands not listed in table 4.4. The NACK message starts with the X“4C” word and it is 10 B long.

Nack X“4C”	Received command	CLK-Board register	GPS register	CRC
1 byte	3 byte	1 byte	1 byte	4 byte

The communication protocol between CPU and CLK-Board provides that, upon receipt of a second level trigger by the CCB, the CLK-Board put the system in BUSY and send a packet to the CPU (the format of which is shown in table 4.5) of 537 bytes, with information such as: the number of the packet, the number of event, the time at which the second level trigger from CCB has been received (which must be the same content in the CCB data), information from the GPS receiver, 4 bytes for the current live time, 3 bytes for the dead time of the previous event, 1 byte for the status register of the CLK-Board, 1 byte for the status register of the GPS receiver and finally 4 bytes for CRC.

The counters of live and dead time are controlled by signals from CPU and CCB. In fact, the CLK-Board begins to count the dead time as soon as a trigger arrives from the CCB by means of a dedicated line. At the same time, the CLK-Board moves to busy state. As soon as the CCB has sent all the data related to the event, it sends a signal DATA_SENT on the appropriate line and CLK-Board stops counting dead time and wakes from BUSY. The output from the state of BUSY can also take place through a dedicated control by the CPU (in case of timeout).

The trigger time in the event header is based on the GTU counter in the

Table 4.4: List of the commands from CPU to CLK-Board.

Command	Value
START RUN	X“02”
RELEASE BUSY	X“03”
CPU TRIGGER	X“04”
GET DATA	X“05”
SET BUSY	X“06”
STOP CLOCK: test command	X“07”
SET GPS	X“08”
DISABLE GPS	X“09”
RESET GTU COUNTER	X“11”
RESET PACKET NUMBER	X“12”
RESET TRIGGER COUNTER	X“13”
RESET ALL COUNTERS	X“14”
ENABLE TRG BY PPS	X“15”
DISABLE TRG BY PPS	X“16”
MASK EXTERNAL TRIGGER	X“17”
UNMASK EXTERNAL TRIGGER	X“18”
ENABLE SELF TRIGGER	X“19”
DISABLE SELF TRIGGER	X“20”

Table 4.5: Structure of CLK-Board data. Every data is 337 B long.

Lenght (byte)	Value (LSB first)
4	Packet number
4	Event number
4	GTU number (relative to last trigger)
512	GPS data
4	Live time
3	Dead time
1	CLK-Board status register
1	GPS receiver status register
4	CRC

Clk-Board which is reset at every run.

Flag to distinguish the source of the trigger.

Table 4.6: Content of the CLK-Board status register. In standard operating conditions, before starting a run, the CLK-Board status register value is X“1f”.

Bit	Value
7	Flag trigger from CCB
6	Flag trigger from CPU
5	Flag external trigger (includes also TA and 1PPS)
4	Busy signal
3	Flag SpaceWire txrdy
2	Flag SpaceWire running
1	DCM 200 MHz locked
0	DCM 100 MHz locked

Table 4.7: Content of the GPS receiver status register. In standard operating conditions, the GPS receiver status register value is X“06”.

Bit	Value
7	0
6	0
5	0
4	Self trigger enabled
3	1PPS trigger enabled
2	1PPS signal present
1	data present
0	Flag GPS not used

In self trigger mode, a trigger pulse is produced every 50 ms (20 Hz), starting by 1PPS signal. This signal is generated using a counter feed with the GTU clock and resetted by 1PPS signal.

4.5.3 The HK interface

As described in section ?? the Housekeeping board has to manage the reset and the switching on and off of all the subsystem of the DP and of the PDM board, in addition, it has to monitor voltages, temperatures and alarm for the same components. Through the HK, the CPU can control all the systems involved in the data acquisition.

The lines of the interface between the CLK-Board and the HK are shown in Figure 4.13. The SPI lines allow to transmit voltages, temperatures and other data monitored by HK, there are two dedicated lines for alarm and reset. In addition to these lines, there are two line external to the FPGA,



Figure 4.13: Input and output lines of the interface between CLK-Board and HK. All the lines are LVDS lines.

Program B and *Done*, needed to control the programming the FPGA and to control its status. The *Program B* has to be high for at least 3ms to reprogram the FPGA [75], while the *Done* line goes to '1' when the FPGA is programmed and ready to start working. The *Done* line is monitored all the time by HK to detect if there is some problem and the CLK-Board needs to be reprogrammed. A low state in *Done* line indicates a case of alarm and HK respond immediately sending a pulse on *Program B* line.

Both the alarm line and the reset line are active high. The reset needed by the Virtex-5 has to be long at least 3ms. Concerning the alarm line, it is given by the OR product of all the lines of the alarm vector and can be switched off by HK sending a command. In order to generate high priority alarms, the Housekeeping has to detect a change of level in the *alarm* line, then HK asks to the subsystem for its alarm register and finally HK sends to CPU the alarm which generates the change of level.

The SPI interface has been realized implementing a core. The same core was implemented in CCB and PDM in order to have an uniform behaviour of the three systems. The implemented SPI protocol has the following characteristics:

- master-slave: the HK is the master;
- multi drop: every subsystem is polled with a different chip select line;
- full duplex;
- synchronous;
- data transfer rate = 2MBs^{-1} ;
- the information are exchanged in byte format, one bit a time.

In Table 4.8 is reported the list of the commands that the CLK-Board is able to receive from HK. The HK can read the CLK-Board and the GPS receiver status register to understand if there is some problem and can ask for the alarm register in case the alarm line, given by the OR of all the alarm register bit, goes high. The content of the alarm register is reported in table 4.9.

Table 4.8: List of the commands from HK to CLK-Board.

Command	Value
Send "0F" (test command)	X"01"
Send Alarm register	X"02"
Set alarm line (test command)	X"30"
Reset alarm line and register	X"03"
Send Status register of Clk-Board	X"40"
Send Status register of GPS	X"50"
Send temperature LSB	X"60"
Send temperature MSB	X"06"
Send Vccint LSB	X"70"
Send Vccint MSB	X"07"
Send Vccaux LSB	X"80"
Send Vccaux MSB	X"08"
Send Date 1st byte	X"10"
Send Date 2nd byte	X"11"
Send Date 3rd byte	X"12"
Send Date 4th byte	X"13"
Send Time 1st byte	X"14"
Send Time 2nd byte	X"15"
Send Time 3rd byte	X"16"
Send Time 4th byte	X"17"
Send Date 5th byte	X"18"
Send Date 6th byte	X"19"
Send Date 7th byte	X"1a"
Send Position 1st byte	X"1b"
Send Position 2nd byte	X"1c"
Send Position 3rd byte	X"1d"
Send Position 4th byte	X"1e"
Send Position 5th byte	X"1f"
Send Position 6th byte	X"20"
Send Position 7th byte	X"21"
Send Position 8th byte	X"22"
Send Position 9th byte	X"23"
Send Position 10th byte	X"24"
Send Position 11th byte	X"25"
Send Position 12th byte	X"26"
Other	X"FF"

Table 4.9: Content of the CLK-Board alarm register. In standard operating conditions, the alarm register values X“00”. The alarm line is given by the OR of all the alarm register bit and it is active high.

Bit	Value
7	200 MHz SpaceWire clock stopped
6	100 MHz internal clock stopped
5	Data from GPS non received
4	1PPS signal from GPS not received
2	Voltage V_{core} out of range
1	Voltage V_{aux} out of range
0	FPGA over temperature

4.5.3.1 Alarms

If an alarm is detected, the CLK-Board informs the HK via alarm line. There are several alarm conditions related to the FPGA configuration, the interface working and the GPS state. Every alarm condition, independently from the cause, sets the alarm line at 1. The type of the alarm is stored in the alarm register which can be read by HK upon a command request from CPU. After the reading of the alarm register, the alarm is masked.

2.1 Over temperature

The values of temperature sensors are sent to the HK. No alarm is related to them.

2.2 CLK-Board not configured

When the FPGA is not configured the DONE line goes to 0. This is a normal condition in the start-up phases, but in the other phases it represents a malfunction. Through the DONE line, the HK can detect this problem and report it to CPU. The CPU has to reset and reprogram the FPGA. If this is not enough, the CPU switches off the corresponding CLK-Board power supply and switches it on after a certain (TBD) period of time. Then, the procedure of start-up has to be undertaken.

2.3 GPS crash

If the PWR CHK line from GPS goes to 0, the CLK-Board detect the problem, stores the information in the alarm register and set the alarm line to 1. Then, the CPU has to check the power supply of GPS and to send to CLK-Board a request of a reset of the GPS. If the PWR CHK line does not go to 1 after a certain period of time, the CPU has to switch the GPS power supply OFF. When the GPS is turned off, the CPU sends to the CLK-Board a command to switch it in the working mode without GPS.

2.4 Communication error on SPW link

Alarm is sent to the HK. The alarm register is set and must be read from CPU. The CPU resets and restarts the link.

2.5 Communication error on SPI link

Alarm is sent to the HK. The alarm register is set and must be read from CPU. The CPU resets and restarts the link.

2.6 Errors from GPS

Errors from the GPS can be of two types: absence of PPS signal or transmission of an incorrect message. When the CLK-Board detects a problem, it stores the information in the alarm register and sets the alarm line to 1. Then, the CPU sends to CLK-Board a request of a reset of the GPS. If the GPS does not work correctly after a period of time sufficient for a cold reset, the CPU switches off the GPS power supply and switches it on after a certain period of time. Afterwards, the procedure of start-up has to be undertaken. If the problem persists, the CPU has to switch the GPS power supply OFF. When the GPS is turned off, the CPU sends to the CLK-Board a command to switch it in the working mode without GPS.

4.5.4 The GPS interface

The GPS receiver has already been introduced in section 4.1, here I want to focus on the interface with the GPS receiver from the point of view of the CLK-Board. The lines of the interface between the CLK-Board and the GPS receiver are shown in Figure 4.13. All the lines are LVDS lines, in order to minimize —.



Figure 4.14: Input and output lines of the interface between CLK-Board and GPS receiver. All the lines are LVDS lines.

trasmissione comandi uart ricezione comandi con identificazione inizio

GPS data: There are two modes of acquisition of time information: with and without GPS. The GPS mode is the default working mode, the other is activated when the GPS is not working. The switching between the modes of acquisition when GPS does not work are described in the alarm section.

In standard working mode, the CLK-Board retrieve timing information from GPS. Every time the system is switched on it is mandatory to set up GPS to send the data needed. After the FPGA configuration, the CPU drives the requirement of a set of data with specified periodicity to the GPS. The available GPS messages are:

- GGA Time, position and fix type data
- GLL Latitude, longitude, UTC time of position fix and status
- GSA GPS receiver operating mode, satellites used in the position solution, and DOP values

- GSV Number of GPS satellites in view satellite ID numbers, elevation, azimuth, SNR values
- MSS Signal-to-noise ratio, signal strength, frequency, and bit rate from a radio-beacon receiver
- RMC Time, date, position, course and speed data
- VTG Course and speed information relative to the ground
- ZDA PPS timing message (synchronized to PPS)

4.5.5 The CCB interface

The lines of the interface between the CLK-Board and the CCB are shown in Figure 4.15. As seen in the previous section, the CLK-Board has to feed



Figure 4.15: Input and output lines of the interface between CLK-Board and CCB. All the lines are LVDS lines, in order to maximize signal integrity.

the CCB with the clock signals. In addition, there are two input and two output lines related to the data acquisition process described in section 4.5 and a time synchronization signal.

The time synchronization of the apparatus is one of the fundamental tasks performed by CLK-Board. This features is inherited by the JEM-EUSO design, in fact, tagging every event with a time stamp by PDM, CCB and CLK-Board will permit to detect if an event is seen by several PDM.

The synchronization works in the following way: upon a first level trigger generation, the PDM sends a data packet and the CCB tag this packet with a time stamp, which represents the time of the event. When a second level trigger is issued by CCB, the CLK-Board tags the event with another time stamp, this number is stored along with the UTC time received from the GPS receiver. Thus the CLK-Board can associate to every event an absolute time tag.

Since it is necessary the basic time unit is the GTU, the GTU clock is used to feed counters which permit to associate a number of GTU to every trigger. The time stamp is given by the number of GTU counted by the GTU counter implemented in each board. To get a time synchronization it is necessary to initialize all the counters at the same time. At the start of every run the CLK-Board initializes all the counters by a Time-Sync

signal, which is used as an asynchronous reset. The Time-Sync signal is generated in correspondence of every transition from '0' to '1' of the 1PPS signal coming from the GPS receiver in order to have a time tag with a precision of the order of a GTU and coherent with UTC.

The Time Sync signal is generated at the start of every run. In the standard working mode, when the CLK-Board receives a START RUN command from CPU, it waits until the next 1PPS signal coming from GPS and then sends the Time Sync signal to CCB. If there is some problem and the GPS does not the 1PPS signal, the CLK-Board issues an alarm and the CPU can switch the acquisition in a mode without GPS. In that case, the Time Sync signal is sent in correspondance of the receipt of a START RUN command.

Chapter 5

EUSO-Balloon Integration

The EUSO balloon instrument was fully assembled and tested in Toulouse at IRAP before being packed for the transportation to the launching site in Timmins (Canada). It was re-assembled on launching site with a minimum of functional tests and optical alignments before the flight.

The Figure ?? shows the basic time sequence of the main Assembly, Integration and Tests (AIT) operations and the site where they were performed. Some parts were assembled and integrated in parallel step by step. The integrated parts were then merged together building more and more the detector. Early phase consisted in building the detector electronics in parallel to the analog and digital electronics and the computing electronics. The optics were tested in parallel. During the last phase, the electronics as a whole, the mechanics and the optics were mounted as the final instrument and then the latest tests were performed.

Before the integration took place, the flight model of all the EUSO-Balloon DP subsystems have been produced with their spares by the responsible organization. Each sub-assembly has been tested by using hardware emulators as external interface to check if they fulfil the functional requirements. LVPSs have been tested by simulating the maximum load. Flight models of the cables have been produced. Every component has been realized using industrial grade components to cope with the thermal challenges, nevertheless, environmental test inside a climate-chamber in low-pressure environment have been performed for all the sub-assemblies as stand alone system to finalize the thermal management.

In this chapter every phase of the integration and assembly which involved the Time and Synchronization System will be shortly reviewed.

5.1 DP Integration in Naples

The first step of the integration which involved the CLK-Board was the integration of the Data Processor (DP). The block diagram of the DP is

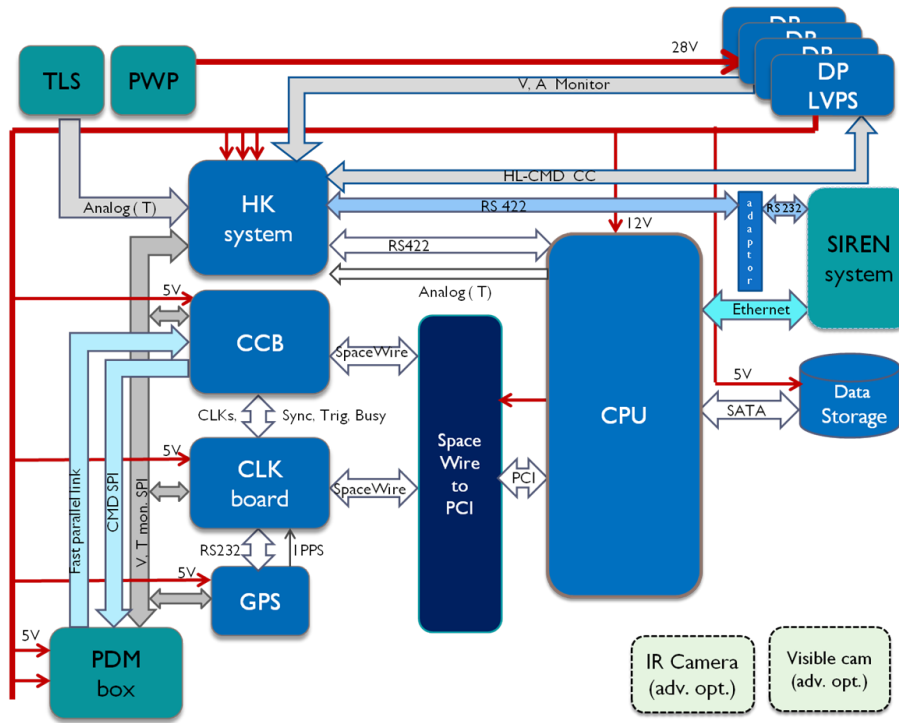


Figure 5.1: Functional block diagram of the Data Processor.

shown in Figure ?? to recall all the subsystems.

The flight model of the DP was successfully integrated and tested in Naples in the period November 2012-July 2013 by a team of people coming from Naples, Rome, Bari, as well as from Germany and Mexico. All the mechanical interfaces, the electrical interfaces as well as the cables were successfully tested. The most significant step taken in Naples was the implementation of the communication channel CPU-Housekeeping and the development of the procedures. In this section the results of the various steps of the first integration are reported.

The EUSO-Balloon flight DP Eurocard subrack box with all the subsystem finally integrated is shown in Figure 5.2.

The DP system is controlled through CPU connected to a console and to a GSE-CPU (a dell laptop installed with scientific linux) acting like a server for command and data. To supply the DP was used a 28 V laboratory power supply.

The DP-AIT activities took place into several sub-phases corresponding to the progressive integration of the electronic modules.

The first step was LVPSs test and integration with HK. At this stage the analog reading line (monitor line), the high level command to turn ON/OFF LVPS by HK, the contact closure and the cable compatibility for CLKB,

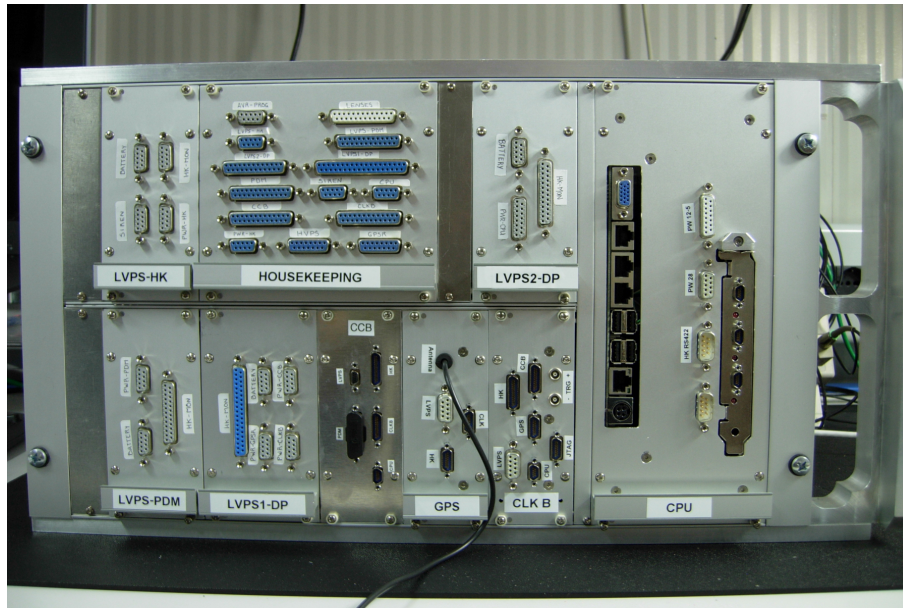


Figure 5.2: View of the Data Processor.

CCB and GPS were checked and tested. Then the CPU was added to the first step configuration to test the CPU-LVPS power connection and the CPU/HK serial connection. This means that not only the LVPSs and HK mechanical and electrical integration (plug-in unit, cables and connectors) were checked, but also the CPU-HK communication through the RS422 line. During this test CPU settings, HK Arduino settings and cable and connectors were checked.

The following step of the DP integration involved the Timing and Synchronization system and the LVPS and HK. After testing mechanical and electrical integration, the communication between CLK-Board and GPS receiver through a bidirectional serial link and the correct exchange of the PPS signal were tested. Finally, the CLK-Board/HK and the GPS receiver/HK communication through a SPI interface were performed. The full series of commands needed to send by HK the commands to get the data from the GPS has been tested successfully. The interface between CLK-Board and HK is more complex, because it includes also the lines required to configure, reset and check the configuration on the FPGA (see chapter ??). All these lines, together with the alarm line and the lines foreseen by the SPI protocol were tested and validated.

After the integration of the CCB to check its interfaces with HK. The next phase of the integration has been devoted to the communication between CCB and the CLK-Board. These tests were performed first without and then with an emulator of the PDM Board sending fake data. The tests of the interface between CLK-Board and CCB included also the verification

of the time synchronization of the system and the correct broadcast of all the signal related to the data acquisition, such as 2nd level trigger, external trigger and busy signals.

The last phase of the integration was devoted to the communication of the CPU with the CLK and the GPS through SpaceWire. Tests of communication between the CPU and the CCB and then between the CPU and the CLK board at a rate of 200 Mbit/s were performed successfully. Besides checking all the commands, using the external trigger, data were acquired and stored on disk, checking the integrity and the reliability of the data with a Cyclic Redundancy Check. It was verified as well that the transfer time was inferior to the dead time and it was simulated an alarm condition which required a reset from CPU by HK to check the proper functionality of the whole DP.

At the same time, the core of the CPU software which has to control the instrument and the data acquisition has been developed. Test of the data handling procedures were performed by simulating the acquisition procedure of CCB dummy packets and Clock Board data packets. This allowed us to characterize the performance of the system with the time necessary to transfer data and write data to disk. For our first tests we used an external signal (with a frequency of 500 HZ) as a trigger signal to acquire 1000 events.

For each event a packet of 330 kBytes containing the information provided by the 36 ASICs is transferred from the PDM board to the CCB through a 40 MHz 8 bit parallel bus and then from CCB to CPU together with the data of the CLK board (GPS data, dead/live time and GTU time of the event) through Space-Wire connection. The measured time needed to the CPU to transfer the data (~330 kB) from the CCB to the disks where they are written is of about 20 ms per event (50 Hz as max sustainable trigger rate in the technical specifications). For each event we measured the time of the event (GTU), the time required to the system in order to transfer and store data on disk (dead time, T_{dead}) and the time elapsed waiting for a new trigger (live time, T_{live}) with a time resolution of one GTU. The most critical data transfer is the one on the CCB-CPU Space-Wire bus, comparing the dead time (see Figure 5.3) and time needed to transfer the data with the Space-Wire protocol, it results that the data writing on disks does not affect the dead time.

In addition, the Ground Support Equipment (GSE) software, which allows the control of the instrument by remote, was developed in this phase of the integration. The GSE software simulates the control of the instrument as it should be performed by Siren system interfacing the HK through a RS-232 port and the CPU through Ethernet. The full list of commands needed by CPU to require HK to switch ON/OFF of sub-assemblies, receive and manage alarms, send reset, etc., was developed and implemented. More in detail, the system was able to react to alarms sending a reset signal and/or with the shut-down and the restart of the system. In total, 800 commands

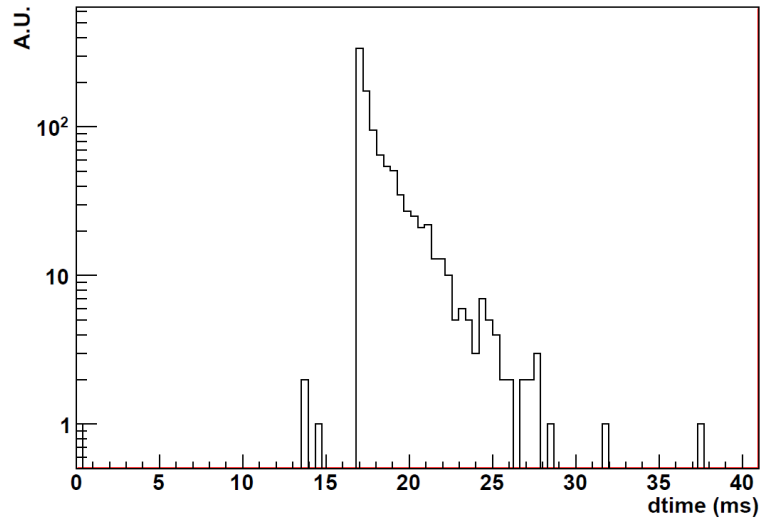


Figure 5.3: The dead time distribution.

have been implemented to manage the Housekeeping by the CPU and all the procedures have been defined.

At the end of the DP integration in Naples the CPU was able to read all the monitoring parameters (temperatures and voltages) through the Housekeeping and also the command part was implemented.

Finally, it was defined a start-up sequence with established procedure to guarantee the correct functionality of the system. It was established the sequence of operation to perform at DP turning on:

1. start switching on sequence monitoring power consumption for each sub system switched on (HK, GPSR, CLKB and CCB);
2. check of the HK parameters (temperatures, voltages and currents) for each subsystem through the GSE-CPU;
3. check of the HK parameters (temperatures, voltages and currents) for each subsystem by sending HK commands from the GSE-CPU through the serial port;
4. set the CCB in Dummy mode to perform acquisition tests;
5. start an acquisition of one event and check data from CLK-Board and CCB (dummy data).

The procedure was operated many times without any problem, the data transmitted by CLK-Board and CCB were controlled and verified. The measured dead time and live time were checked to be compatible with the specification. Details on these results will be shown in the section describing the results of the test of DP + PDM integration.

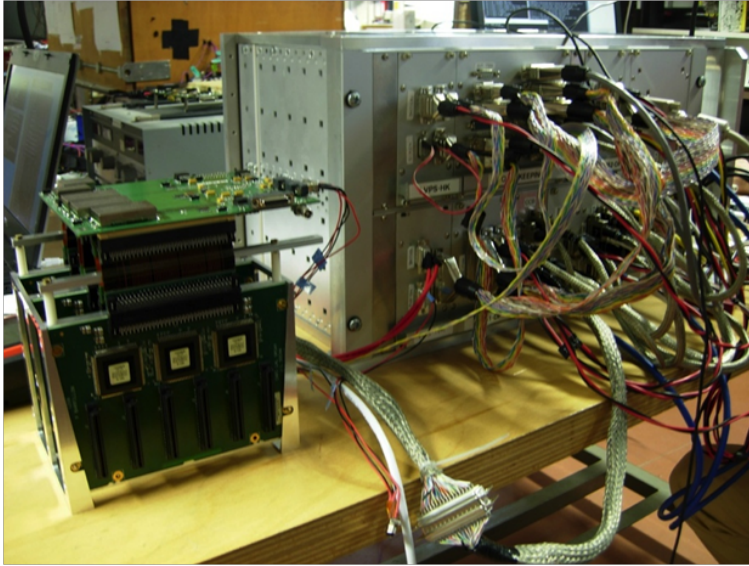


Figure 5.4: The Data Processor connected with the PDM Board.

All the requirements (functional and mechanical, for the interfaces, the power and the weight) were tested and successfully verified for all the sub-assemblies of the DP. The measured performance of the integrated system in acquiring and storing data fulfilled all the requirements.

5.2 DP-PDM Integration test at APC, Paris

The following step of the complex management of the DP foresees the implementation and the tuning of the interaction with the High Voltage Power Supplies and the PDM Board and, consequently, with the readout ASICs of the Photo-Detector Modules. The DP had to be able to manage both the data acquisition from MAPMT and the monitoring of the PDM Board functionality parameter through the Housekeeping.

DP elements (HK, LVPS, CCB, CPU, CLK-Board and GPS receiver) and PDM elements (HVPS, EC-ASIC, EC-units and PDM board) were integrated at APC, in Paris from October 2013 to February 2014. After the integration, the DP was able to manage both the data acquisition from MAPMT and the monitoring of the PDM Board functionality parameter through the Housekeeping. This step allowed us to calibrate the MAPMT and to improve data acquisition procedures.

In Figure 5.4 there is a picture of the DP integration with the back-plane of the PDM (without the EC-units, which can be tested only in a black-box). Figure 5.5 shows the main interfaces which have been tested between the DP and PDM and the type of signals/data exchanged between them. As

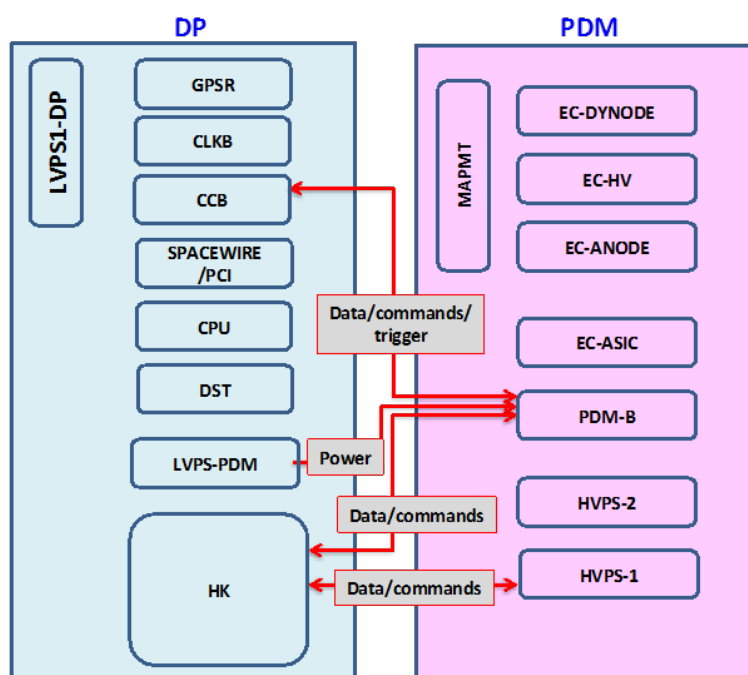


Figure 5.5: The dead time distribution.

shown in figure 5.5, the integration of the PDM and the DP concerns the following items :

- LVPS-PDM/PDM Board;
- HK/PDM Board;
- HK/LVPS;
- CCB/PDM Board.

In those tests, the DP was still powered by the 28 V laboratory power supply, while the PDM received its power from LVPS-PDM which is inside the DP.

Clearly, the first objective was to power the PDM board with the corresponding DP LVPS, to show that LVPS-PDM was able to withstand the powering of the PDM-Board + 6 EC-ASICs. Once powered, the PDM was connected with the HK to check LVDS compatibility and cable compatibility of the SPI line. After that, the connection between PDM and HK was implemented and the software to enable the communication between the two subsystems through the SPI interface was developed and tested. The sending of the commands, the data transmitted and the different procedures were verified acquiring the housekeeping parameters of the PDM board (voltages and temperatures) and testing the alarm and reset lines. Finally the HK ON/OFF commands to HVPS were tested, this was a double test: for the

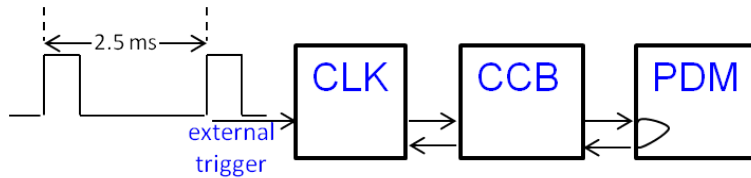


Figure 5.6: The standard setup for data acquisition test taken using an external trigger signal.

HK firmware to manage properly the switching on of the HVPS after an interrupt and for the HV ramping up/fall down behaviour in time.

The main interface between DP and PDM is the one between CCB and PDM board. Commands are sent from CCB to PDM board through a serial SPI link. On the other hand, the PDM board, on request, sends data to CCB through a parallel bus. This interface was continuously tested while the firmware of the PDM board was developed or adapted. The validation of the interface included the checking of:

- the proper configuration of the ASICs (electronic gains, thresholds);
- the sending of commands from CCB to PDM through the serial SPI link;
- the sending, on request, of data from PDM-Board to CCB through a parallel bus;
- the data transfer rate and stability.

Of course, these tests not only involved the CCB and the PDM board but also the whole DP chain (CPU, CLK-Board, data storage, etc) and the EC-ASIC boards. In Figure 5.6 is shown the standard set-up used during these tests.

The last step of the PDM+DP integration was a full acquisition: the whole data acquisition chain has been completed and validated. It has been possible to detect the photons counting with the MAPMT sending a data request from CPU to Clock Board or using an external signal. In fact, this signal is propagated through the chain Clock Board-CCB-PDM and then the photons counting is sent back to the CPU through all the electronics and the data are stored in the data storage by the CPU. These tests required adjusting the hardware interfaces between the single DP elements and developing proper software protocol for the exchange of commands and data between the hardware elements.

The standard test procedure foresaw the acquisition of 1000 events using as a trigger an external signal at CLK-Board input at a 500 Hz rate. For each event a packet of 330 Kbytes containing the information provided by the 36 ASICs is transferred from the PDM board to the CCB and then

from CCB to CPU together with the data of the CLK-Board (GPS data, dead/live time and GTU time of the event). Moreover, it was performed a data acquisition performance test: for each event the time of the event (GTU), the time required to the system in order to transfer and store data on disk (dead time, Tdead) and the time elapsed waiting for a new trigger (live time, Tlive) were measured.

Preliminary functional tests were performed at APC before shipment to Toulouse, but the complete electronic system PDM + DP was mainly and intensively tested at IRAP during the final integration steps.

5.3 Thermal Vacuum test at CNES, Toulouse

The purpose of the environmental tests was to check that the electronics worked in its defined temperature range [0 °C - 50 °C], in the low-pressure (3 mbar) conditions expected at 40 km altitude.

All the DP components (CPU, CLK-Board, GPS, CCB, HK, LVPS, etc) were successfully tested in temperature chambers within the range [-20 °C - 50 °C] and at 3 mbar. Since the LVPS-HK shown an anomaly during the global test in Simeon, the board was re-produced and re-tested.

The integrated DP+PDM subsystems were tested together in the SIMEON vacuum chamber (see Figure 5.7) at 3 mbar in a temperature range of [0 °C - 50 °C].

The purpose was to ramp down quickly the pressure, to turn on/off both subsystems and to measure the temperature evolution recorded by thermocouples located in several places of the electronics. A radiator plane was designed to ease electronics cooling in a low pressure environment (see Figure 5.13a).

The test procedure was the following:

- start every subsystem at room temperature of 20 °C;
- every system is switch off, except HK which may run on the electronics later;
- decrease the pressure quickly from 1 bar to 3 mbar;
- observe the temperature evolution when every system is off;
- turn on every subsystem one by one;
- observe the temperatures evolution when every system is on;
- observe if some failure occurs;
- check that the temperature remains in the range of [0 °C - 50 °C] at 3 mbar.



Figure 5.7: Figure 36 The CNES Simeon environment chamber.

During the test, several operation were performed to check that the system was working functionality:

- DP + PDM Board: test of communication;
- DP + PDM Board + ASIC boards + HVPS: test of the different levels of the high voltages;
- DP + PDM Board + ASIC boards: S-Curves of the 2304 pixels were acquired around the pedestal.

Since the HVPS have been found unable to power the 9 EC at 3 mbar, the whole PDM-System (the PDM included PDM-Board cooling plate and the HVPS, EC-ASICs boards, etc) has been tested lately in a low-pressure chamber at 3 mbar at APC. During this test, all the PDM was turned on and temperature variations were measured with thermocouples placed at critical places. It was possible to acquire data at the level of the whole PDM, but with a very low gain. Then an additional test in Simeon was done to validate the use of the whole PDM at 3 mbar.

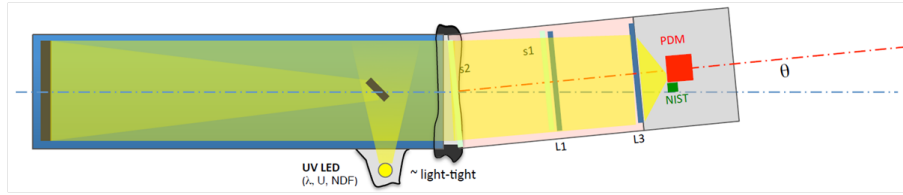


Figure 5.8: Basic proposition for the optics test: a LED is placed at the focus point of a Newtonian telescope called the collimator to produce a parallel light beam of 1 meter diameter at the entrance of the EUSO-BALLOON instrument. For optics test a CCD camera and NIST photodiode were used, while for final test (see paragraph 5.5) the LED was replaced by a LED flasher and the CCD camera was replaced by the real detector (PDM).

The whole chain (PDM+DP) integrated on its radiator has been tested for a second time in the Simeon facility, at 3 mbar. The test shown the capability for the whole chain to acquire data in the nominal way at 3 mbar, validating in particular the possibility to power all the PDM photocathodes simultaneously at 950 V.

Since the HVPS subsystem shown a weakness around 0 °C in Simeon, the boards have been tested in a climatic chamber at APC and finally, the HVPS subsystem has been validated on the smallest range of [3 °C - 50 °C].

5.4 Other integration tests

In the previous sections the PDM-DP integration was described, but the first phases of the EUSO-Balloon integration included also the mechanical integration, the Power Pack (PW) box assembly the lenses integration and the optical alignment. The mechanical integration included the mounting of the lenses in the instrumentation booth but also the design and test of the thermal protection of the instrument and was done at IRAP. The PWP box was designed by RIKEN, while the box was fabricated by IRAP and the battery cells were provided by CNES. The integration of the PWP consisted in soldering batteries cells in the PWP box and it was performed at IRAP. The optical system of lenses, once inserted in the instrument structure was qualified according its optical properties. The experimental setup is shown in Figure 5.8: a 390 nm LED is placed at the focus point of a Newtonian telescope called the collimator to produce a parallel light beam of 1 meter diameter at the entrance of the EUSO-BALLOON instrument. The different measurements on the focal plan were obtained by a CCD camera and NIST photodiode (calibrated photodiode), for several incident angles and wavelengths. A set of three qualification measurements were performed:

- focal length, to know where to put the PDM-FS along the telescope axis;

- transverse profile of the spot (point spread function measurement);
- throughput of the system.

The focal position z_0 was found by minimising the spot size when moving the CCD detection plane along z the optical axis. The point spread was measured by scanning the transverse profile of the beam with the CCD camera and the NIST power meter at the focal distance z_0 . The measurement of the throughput of the system was intended to determine the light transmission coefficient of the optical system. The transmission was evaluated by sending a calibrated light beam from the collimator on the instrument aperture and measuring the light flux on the focal plan with the PhotoDiode NIST. The calibrated light beam was obtained by sampling the light beam from the collimator by a PhotoDiode NIST on the instrument aperture.

5.5 Full integration test at IRAP, Toulouse

Once every system was assembled and tested, the whole system was assembled at IRAP and the global tests phase started. The main steps were the following:

- functional tests of the telemetry (TM) with NOSYCA;
- full instrument performances test;
- autonomous instrument tests;
- campaign simulation tests.

During ground AIT activities, the electronic modules had to be connected to the ground equipments, however the electrical section had to be light-tight to avoid stray light damaging or destroying the MAPMTs polarised with their HV, so a feed-through plate called “hatch” has been produced. During AIT, external cables were connected to the hatch, while during the flight, the cables were replaced by plugs and the hatch was closed. After mounting the hatch, a control of the good electrical connection and good health tests was performed to validate the good integration of the electrical section, then some tests of the Siren-DP interface through the hatch were done.

With the hatch closing the instrument, the telescope can be considered as a black box in which it is possible to perform health test involving light detection. The aim of this kind of tests was to perform:

- good health tests of each subsystem;
- functional test of the instrument (with the whole electronics subsystem connected);

- acquisition of (fake) images.

During laboratory tests, the CPU and the HK were controlled by laptops and the LVPS-HK was set on thanks to a connector consisting in 2 jumpers. In flight conditions, the SIREN system controls the CPU, the HK and enable the LVPS-HK. The communication between SIREN and these elements has been tested thoroughly at IRAP. The connections were done through the hatch as they were for the flight. The network parameters of the CPU and the GSE were configured according the flight network configuration defined by NOSYCA/Siren system.

The first test was the sending, from the GSE console, of several commands to switching ON/OFF the LVPS-HK through the Siren interface. The LVPS-HK was properly switched on and off according the command sent. The second test was to validate the serial communication between the HK (RS422) and the Siren system (RS232). This bidirectional link was used to receive the HK data (Telemetry, TM) and to upload command from ground (Tele-Command, TC). The RS232 output of the ground segment of Siren system was connected to a serial port of the GSE. After checking the mechanical and electrical integration of the NOSYCA system, the high speed data transfer was tested. The link worked properly, the telemetry data from the HK were correctly received for the whole duration of the test. On the other side, several commands were sent from the GSE to the HK which answered correctly. As third test the TCP-IP link between the GSE and the CPU (operated by Siren) was checked. The SSH connection with the CPU was established without any problem.

Once verified the correct operability of the three interfaces, all the sub-systems were turned off to test the sequence of the operations which should be performed, in flight, to power on, to configure the payload and to start the data taking.

The fully integrated system is shown in Figure 5.9. The final phase of the integration process was the performances tests to check the full instrument operate appropriately. These kind of test prepared the coming flight campaigns. Three kind of tests were done:

- trigger tests;
- calibration by a calibrated light source;
- time synchronisation between an external light source and the instrument internal trigger.

5.5.1 Trigger tests

The full instrument performance test consisted in simulating by an optical source the air shower development at speed-of-light in the atmosphere vertically, as the LED flasher is thought. The purpose is to check and tune the

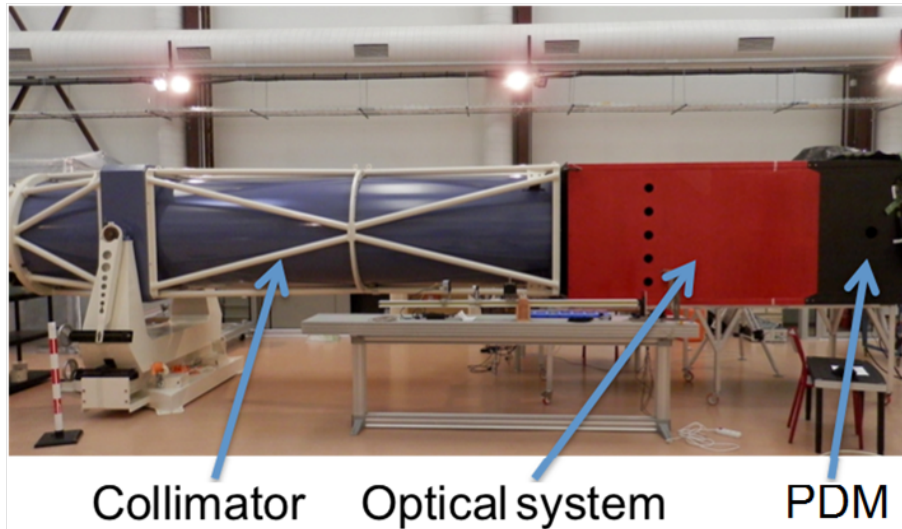


Figure 5.9: The fully integrated EUSO-Balloon instrument with the collimator used for the final test.

PDM-Board trigger algorithm. As shown of the figure 5.8, a LED flasher was used through the collimator to simulate a flash point at infinity. Several parameters could be tuned and tested: wavelengths, incidence angles, spot intensity, length of the pulses.

5.5.2 Calibration source tests

The purpose of these test was to validate the use of calibrated light sources on an helicopter during flight. Since detecting cosmic rays events is unlikely during a first short balloon flight (threshold $\sim 10^{18}$ eV), Xenon-flashes and LASER-induced events will provide a proof of principle and a way to calibrate threshold and sensitivity.

The basic principle of these test is to fly an helicopter equipped with two types of calibrated pulsed UV light sources. If the helicopter flies in field of view and fire a flash lamp, the light travels directly from lamp to detector and it is possible to make point test. Whereas, flying the helicopter outside field of view and shooting a UV pulsed laser across field of view, the light scatters out of the beam to the detector. In such a way it is possible to make track test, considering that a 5 mJ Laser simulates the light emission of a cosmic ray of about 100 eV.

The calibration source test were made using calibrated Light-emitting diodes (LEDs) operating at 355, 375 and 395 nm. Using the trigger generated by the CLK-Board, 128 data packets were read out of the PDM. The LED source was placed at the focus of the collimator so that its light filled the full diameter of the collimator. The LEDs were connected to a waveform

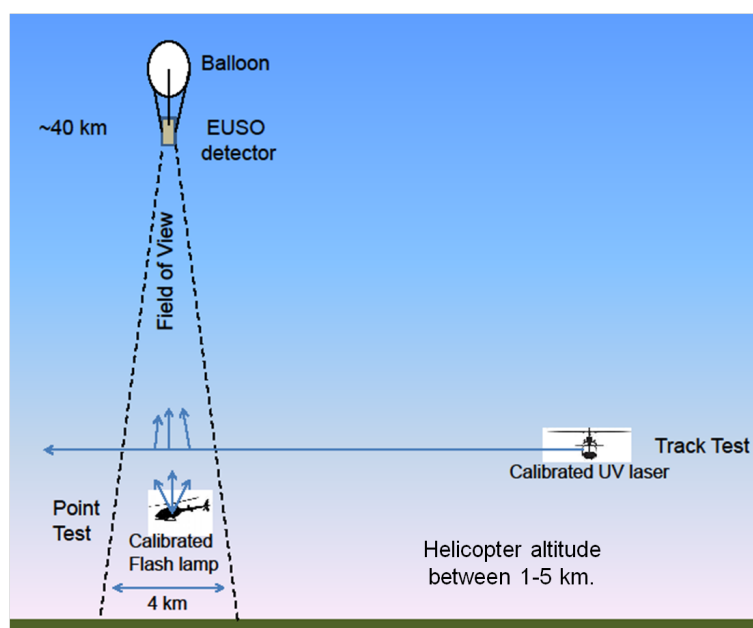


Figure 5.10: The basic principle of the “in flight” calibration with light sources on board an helicopter.

generator that was set to produce a square wave pulse with an adjustable amplitude and duration. The repetition period was set to $320 \mu\text{s}$ in order to have one pulse in each GTU.

These tests allowed to find LED settings for unsaturated signals in the PDM of EUSO BALLOON at 355, 375 and 395 nm.

To summarize, we performed end-to-end tests and we successfully managed to:

- operate the instrument from flight batteries with flight-plug ;
- measure the width of the PSF as a function of z (distance L3-PDM) for several wavelengths in order to find the best focal spot;
- map the PSF's at different wavelengths and incident angles;
- measure the overall (end-to-end) efficiency for 375 nm;
- test the system with pulses and pulse-intensities to match the dynamic range.

5.5.3 Test triggering using GPS signal

The LED settings found, together with the collimator throughput, were used to determine the brightness settings for the laser and the flashers on the helicopter flown under EUSO-BALLOON during its flight in Canada.

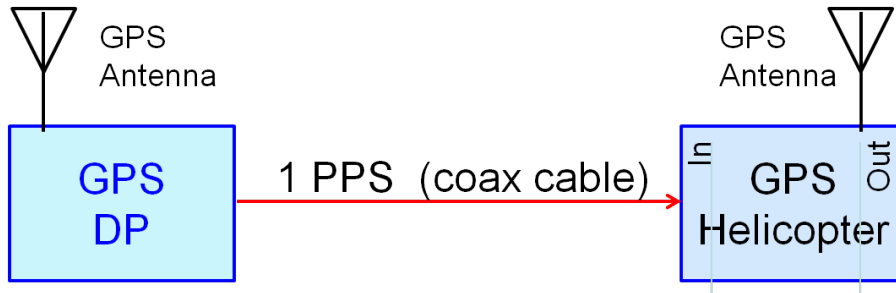


Figure 5.11: The 1PPS output signal of the DP GPS clock was time stamped by the helicopter GPS clock system.

The purpose of these tests was to detect the light from the calibrated sources by bypassing the PDM trigger algorithm. The calibrated source pulse has a different time/amplitude pulse structure so it is necessary to find another triggering mode. The DP, through the CLK-Board, provide an external trigger entry, thus it is possible to synchronise the light emission from the calibration source to the data acquisition on the base of a synchronised pulse. The GPS 1 Pulse Per Second (1PPS) signal was chosen to define a coincidence the DP readout window (128 GTU, thus $320 \mu\text{s}$), with the time position of the source pulse as shown on the Figure ???. The appropriate delay was determined during the AIT. In order to emit light by pulsing a LED synchronous to the helicopter GPS clock and recording that light with using the 1PPS signal of the DP GPS receiver as trigger the first step was to compare synchronization of helicopter GPS clock with balloon DP GPS clock. For this purpose, two GPS antennas were set up in the IRAP clean room and each was connected to a separate antenna placed outdoors. The 1PPS output signal of the DP GPS clock was sent out and time stamped by the helicopter GPS clock system (see Figure 5.11). The result of this first test are shown in the plot in Figure ???: the difference between DP GPS clock and Helicopter GPS clock is primarily due to the DP GPS Clock which uses a GPS engine optimized for position rather than timing. These tests proved that the Balloon GPS and Helicopter GPS clocks were synchronized with an $\text{RMS} < 0.5 \mu\text{s}$.

The following step was to use the 1PPS signal of the DP GPS clock as external trigger (through the CLK-Board) for the EUSO-Balloon instrument and simultaneously use the helicopter GPS clock to trigger an UV LED to produce one light pulse per second (see Figure ??). The pulse appeared in the 128 GTU readout window of EUSO-Balloon: the instrument successfully captured the flashes from an LED that was triggered independently by the helicopter GPS clock. These tests validated the external GPS trigger technique.

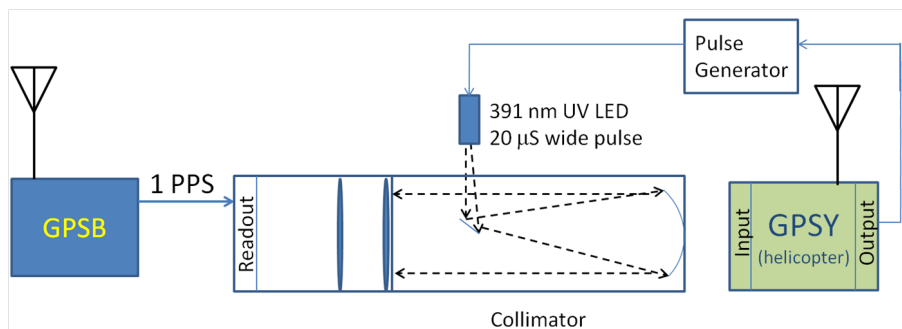


Figure 5.12: The 1PPS output signal of the DP GPS clock is used to trigger the data acquisition, while the light emission is triggered by the helicopter GPS clock. Since the two GPS clock are synchronized, the source pulse appears in the DP readout window.

5.6 Campaign simulation tests

The aim of this activity was to validate the good functioning of the instrument in autonomous conditions and to simulate the first flight campaign. In Figure ??

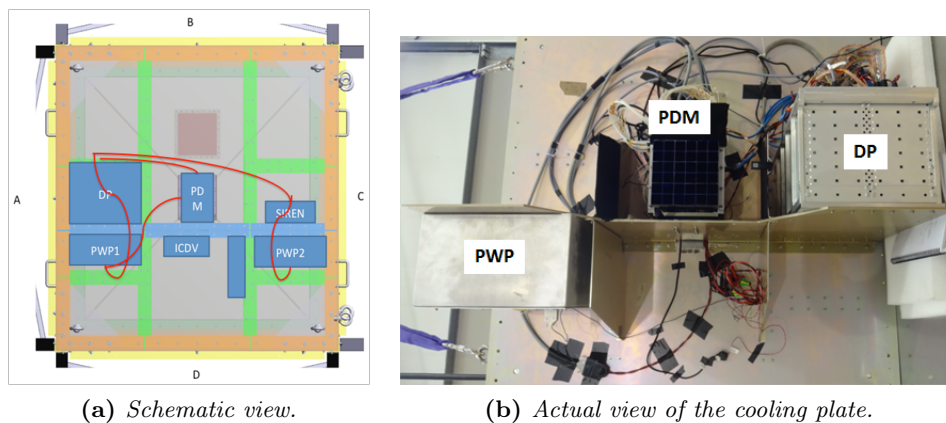


Figure 5.13: Top view of the full instrument showing the positioning of the various subsystems inside the instrument booth.

The main activities of this test were:

- switch the power supply of the instrument to battery;
- lift the gondola (to provide insulation from Earth);
- good health tests and signal acquisition, particularly the detectors signal, with and without WIFI NCU and NSO;
- thermal protections assembling;

- crash-pad implementation;
- ground segment implementation.

The EUSO-Balloon flight campaign will be briefly described in the next chapter.

Chapter 6

EUSO-Balloon launch campaign

The EUSO-Balloon launch campaign has been held in Timmins (Canada) in August 2014. I was one of the four member of the DP team who took part to the campaign. In this chapter I will summarize the main point of the preparation to the launch and of the flight.

The main tasks of the flight preparation were:

- Put the instrument in flight configuration
- Interface the DP with the CNES communication system
- Perform good health test to validate the acquisition chain
- Test of laser synchronization with the trigger from CLK-Board based on the 1PPS signal coming from GPS
- Development of flight data acquisition procedure

6.1 Ground Support Equipment and software

The Instrument can be controlled by two access points, a serial line toward HK microcontroller and an Ethernet port connected to the DP-CPU. During the flight, the serial line and the Ethernet ports of the instrument are connected to the CNES Siren module. Similar configurations could be adopted during final AIT activities. However, Siren module is not always available during AIT. This Siren functionality is simulated by a GSE computer having a serial port and Ethernet port (actually the GSE laptop running the GSE server). A private internal network must be set up to which any AIT team computer can connect to. The Ethernet port of the GSE server is connected to the internal network. The role of the GSE server is to receive or send data packets (event data, monitoring data, status data, or commands



Figure 6.1: The balloon a few moments before the launch.

data) from/to the appropriate port (its serial line for HK or Ethernet for the DP-CPU) to the instrument. The different computers from each AIT team are running one GSE client application in parallel, allowing them to receive the instrument data or to issue commands related to their own work. An additional computer, having two Ethernet boards. One of the Ethernet board must be connected to the internal private network and the second Ethernet board is connected to the external world internet. This computer is setup as a Gateway computer, running a proxy-server. Thus any computer connected to the internal network can access to the world Ethernet (for example to download code from institutes servers or flush data there). Moreover, people working outside the AIT place can work on the software developed for the AIT.

6.1.1 EUSO-Balloon instrument in AIT configuration

Figure ?? shows the Ethernet configuration during the AIT Phase, when Siren module is not available. The DP-CPU and GSE server CPU have two fixed IP addresses of the internal private network. The gateway is toward the external internet is provided by a poor resource NAS. This NAS will be very soon replaced by a Desktop computer with two Ethernet boards, with more memory and data flow performances. This Desktop computer has external disk of 2 TBytes. The GSE server or the Gateway computer can be used as the centralized detector control.

6.1.2 EUSO-Balloon instrument in flight configuration

During flight operation or when Siren module is available for AIT, the internal network must be duplicated because the GSE server is replaced by the Siren Module (Fig. 3.9). In the instrument the flight Siren module is connected to the Ethernet port of DP-CPU. The ground Siren module is connected to the private Ethernet network. The GSE server send or receive the Ethernet data to/from the instrument through its internal network via the two Siren module. Still the external access to the internet is provided by the gateway computer. The GSE server or the Gateway computer can be used as the centralized detector control.

6.2 The preparation of the flight

After the integration at IRAP in Toulouse, the EUSO-Balloon instrument was dismounted and sent to Timmins in containers. Once in Timmins the whole instrument had to be checked and mounted again. Before closing the gondola, the DP-PDM interface was checked and DP, PDM, SIREN and power pack box were fixed to the radiator mechanical structure. Then the electronics and the structure were putted under a black tent (with a NIST to estimate the light) to perform the first measurement with and without light. The DP-PDM tests showed that also the HVPS system was ok and the system was able to catch light. The DP-PDM were powered with the flight model battery powering and the interface with the CNES SIREN telemetry system was established and checked. During the assembling, the cable routing and the ground shielding were enhanced to improve the reliability of the system and to reduce the noise in the data taking.

The test of the DP GPS and the helicopter GPS taken in Toulouse (see 5.5.3) were repeated to synchronize accurately the two GPS.

6.3 The condition for the flight

During the days before the flight there were several meeting in order to decide the condition for the flight and to train the team. On August 26, the astronomical night in Timmins came around 10:30 p.m., but it had to be considered also the astronomical twilight, i.e. the time until the Sun reaches -18° under the horizon. In addition, since the EUSO-Balloon operated at an altitude of 40 km, the twilight was longer than on ground. For this reason, it was decided to switch on the High Voltages (HA) only after 11:00 p.m. in order to non risk to damage the MAPMT.

6.4 The flight

On August 25, 2014 at 0:53 UT EUSO-Balloon has been launched successfully from Timmins Stratospheric Balloon Base (lat 48.5° N) (Figure 7.3).

The instrument reached a float altitude of 38300 m at 23:43. The high-voltages had already been switched on at 22:50, at an altitude of 32 km, when the balloon was still on its ascent.

During more than five hours of operation, a total of about 8000 data-packets (i.e. roughly a million GTU) have been transmitted to the ground by telemetry. However, the largest part of the scientific harvest was on two redundant hard-drives in the gondola. The flight was terminated on 25.8 at 4:20 LT, about 100 km to the west of Timmins. Despite a descent path guaranteeing one of the driest landing zones along the flight track, EUSO-Balloon and the entire flight train splashed down in a tiny lake at 4:36 LT. An adventurous recovery was performed by a crew of trappers, EUSO members, and with the help of a helicopter. Thanks to its inborn design for waterlandings, the entire instrument was virtually undamaged, both lenses were intact, the electronics, IRCam, and particularly the RAID disks had not suffered any water damage and were fully operational.

The quick-look analysis based on the available telemetry data already bears high promises: the background light levels seem to be within the predicted range, the city-lights of Timmins have clearly been observed at the saturation level, and a laser-track has likely been detected as it crossed the field of view.

A variety of ground covers have been observed - including various types of soil and vegetation, water, urban and industrial areas, and clouds. Moreover, a helicopter carrying a laser and flashers for calibrating the instrument has been flying circles along the flight track for over two hours.

Altitude profile

Balloon track

Helicopter time

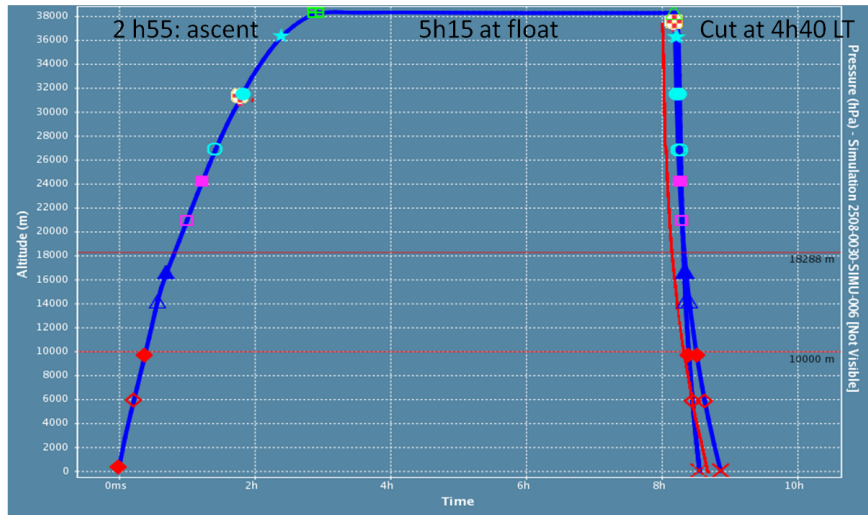


Figure 6.2: Altitude profile.

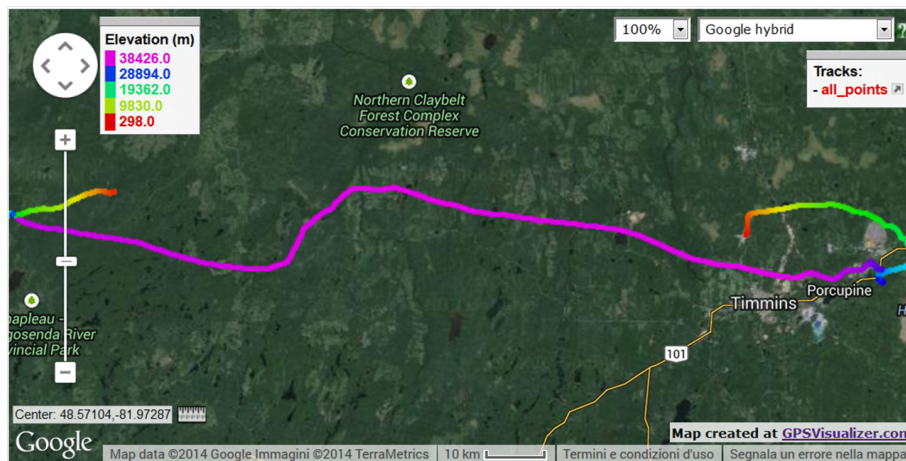


Figure 6.3: The balloon track.

Chapter 7

Data analysis and measurements

7.0.1 Jitter measurements

Before designing the flight model board for the CLK-Board of the EUSO pathfinders, I implemented the project on a Xilinx Virtex-5 FPGA [117] to verify if the system worked correctly. Communication interfaces, both with GPS receiver and with an FPGA programmed to perform some functions of a CCB, have been tested. More details on clock distribution network, synchronization with GPS system and event synchronization can be found in [?]. Here I want to focus on the jitter measurements taken.

The clock jitter reduces the timing budget available within a single clock period in any design [70]. A variation of the clock phase may introduce an additional uncertainty in a time measurement or may violate the specifications of other subsystems receiving the clock. Focusing on the jitter affecting the output clock driven by an FPGA pin gives us an insight on the FPGA internal jitter and allows us to compare different clock conditioning solutions.

I took jitter measurements to study the propagation of both clock signals within our FPGA. After measuring the jitter introduced by the passage in the 1st chip, the GTU clock was sent to another FPGA. In this way, I could study the variations of the GTU clock even after a 2nd level of electronics. I took these measurements at the output of a Virtex-5 device and of a Virtex-4 device, similar to the one used to implement CCBs.

In our testbench (fig. 7.1) some FPGA pins dedicated to clock IO are routed to SMA connectors. I used $50\ \Omega$ coaxial cables to clock the FPGA and to analyze its output. A clock generator [?] provided a very low jitter input clock to the board. A $50\ \Omega$ resistor was mounted on the board under the FPGA to properly terminate the clock line. The clock signal was also sent off-chip by means of a LVDS driver. LVDS differential drivers support high data rates and allow us to drive $50\ \Omega$ loads. One of the LVDS pin

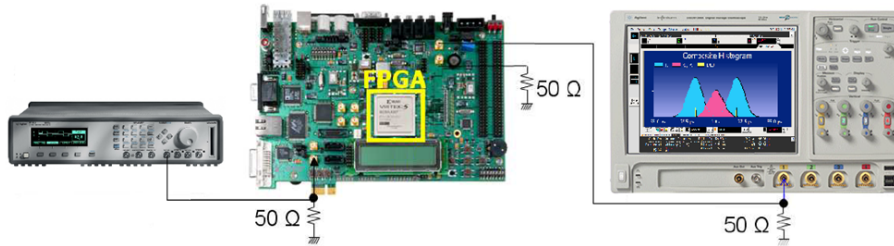


Figure 7.1: A pictorial block diagram of our test bench.

was connected to the test equipment, the other was terminated with a $50\ \Omega$ resistor, in order to keep the differential driver balanced.

I took jitter measurements in time domain with a real time oscilloscope [129] provided of a specific software for jitter analysis [110]. Our testbench permitted us to measure all the contributions to the jitter and, besides allowing to quickly assess the impact of jitter on the reliability of the system by estimating the peak-peak value of the TJ, it allowed us to identify the possible causes of jitter distinguishing between its components. An accurate evaluation of the periodic and the random contributions can be found in [132]. All the tests were performed on two boards and the results are nearly identical.

It is important to stress that the very low-jitter clock from the generator is not the actual signal given to the DUT. In fact, there is a noise pickup both at chip and at board levels. For instance, the actual signal at the DUT input includes the noise due to the power supply on the FPGA input buffer and possible crosstalk on the routing. The logic implemented in the chip produces noise due to its switching activity and the clock signals pick up additional noise when they exit the FPGA through the output buffer. The jitter measurements performed include also the contribution of the DUT and the surrounding environment (the benchmark design, the FPGA and the board).

At first I studied the jitter on the 40 MHz clock at the output of the clock generator, then we sent this signal to the CLK-Board in order to estimate the jitter introduced by the passage in the FPGA. The TJ at the output of the FPGA is bigger than the jitter at the input of the chip, both DCD and PJ rise. RJ and PJ histogram is still gaussian, this means that RJ is dominant. Looking at the spectrum of the jitter, there is an increase of the peaks due the PJ.

Once studied the jitter introduced in the 40 MHz clock by the passage in the FPGA, we measured jitter of the GTU clock at the output of the CLK-Board. The GTU clock, with a duty cycle of 98%, is produced within the CLK-Board. This signal is then routed through a BUFG on the clock signals dedicated path, drives a part of the logic and is sent to CCBs, therefore, it is very important to know its jitter. Moreover, even if this signal has

a period of $2.5 \mu\text{s}$, it is necessary that the 50 ns interval in which the signal is low is preserved and transmitted correctly to the last level of electronics of the FS. Figure 7.2 shows the screen of the oscilloscope with the GTU clock

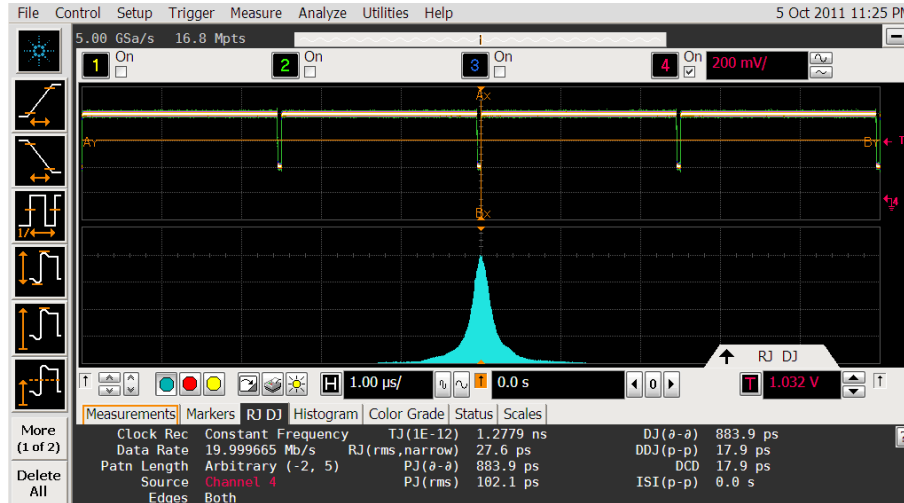


Figure 7.2: Signal and TIE histogram for the GTU clock at the output the CLK-Board.

and the histogram of TIE. After studying the jitter of both clock signals at the output of the CLK-Board, we measured the jitter of the GTU clock at the output of a 2nd level of FPGA. Using SMA connectors and coaxial cables, the differential GTU clock has been sent from the CLK-Board to the 2nd FPGA. We chose to transmit a differential clock in order to corrupt it as little as possible. At the output of the 2nd chip all the values of the jitter components measured are of the same order of magnitude which they had at the output of the 1st FPGA. Our measurements are summarized in the following table:

	40 MHz	40 MHz 1 st	GTU 1 st	GTU 2 nd
TJ	114.28 ps	211.65 ps	1.2812 ns	1.5143 ns
RJ(rms)	4.91 ps	6.30 ps	28.1 ps	51.4 ps
PJ(dd)	12.98 ps	19.44 ps	880.0 ps	741.0 ps
PJ(rms)	3.36 ps	5.55 ps	104.8 ps	128.8 ps
DJ(dd)	44.22 ps	121.81 ps	880.0 ps	780.9 ps
DCD	32.55 ps	104.92 ps	17.9 ps	58.7 ps

In both cases, the dominant component is represented by PJ, in fact, observing the TIE histogram and the composite jitter histogram, we can notice that the TJ PDF has not the form of a Dirac double-delta, because the PDF of RJ and PJ is dominant.

We took the same measurements also using a Virtex-4 as a 2nd board, jitter values are not very different from those measured at the output of Virtex-5. In both cases, jitter does not increase significantly after a 2nd level



Figure 7.3: The data acquisition mode used during the flight.

of FPGA and it is tolerable for our system.

7.1 Data analysis in progress

The goals:

- Instrument performance:
 - flasher/laser track reconstruction =, calibration =, energy in event global efficiency;
 - PSF.
- Atmospheric conditions:
 - IR-Camera for cloud height and temperature;
 - model verifications.
- UV background:
 - for various ground covers and clouds;
 - spatial and temporal variability.
- Trigger: a posterior trigger test-algorithm.
- Technology: improving the hardware for future flights (optics, PDM, DP, gondola).

7.1.1 Data Processor performance

Continuous data taking Some minor problems not related to CPU

Continuous data taking The number of fired pixels reflects the amount of light in the FoV Noise peaks are related to changes in DAQ and gain

The number of PMT OFF changes in every run (related to COMMIT error?) Step of 6 PMT corresponding to one ASIC board

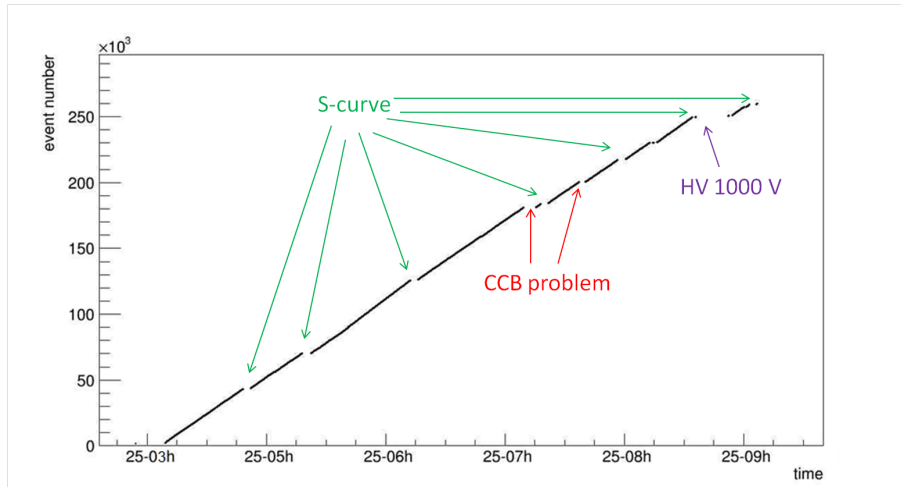


Figure 7.4: Number of acquired events in function of time (UTC).

7.2 Live and dead time measurement

$\tau_{\text{Live time}} = 37.86$ ms time needed from CPU to send a new trigger signal

$\tau_{\text{Trigger rate}} = 18$ Hz

$\tau_{\text{Dead time}} = 17.25$ ms comparable with the data transfer time via SPW link (340kB @ 200 Mbits/s)

Time at float = 5h15 minutes = 18900 s N. Events = 256000 Event duration = 128 GTU = 320 320 μ s

T acquisition = N. events \cdot event duration 80 s 0,4% Time@float

Tdead+LiveTOT = N. Events \cdot [$\tau_{\text{Dead time}}$ + $\tau_{\text{Live time}}$] = 14080 s

T S-curves = 7 \cdot 3 minutes \sim 1200 s

Total data taking time = T acquisition + Tdead+LiveTOT + TS-curves = 15300 s

Total data taking time / Timeatfloat = 81%

The remaining 19% was due to configuration procedure at the start of every run and to problems related to communication with PDM or HV drop.

Band structure due to the data transfer: after a short run the CPU has to transfer the data on ground, so it is slower.

In the acquisition mode the sum of dead time and live time is exactly 50 ms (20 Hz frequency).

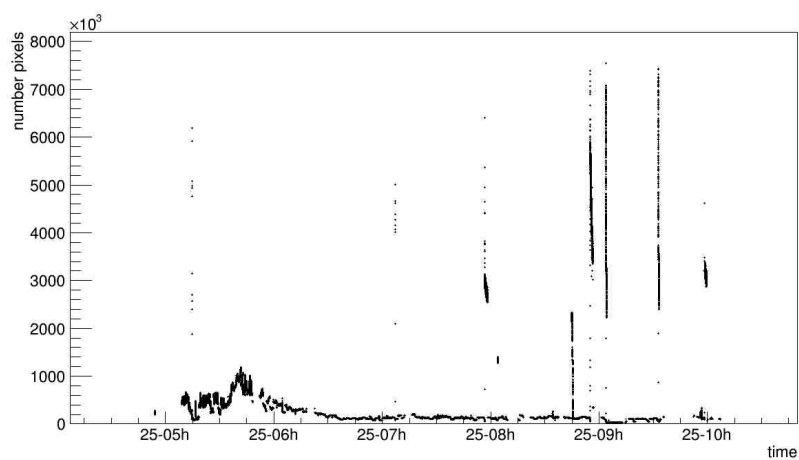


Figure 7.5: Number of pixels in function of time (UTC).

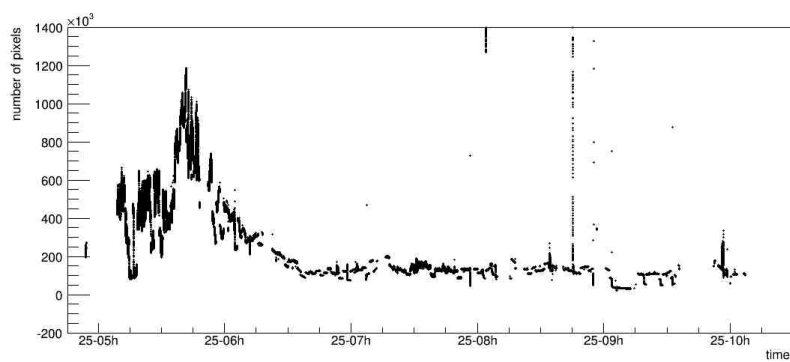


Figure 7.6: Number of pixels in function of time (UTC), zoom to underline noise peaks due to changes in DAQ and gain .

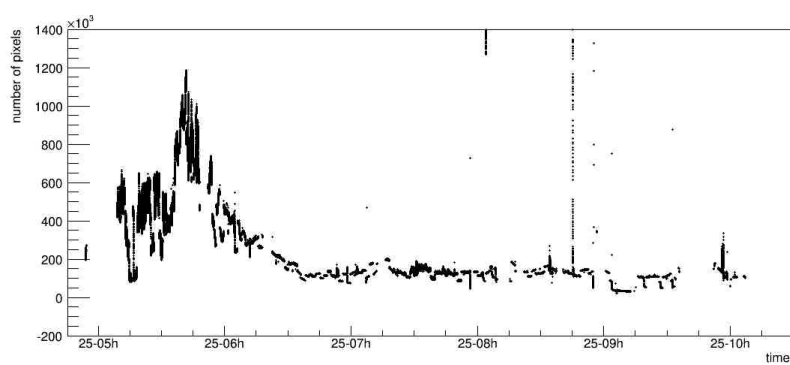


Figure 7.7: Number of PMT off in function of time (UTC), zoom to underline noise peaks due to changes in DAQ and gain .

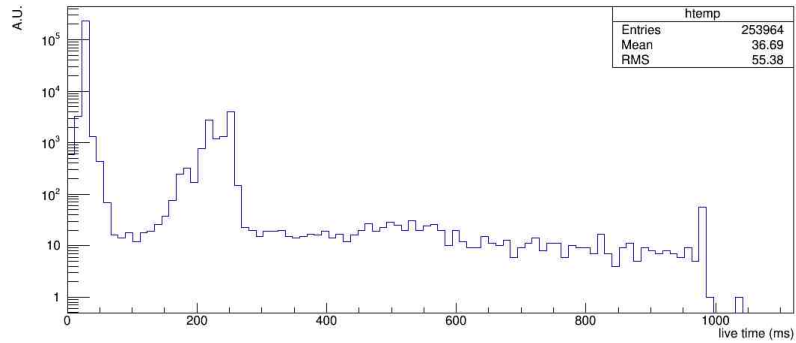


Figure 7.8: .

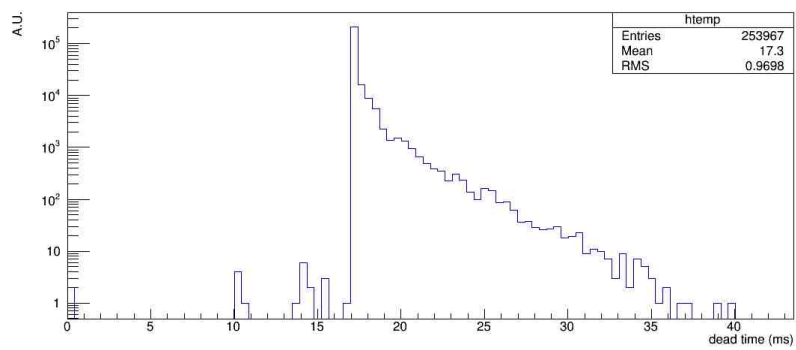


Figure 7.9: Dead time distribution.

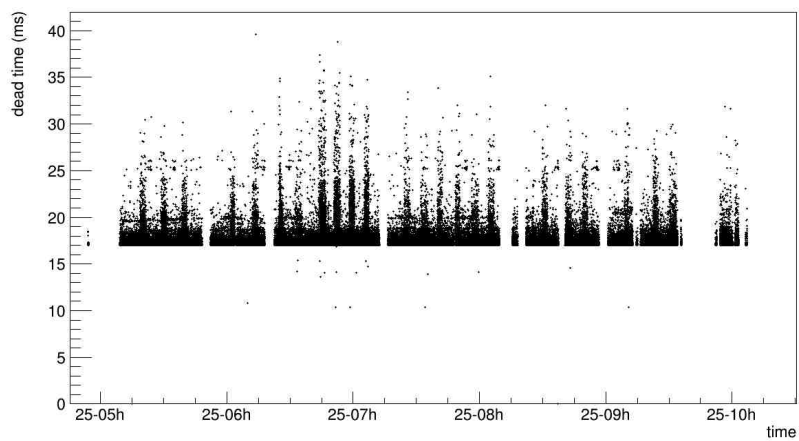


Figure 7.10: Dead time in function of time (UTC).

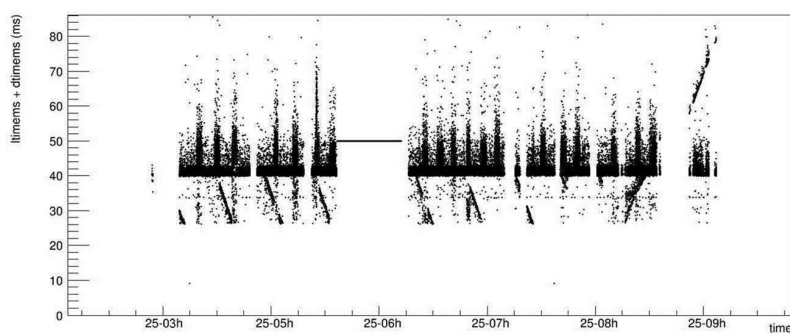


Figure 7.11: Dead time + live time in function of time (UTC).

Conclusions and perspectives

In my Ph.D. thesis work I developed the Time and Synchronization System for the EUSO-Balloon and EUSO-TA pathfinders of the JEM-EUSO experiment.

I carried on my work within the framework of the JEM-EUSO international collaboration, having the possibility to take part to the integration of the instrument and to the first flight campaign of the EUSO-Balloon.

The Time and Synchronization System is composed of the CLK-Board and a GPS receiver and represents a complete subsystem of the Data Processor (DP) of the EUSO pathfinder, which is in charge of the data acquisition management.

My Ph.D. work started with the design of the firmware for FPGA of the CLK-Board. This board has to:

- generate and distribute clocks and time synchronization signal to all the FS electronics;
- provide the time synchronization of the event and measure live-time, dead-time and arrival time of particles on a scale of few μs ;
- interface with the GPS system in order to tag every event with an absolute time label;
- manage trigger signals: it receive 2nd level trigger signals and forwards test trigger signals to FS electronics;

I wrote the HDL description of the system, then I realized a prototype and I developed a test benches in order to verify the logic description of the project. The test benches stimulates the system by emulating the behavior of external elements, which it will be interfaced to once it will be in real operation: the other components of the DP. This methodology allowed me to verify the successful operation of the system permitted me to quickly develop and debug the firmware to be executed by the FPGA.

Concerning the GPS system, after selecting and testing several commercial GPS receiver, we designed PCBs to integrate GPS receivers and provide them all the connections to others DP components. I went to CNES to test

the chosen GPS receiver in an high altitude simulator. In fact, for the EUSO-Balloon pathfinder, we used a different GPS receiver and an industrial grade FPGA able to work at high altitude.

The Time and Synchronization System has been successfully integrated with the other components of the DP during the DP integration held in Naples in 2013. I participated to the testing and the development of procedures in collaboration with the other members of the team to optimize the management of the trigger and synchronization signals.

During the second year of my Ph.D. program, I have been involved in the integration of the DP with the board which generates the first level trigger and, through this board, to the FE electronics and the MAPMT at APC, in Paris. We built and tested the whole acquisition chain, from MAPMT to CPU and I had the possibility to make a first preliminary analysis of TS system data to check his proper functionality. Then the whole system was tested in Thermo-vacuum chamber at CNES, finally I was involved in the full integration tests (from optics to DP) at IRAP in Toulouse.

In August 2014, I was one of the four members of the DP team who participate the first launch of EUSO-Balloon from the Canadian Space Agency base in Timmins, where I had also to implement an internal trigger to synchronize data acquisition and helicopter light during flight. The proper functioning of the system during flight is the successful completion of my work.

The analysis of data taken during the flight is in progress, the system has been restored after the flight and post-flight calibration in progress at APC in Paris.

At the moment, I am involved in the development of the Data Processor for the next missions:

- Long duration Balloon flight is a joint project of the French space agency, Centre National d'Études Spatiales (CNES), with NASA. The main objective of the long duration EUSO-Balloon flight will be to detect the first Extensive Air Shower from an altitude of 40 km.
- Mini-EUSO is a special project to place a very small version of the JEM-EUSO detector inside the ISS, observing the atmosphere through an UV transparent window. One of the important issues of Mini-EUSO is the significant increase of the technological maturity levels required for several innovations necessary for JEM-EUSO, developing several components upstream in this small demonstrator, including having the opportunity to test them in space. The second issue of this demonstrator will be its ability to produce unpublished data, paving the way for a family of large-scale projects.

Bibliography

- [1] V. Hess, “Penetrating Radiation in Seven Free Ballon Flights”, *Physik. Zeitschr.* 13, pp. 1084-1091, 1912.
- [2] P. Auger, P. Ehrenfest, R. Maze, J. Daudin, and R. A. Fréon, “Extensive cosmic-ray showers”, *Rev. Mod. Phys.* 11, pp. 288-291, July 1939.
- [3] J. Linsley, “Evidence for a primary cosmic-ray particle with energy 10^{20} eV”, *Physical Review Letter* 10, pp. 146-148, Feb. 1963.
- [4] J. Blumer, R. Engel, J. R. Horandel, “Cosmic rays from the knee to the highest energies”, *Prog.Part.Nucl.Phys.* 63, pp. 293-338, DOI: 10.1016/j.pnpnp.2009.05.002. arXiv:0904.0725 [astro-ph.HE], 2009.
- [5] K. Kotera, A. V. Olinto, “The Astrophysics of Ultrahigh-Energy Cosmic Rays”, *Annu. Rev. Astron. Astrophys.*, pp. 119-153, DOI: 10.1146/annurev-astro-081710-102620. arXiv:1101.4256 [astro-ph.HE], 2011.
- [6] T. K. Gaisser, T. Stanev, “High-energy cosmic rays”, *Nuclear Physics A 777.0*, Special Issue on Nuclear Astrophysics, pp. 98-110. issn: 0375-9474, DOI:10.1016/j.nuclphysa.2005.01.024 , 2006.
- [7] F. W. Stecker, M. A. Malkan, S. T. Scully, “Intergalactic Photon Spectra from the Far-IR to the UV Lyman Limit for $0 < z < 6$ and the Optical Depth of the Universe to High-Energy Gamma Rays”, *ApJ* 648, pp. 774-783, DOI: 10.1086/506188, eprint: arXiv : astro-ph/0510449, 2006.
- [8] The Pierre Auger Collaboration, “Measurement of the energy spectrum of cosmic rays above 10^{18} eV using the Pierre Auger Observatory”, *Phys. Lett. B* 685, 2010.
- [9] P. Sokolsky for the HiRes Collaboration, “Final Results from the High Resolution Fly’s Eye (HiRes) Experiment”, XVI International Symposium on Very High Energy Cosmic Ray Interactions ISVHECRI 2010, 2010.

-
- [10] L. Cazon and The Pierre Auger Collaboration. “Studying the nuclear mass composition of Ultra-High Energy Cosmic Rays with the Pierre Auger Observatory”, *Journal of Physics: Conference Series* 375.5, p. 052003, url: <http://stacks.iop.org/1742-6596/375/i=5/a=052003>, 2012.
- [11] Y. Tameda, “HiRes and TA Composition measurements”, *European Physical Journal Web of Conference*, Vol. 53, *European Physical Journal Web of Conferences*, p. 4005, DOI: 10.1051/epjconf/20135304005, 2013.
- [12] E. Barcikowski et al., “Mass Composition Working Group Report at UHECR-2012”, *EPJ Web Conf.* 53, p. 01006, DOI: 10.1051/epjconf/20135301006, arXiv:1306.4430 [astro-ph.HE], 2013.
- [13] E. Fermi, “On the Origin of the Cosmic Radiation”, *Phys.Rev.* 75, pp. 1169-1174. doi: 10.1103/PhysRev.75.1169, 1949.
- [14] A. R. Bell. “The Acceleration of cosmic rays in shock fronts”, *Mon.Not.Roy.Astron.Soc.* 182, pp. 147-156, 1978.
- [15] R. D. Blandford and J. P. Ostriker. “Particle acceleration by astrophysical shocks”, *ApJL* 221, pp. L29-L32. doi: 10.1086/182658, 1978.
- [16] S.L. Shapiro, S.A. Teukolsky. “Black holes, white dwarfs, and neutron stars: The physics of compact objects”, *John Wiley and Son. Inc.*, 1983.
- [17] V. Berezhinsky, M. Kachelriess, A. Vilenkin. “Ultrahigh-energy cosmic rays without GZK cutoff”, *Phys.Rev.Lett.* 79, pp. 4302-4305, doi: 10.1103/PhysRevLett.79.4302. arXiv:astro-ph/9708217 [astro-ph], 1997.
- [18] KASCADE-Grande Collaboration, “The spectrum of high-energy cosmic rays measured with KASCADE-Grande”, *Astroparticle Physics*, vol. 36, pp. 183-194, 2012.
- [19] A. Codino, “The Naked Iron Knee, its Necessity and Empirical Evidence”, *INFN Report/TC-09/05*, July 2009.
- [20] K. Murase, S. Inoue, S. Nagataki, “Cosmic Rays above the Second Knee from Clusters of Galaxies and Associated High-Energy Neutrino Emission”, *The Astrophysical Journal*, 689: L105-L108, December 2008.
- [21] K. Kampert, “Ultra High-Energy Cosmic Ray Observations”, *J. Phys. Conference*, 2008. <http://arxiv.org/abs/0801.1986v1>

-
- [22] N. Hayashida et al., AGASA Collaboration, “The Anisotropy of Cosmic Ray Arrival Direction around 10^{18} eV”, *Astropart. Phys.* 10, arXiv:astro-ph/9906056v1, 1999.
- [23] Pierre Auger Collaboration, “Correlation of the Highest-Energy Cosmic Rays with Nearby Extragalactic Objects”, *Science* 318, 938, 2007.
- [24] Pierre Auger Collaboration, “Update on the correlation of the highest energy cosmic rays with nearby extragalactic matter”, arXiv:1009.1855v2 [astro-ph.HE], 2010.
- [25] A.M. Hillas, “The Origin of Ultra-High-Energy Cosmic Rays”, *Annual review of astronomy and astrophysics*, Volume 22, p. 425-444, 1984.
- [26] Thomas K. Gaisser, “Cosmic Rays and Particle Physics”, Cambridge University Press, 1990.
- [27] A.A. Penzias, R.W. Wilson, “A Measurement of Excess Antenna Temperature at 4080 Mc/s.”, *Astrophysical Journal*, vol. 142, p.419-421, 1965.
- [28] K. Griesen, “End to the Cosmic-Ray Spectrum?”, *Phys. Rev. Lett.* 16, 748 (1966).
- [29] G.T. Zatsepin and V.A. Kuzmin, “Upper limit of the spectrum of cosmic rays”, *JETP. Lett.* 4, 78, 1966.
- [30] Heitler W, “Showers Produced by the Penetrating Cosmic Radiation”, *Proc. R. Soc. A* 166 529, 1938.
- [31] R. Aloisio, V. Berezhinsky, A. Gazizov, “Transition from galactic to extragalactic cosmic rays”, *Astroparticle Physics*, vol. 39-40, pp. 129-143, 2012.
- [32] D. De Marco and T. Stanev, “On the shape of the ultrahigh energy cosmic ray spectrum”, *Phys. Rev. D*, 72:081301, 2005.
- [33] , V. Berezhinsky , A. Gazizov , S. Grigorieva, “On astrophysical solution to ultrahigh energy cosmic rays”, *Phys. Rev. D*74, 2006.
- [34] D. Allard, E. Parizot and A.V. Olinto, “Signatures of the extragalactic cosmic-ray source composition from spectrum and shower depth measurements”, arXiv: astro-ph/0703633, 2007.
- [35] D. Allard, E. Parizot and A.V. Olinto, “On the transition from galactic to extragalactic cosmic-rays: Spectral and composition features from two opposite scenarios”, *Astropart. Phys.*, 27:61, 2007.

- [36] X. Bertou, P. Billoir, S. Dagoret-Campagne. “LPM effect and pair production in the geomagnetic field: a signature of ultra-high energy photons in the Pierre Auger Observatory”, *Astroparticle Physics* 14.2, pp. 121-130. issn: 0927-6505. doi: [http://dx.doi.org/10.1016/S0927-6505\(00\)00112-2](http://dx.doi.org/10.1016/S0927-6505(00)00112-2). url: <http://www.sciencedirect.com/science/article/pii/S0927650500001122>, 2000.
- [37] J. Matthews, “A Heitler model of extensive air showers”, *Astropart.Phys.* 22, pp. 387-397. doi: 10.1016/j.astropartphys.2004.09.003, 2005.
- [38] B.M. Connolly, S.Y. BenZvi, C.B. Finley, A.C. O’Neill, S. Westerhoff, “Comparison of the Ultra-High Energy Cosmic Ray Flux Observed by AGASA, HiRes and Auger”, arXiv:astro-ph/0606343v2, February 2008.
- [39] K. Shinozaki, “AGASA Results”, October 2004.
- [40] Pierre Auger Collaboration, “The Pierre Auger Observatory I: The Cosmic Ray Energy Spectrum and Related Measurements”, 32ND INTERNATIONAL COSMIC RAY CONFERENCE, BEIJING 2011.
- [41] D. J. Bird et al., “The cosmic-ray energy spectrum observed by the Fly’s Eye”, *Astrophysical Journal*, vol. 424, pp. 491-502, March 1994.
- [42] Telescope Array Collaboration, “Hybrid Measurement of the Telescope Array Experiment”, PROCEEDINGS OF THE 31st ICRC, Lodz, 2009.
- [43] P. Sokolsky for the HiRes Collaboration, “Final Results from the High Resolution Fly’s Eye (HiRes) Experiment”, XVI International Symposium on Very High Energy Cosmic Ray Interactions ISVHECRI 2010, 2010.
- [44] P. Doll et al., “Muon tracking detector for the air shower experiment KASCADE”, *Nucl.Instrum.Meth.* A488, pp. 517-535. doi: 10.1016/S0168-9002(02)00560-0.
- [45] R. Adinolfi Falcone et al. “The hadron calorimeter of EAS-TOP: Operation, calibration and resolution”, *Nucl.Instrum.Meth.* A420, pp. 117-131. doi: 10.1016/S0168-9002(98)01129-2, 1999.
- [46] Ivanov Anatoly. “The Yakutsk array experiment: Main results and future directions”, *EPJ Web Conf.* 53, p. 04003. doi: 10.1051/epj-conf/20135304003, 2013.

- [47] T. Antoni et al. “KASCADE measurements of energy spectra for elemental groups of cosmic rays: Results and open problems”, *Astropart.Phys.* 24, pp. 1-25. doi: 10.1016/j.astropartphys.2005.04.001. arXiv:astro-ph/0505413 [astro-ph], 2005.
- [48] W.D. Apel et al. “Kneelike structure in the spectrum of the heavy component of cosmic rays observed with KASCADE-Grande”, *Phys.Rev.Lett.* 107, p. 171104. doi: 10.1103/PhysRevLett.107.171104. arXiv:1107.5885 [astro-ph.HE], 2011.
- [49] Pierre Auger and Yakutsk Collaborations (Allen, J. et al.), “Air Shower Simulation and Hadronic Interactions”, *EPJ Web Conf.* 53, 01007 arXiv:1306.6090 [astro-ph.HE] , 2013.
- [50] A.M. Hillas, “Evolution of ground-based gamma-ray astronomy from the early days to the Cherenkov Telescope Arrays”, *Astroparticle Physics*, vol.43, pp. 19-43, 2013.
- [51] S. Funk, “The status of gamma-ray astronomy”, arXiv:1204.4529v1, 2012.
- [52] Y. Tameda for the Telescope Array and HiRes Collaboration, “HiRes and TA Composition measurements”, *EPJ Web of Conferences* 53, 04005, 2013.
- [53] M. Fukushima, “Measurement of ultra-high energy cosmic rays: An experimental summary and prospects”, *EPJ Web of Conferences* 53, 02002, 2013.
- [54] M. Nagano, A. A. Watson, “Observations and implications of the ultrahigh-energy cosmic rays”, *Reviews of Modern Physics*, Vol. 72, No. 3, July 2000.
- [55] G. Medina-Tanco for the JEM-EUSO Collaboration, “Science objectives of the JEM-EUSO mission”, ID0956, ICRC 2011.
- [56] A. Zuccaro for the JEM-EUSO Collaboration, “The JEM-EUSO optics design”, ID0852, ICRC 2011.
- [57] Y. Kawasaki for the JEM-EUSO Collaboration, “The Focal Surface of the JEM-EUSO Instrument”, ID0472, ICRC 2011.
- [58] M. Casolino for the JEM-EUSO Collaboration, “Data Acquisition System of the JEM-EUSO project”, ID1219, ICRC 2011
- [59] J. Bayer for the JEM-EUSO Collaboration, “The Cluster Control Board of the JEM-EUSO mission”, ID0836, ICRC 2011.

-
- [60] A. Neronov for the JEM-EUSO Collaboration, “Atmospheric Monitoring System of JEM-EUSO”, ID0301, ICRC 2011.
- [61] G. Medina-Tanco for the JEM-EUSO Collaboration, “The Housekeeping subsystem of the JEM-EUSO instrument”, ID0961, ICRC 2011.
- [62] JEM-EUSO Collaboration, “JEM-EUSO Report on the Phase A Study 2010”, JEUSO-110025-01-E-TR-ZZZ, 2010.
- [63] J. H. Adams et al, “Summary Report of JEM-EUSO Workshop at KICP in Chicago”, arXiv:1203.3451 .
- [64] S. Palomares-Ruiz, A. Irimia and T. J. Weiler, Phys. Rev. D 73, 083003 (2006) [astro-ph/0512231].
- [65] A. D. Supanitsky et al. (JEM-EUSO Collaboration) Proc. 33rd ICRC, 2013 (id 461);
- [66] A. Guzman et al. (JEM-EUSO Collaboration) Proc. 33rd ICRC, 2013 (id 0533)
- [67] P. Bhattacharjee and G. Sigl, Phys. Rept. 327, 109 (2000).
- [68] M. Bertaina et al. [JEM-EUSO Collaboration] Proc. 33rd ICRC, 2013 (id 272)
- [69] J. M. Rabaey, A. Chandrakasan, B. Nikolic “Digital Integrated Circuits - A Design Perspective (2nd Ed)”, Prentice Hall, 2003.
- [70] S. Unger and C.-J. Tan, “Optimal clocking schemes for high speed digital systems”, IEEE Transactions on Computers, Vol. C-35, Oct. 1986, pp. 880-895.
- [71] E. G. Friedman, “Clock Distribution Networks in Synchronous Digital Integrated Circuits”, Proceedings of the IEEE, Vol. 89, N^o 5, May 2001.
- [72] J. F. Wakerly, “Digital Design Principles and Practices, Third Edition”, Prentice Hall, ISBN: 0-13-769191-2, 1999.
- [73] D. F. Wann, M. A. Franklin, “Asynchronous and Clocked Control Structures for VLSI Based Interconnection Networks”, IEEE Transactions on Computers, Vol. C-32 Issue 3, March 1983.
- [74] M. Afghahi, C. Svensson, “Performance of Synchronous and Asynchronous Schemes for VLSI Systems”, IEEE Transactions on Computers archive Volume 41 Issue 7, July 1992.
- [75] Xilinx, “Virtex-5 FPGA User Guide, UG190” [Online]. Available: www.xilinx.com/support/documentation/user_guides/ug190.pdf.

- [76] Bell Communications Research, Inc (Bellcore), "Synchronous Optical Network (SONET) Transport Systems: Common Generic Criteria, TR-253-CORE", Issue 2, Rev No. 1, December 1997
- [77] National Committee for Information Technology Standardization (NCITS), Working Draft for "Fiber Channel-Methodologies for Jitter Specification (MJS)", Rev 7, 1999.
- [78] ITU-T Recommendation G.810 (08/96) "Definitions and Terminology for Synchronization Networks" ITU, 1996.
- [79] Tektronix, "Understanding and Characterizing Timing Jitter", Tektronix Inc., Application Note, 2003 [Online], Available: <http://www.tektronix.com/jitter>
- [80] J. Hancock, S. Draving, "Jitter - Understanding it, Measuring It, Eliminating It - Part 2: Jitter Measurements", High Frequency Electronics, May 2004.
- [81] B. N. Kearsey, R. W. McLintock, "Jitter in digital telecommunication networks", The Radio and Electronic Engineer, Vol. 54, No. 2, pp. 70-78, February 1984.
- [82] M. Muller, R. Stephens, R. McHugh, "Total Jitter Measurement at Low Probability Levels, Using Optimized BERT Scan Method, White Paper", Agilent Technologies, DesignCon 2005, [Online]. Available: <http://cp.literature.agilent.com/litweb/pdf/5989-2933EN.pdf>.
- [83] Agilent Technologies, "Jitter Analysis Techniques for High Data Rates, Application Note 1432", Agilent Technologies, 2008 [Online]. Available: <http://cp.literature.agilent.com/litweb/pdf/5988-8425EN.pdf>.
- [84] R. Darapu, C.W. Zhang, L. Forbes, "Analysis of Jitter in Clock Distribution Networks", 0-7803-8369-9/04/\$20.00 ©2004 IEEE.
- [85] R. Poore, "Phase noise and jitter", Agilent EEsof EDA, 17 May, 2001.
- [86] SiTime Corporation, "Clock Jitter and Measurement", SiT-AN10007 Rev. 1.0, 6 February 2009.
- [87] MAXIM, "An Introduction to Jitter in Communications Systems", Application Note 1916, www.maxim-ic.com/an1916
- [88] M. Li, "Jitter, noise, and signal integrity at high-speed", Prentice Hall, ISBN: 0132429616, 2007.
- [89] LeCroy, "Advance measurements - Jitter and Jitter Breakdown Analysis"

- [90] V. S. Reinhardt, "A Review of Time Jitter and Digital Systems", IEEE International Frequency Control Symposium and Precise Time and Time Interval (PTTI) Systems and Applications Meeting, Vancouver, BC, Canada, August, 2005.
- [91] J. Hancock, "Jitter - Understanding it, Measuring It, Eliminating It - Part 1: Jitter Fundamentals", High Frequency Electronics, April 2004.
- [92] J. Hancock, "Jitter - Understanding it, Measuring It, Eliminating It - Part 3: Causes of Jitter", High Frequency Electronics, June 2004.
- [93] H. Johnson, "Jitter Effects in Modern System Designs", Xilinx Tech On-Line, 2005. [Online]. Available: http://www.xilinx.com/products/silicon_solutions/fpgas/virtex/virtex4/advantages/Jitter_Effects.pdf.
- [94] Agilent, "Measuring Jitter in Digital Systems, Application Note 1448-1", June 1, 2003. <http://cp.literature.agilent.com/litweb/pdf/5988-9109EN.pdf>.
- [95] M. Li, "A New Jitter Classification Method Based on Statistical, Physical, and Spectroscopic Mechanisms", IEC/DesignCon 2009.
- [96] M. Li, J. Wilstrup, R. Jessen, and D. Petrich, "A New Method for Jitter Decomposition Through Its Distribution Tail Fitting", IEEE International Test Conference, pp788-794, 1999.
- [97] L.D.Landau, E.M.Lifshitz, "Statistical Physics, Part 2, 3rd ed.", Pergamon Press, 1980.
- [98] J. Solorzano, "Jitter Basics, Part 2", Micrel Inc., Feb. 2009.
- [99] N. Radhakrishnan, B. Achkir, J. Fan, J. L. Drewniak, "Stressed Jitter Analysis for Physical Link Characterization", Electromagnetic Compatibility, 2010. IEEE International Symposium, pp. 568-572, 25-30, 2010.
- [100] Wavecrest "Jitter Fundamentals- The Reference Standard for Signal Integrity Analysis", Wavecrest Corporation. SMPB-00019 Rev. 1. [Online]. Available: www.wavecrestkk.co.jp/jittfun_hires_sngls.pdf
- [101] Maxim "Jitter in Digital Communication Systems, Part 1", Maxim Integrated Products, Application Note HFAN-04.0.3, Rev1, April 2008 [Online], Available: <http://pdfserv.maxim-ic.com/en/an/AN794.pdf>
- [102] A. Kuo, R. Rosales, T. Farahmand, S. Tabatabaei, A. Ivanov, "Crosstalk Bounded Uncorrelated Jitter (BUJ) for High-Speed Interconnects", IEEE Transaction on Instrumentation and Measurement, Vol. 54, N° 5, OCTOBER 2005.

- [103] Wavecrest, “An Introduction to Jitter Analysis”, Wavecrest Corporation, 2001.
- [104] J. Hancock, “Jitter Analysis with Real-Time Jitter Analysis, Application Note 1448-2”, 2003 [Online]. Available: <http://cp.literature.agilent.com/litweb/pdf/5988-8425EN.pdf>
- [105] M. Marcu, S. Durbha, S. Gupta, “Duty-Cycle Distortion and Specifications for Jitter Test-Signal Generation”, IEEE, 978-1-4244-1699-8/08/\$25.00, 2008.
- [106] M. Li, J. B. Wilstrup, “On the Accuracy of Jitter Separation From Bit Error Rate Function”, IEEE International Test Conference, 2002.
- [107] J. Sun, M. Li, J. Wilstrup, “A Demonstration of Deterministic Jitter (DJ) Deconvolution”, IEEE Instrumentation and Measurement Technology Conference, May 2002.
- [108] R. Stephens, “Jitter analysis: The dual-Dirac model, RJ/DJ, and Q-scale”, Agilent Technologies Whitepaper, 2005. [Online]. Available: <http://cp.literature.agilent.com/litweb/pdf/5989-3206EN.pdf>
- [109] G. Foster, “Dual-Dirac, Scope Histograms and BERTScan Measurements - A Primer”, SyntheSys Research, September 2005. www.bertscope.com
- [110] Agilent Technologies, “Analyzing Jitter Using Agilent EZJIT Plus Software”, October 2005. [Online] Available: <http://cp.literature.agilent.com/litweb/pdf/5989-3776EN.pdf>
- [111] A. Kuo, T. Farahmand, N. Ou, S. Tabatabaei, A. Ivanov, “Jitter Models and Measurement Methods for High-Speed Serial Interconnects”, IEEE International Test Conference, 2004.
- [112] Maxim, “Clock (CLK) Jitter and Phase Noise Conversion - Application Note 3359”, Maxim, 2004 [Online]. Available: <http://pdfserv.maximic.com/en/an/AN3359.pdf>.
- [113] J. Wilstrup, “A method of serial data jitter analysis using one-shot time interval measurements”, IEEE International Test Conference Proceeding, 1998.
- [114] Xilinx DS132, “Using the Virtex Delay-Locked Loop”, [Online]. Available: http://www.xilinx.com/support/documentation/application_notes/xapp132.pdf.
- [115] D. Vandebout, “FPGAs!? Now What?”, XESS Corporation, 2014.
- [116] S. Sjöholm, L. Lindh, “VHDL for designer”, 1996.

-
- [117] Xilinx, “Virtex-5 Family Overview, DS100” [Online]. Available: http://www.xilinx.com/support/documentation/data_sheets/ds100.pdf
- [118] Xilinx, “Virtex-5 FPGA Data Sheet: DC and Switching Characteristics, DS202” [Online]. Available: www.xilinx.com/support/documentation/data_sheets/ds202.pdf.
- [119] Xilinx, “ML505/ML506/ML507 Evaluation Platform, User Guide, UG349” [Online]. Available: http://www.xilinx.com/support/documentation/boards_and_kits/ug347.pdf
- [120] J.M. Zogg, “GPS Basics”, ublox ag, 2002.
- [121] Vinchotech, “GPS Receiver A1080, User’s Manual”.
- [122] Vinchotech, “GPS Evaluation Kit A1080, User’s Manual”.
- [123] Klaus Betke, “The NMEA 0183 Protocol”, 2000.
- [124] Vinchotech, “GPS Firmware A1080 & A1035D, User’s Manual”.
- [125] SiRF Technology, “NMEA Reference Manual”, 2007.
- [126] Vinchotech, “1PPS Pulse Width, Application Note”, 2008.
- [127] K. Chapman, “UART Transmitter and Receiver Macros”, Xilinx, 2003.
- [128] European Cooperation for Space Standardization, “SpaceWire - Links, nodes, routers and networks”, European Space Agency, January 2003.
- [129] Agilent Technologies, “Agilent Technologies Infiniium 90000 Series Oscilloscopes, Data Sheet”, 2009.
- [130] Agilent Technologies, “EZJIT and EZJIT Plus Jitter Analysis Software for Infiniium Series Oscilloscopes”, April 2006.
- [131] Agilent Technologies, “EZJIT and EZJIT Plus Jitter Analysis Software for Infiniium Series Oscilloscopes, Data Sheet”, October 2010. [Online] Available: <http://cp.literature.agilent.com/litweb/pdf/5989-0109EN.pdf>
- [132] A. Aloisio, R. Giordano, V. Izzo, “Phase Noise Issues with FPGA-embedded DLLs and PLLs in HEP applications”, IEEE Transactions on Nuclear Science, Vol. 58, Issue 4, pp. 1664 - 1671, Aug 2011.
- [133] Agilent Technologies, “Agilent 81130A 400/660MHz Pulse/Data Generator, Quick Start Guide”, 1998.

-
- [134] Agilent Technologies, “Agilent 81130A 400/660MHz Pulse/Data Generator, Reference Guide”, 1998.
- [135] Xilinx, “ML505/ML506/ML507 Virtex-5 Evaluation Platform Schematics, Power Supplies” [Online]. Available: http://www.xilinx.com/support/documentation/boards_and_kits/ml505_20061205_bw.pdf
- [136] Texas Instruments, “PTH08T240W, PTH08T241W, Adjustable Power Module”, 2005.

